UNIVERSITY OF OKLAHOMA

GRADUATE COLLEGE

ANISOTROPIC POROCHEMOELECTROELASTIC SOLUTIONS FOR APPLICATIONS IN FIELD OPERATIONS AND LABORATORY CHARACTERIZATION OF SHALE

A DISSERTATION

SUBMITTED TO THE GRADUATE FACULTY

in partial fulfillment of the requirements for the

Degree of

DOCTOR OF PHILOSOPHY

By

MINH H. TRAN
Norman, Oklahoma
2013

Downloaded from SHAREOK. Persistent Handle URL: https://hdl.handle.net/11244/319253

ANISOTROPIC POROCHEMOELECTROELASTIC SOLUTIONS FOR APPLICATIONS IN FIELD OPERATIONS AND LABORATORY CHARACTERIZATION OF SHALE

A DISSERTATION APPROVED FOR THE
MEWBOURNE SCHOOL OF PETROLEUM AND GEOLOGICAL ENGINEERING

BY

_____
Dr. Younane Abousleiman, Chair

_____
Dr. Yucel Akkutlu

_____
Dr. Deepak Devegowda

_____
Dr. Maysam Pournik

_____
Dr. Roger Slatt

© Copyright by MINH H. TRAN 2013
All Rights Reserved.

This dissertation is dedicated to my family.

Acknowledgements

First and foremost, I would like to express my wholehearted appreciation to my advisor, Dr. Younane Abousleiman. I thank him for giving me the fruitful opportunity to work at the integrated PoroMechanics Institute (iPMI) and for his guidance throughout my graduate study. His enthusiasm and visionary approach to bridge fundamental research with engineering problems together with his constant demand for quality research have always motivated me to strive for the very best.

I extend my appreciation to the members of my dissertation committee, Dr. Deepak Devegowda, Dr. Maysam Pournik, Dr. Yucel Akkutlu, and Dr. Roger Slatt, for offering their valuable time to advise and share with me their professional experience in this work.

My appreciation also goes to my colleagues and friends, Dr. Son Hoang and Dr. Vinh Nguyen, for their stimulating discussions and constructive criticisms of my works. My special thanks must also go to Ms. Carla Cates for making every administrative matter go smoothly. I am also thankful to my colleagues at the integrated PoroMechanics Institute (iPMI) for their valuable support and discussions.

Last but not least, I am grateful to my parents, my wife, and daughter for their support and loving. They are the prime reason that I could be who I am.

Table of Contents

Acknowledgements iv

List of Tables vii

List of Figures viii

Abstract xi

Chapter 1: Introduction 1
1.1 Overview on Porochemoelectroelasticity 1
1.2 Review on Relevant Studies Leading to the Development of Porochemoelectroelasticity 2
1.3 Research Objectives and Approach 4

Chapter 2: Porochemoelectroelasticity 7
2.1 Introduction 7
2.2 Constitutive Relations 7
2.3 Transport Equations 11
2.4 Other Governing Equations 12
2.5 The Initial Ion Saturation in Shales 13
2.6 The Donnan Equilibrium Phenomena 15
2.6.1 The Electrochemical Equilibrium of Shale and External Fluids 15
2.6.2 Evidence of Donnan Equilibrium in Geological Systems 17
2.7 Summary 18

Chapter 3: The Mandel's Problem 20
3.1 Introduction 20
3.2 Problem Descriptions 22
3.2.1 The Porochemoelectroelastic Mandel's Problem 22
3.2.2 Boundary Conditions 23
3.3 Analytical Solutions 24
3.4 Solutions Validations with Special Cases 28
3.5 Examples of Applications 31
3.5.1 Laboratory Characterization for The Fluid Effects on Shale 31
3.5.2 Hydraulic Fracturing in Shale 38
3.5.3 Diagenesis of Clay-rich Sediment 42
3.6 Summary 45

Chapter 4: The Full Cylinder Problem 47
4.1 Introduction 47
4.2 Problem Descriptions 48
4.3 Analytical Solutions 51
4.3.1 Solutions for Unconfined Compression and Triaxial Test 51
4.3.2 Solutions for Confined Compression Test 55
4.4 Solutions Validations for Special Cases 58
4.5 Examples of Applications 60
4.5.1 Laboratory Testing for the Fluid Chemistry Effects 60

4.5.2 Determination of the Coupled Hydro-Electro-Chemical Flow Parameters Using the Pressure Transmission Test Data 64
4.6 Summary 67

Chapter 5: The Wellbore Problem 69
5.1 Introduction 69
5.2 The Inclined Wellbore Problem 70
5.2.1 Problem Descriptions 70
5.2.2 Boundary Conditions 72
5.3 Analytical Solutions 73
5.3.1 Solution for Poroelastic Plane Strain Problem 73
5.3.2 Solution for Uniaxial Stress Problem 79
5.3.3 Solution for Anti-plane Shear Problem 79
5.3.4 Complete Solution for Inclined Wellbore Problem 80
5.4 Solution Validations for Special Cases 81
5.5 Examples of Applications 85
5.5.1 Drilling in Shale 85
5.5.2 Leak-off Test 90
5.6 Summary 94

Chapter 6: Conclusions 96

References 99

Appendix A: Relationships between Elastic Stiffness Coefficients and Elastic Moduli for Anisotropic Medium 104
Transversely Isotropic Material 104
Orthotropic Material 105

Appendix B: Wellbore Plane Strain Solutions 107
Solution for Part 1: Axis-Symmetric Loading 107
Solution for Part 2: Deviatoric Loading 108

List of Tables

Table 2.1-Electrokinetic transport coefficients as in Nguyen & Abousleiman (2010) .. 12

Table 3.1-Summary of Trafalgar shale properties (Abousleiman et al., 1996) 29
Table 3.2-Summary of Woodford shale properties 32

Table 4. 1-Summary of shale sample properties use for simulation 65

List of Figures

Fig.2.1-The initial equilibrium condition of shale formation 14
Fig.2.2: The condition at wellbore drilling (or exposing to external fluid) 16

Fig.3.1-The original Mandel's problem (*Mandel*, 1953) 20
Fig.3.2-(a) Schematic of generalized boundary conditions for Mandel's problem, (b) Unjacketed compression test, (c) Hydraulic fracturing, (d) Consolidation of formation in a channel depositional environment 23
Fig.3.3-Comparison of pore pressure at the center from the current solutions when a_{sol} = a^o_f=1 and CEC=χ = 0 to the results in Abousleiman et al. (1996) 30
Fig.3.4-Comparison of lateral displacement (x = b) from the current solutions when a_{sol} = a^o_f=1 and CEC=χ = 0 to the results in Abousleiman et al. (1996) 30
Fig.3.5-Comparison of vertical displacement (z = a) from the current solutions when a_{sol} = a^o_f=1 and CEC=χ = 0 to the results in Abousleiman et al. (1996) 31
Fig.3.6-Distribution of pore pressure p^{total} along the sample width (a_{sol} = 0.87) 33
Fig.3.7-Evolution of pore pressure at the center of the sample (a_{sol} = 0.87) 34
Fig.3.8-Distribution of lateral displacement (u_x) along the sample width (a_{sol} = 0.87).. 34
Fig.3.9-Distribution of the effective σ'_{xx} along the sample width (a_{sol} = 0.87) 35
Fig.3.10-Distribution of the effective σ'_{zz} along the sample width (a_{sol} = 0.87) 35
Fig.3.11-Distribution of pore pressure p^{total} along the sample width (a_{sol} = 1) 36
Fig.3.12-Distribution of the effective σ'_{xx} along the sample width (a_{sol} = 1) 37
Fig.3.13-Distribution of p^{total} along the formation width 39
Fig.3.14-Distribution of horizontal displacement, u_x, along the formation width 39
Fig.3.15-Distribution of the effective σ'_{xx} along the formation width 40
Fig.3.16-Distribution of the effective σ'_{zz} along the formation width 41
Fig.3.17-Illustration of fracture closure due to proppant embedment on a chemically damaged and weakened formation 41
Fig.3.18-Schematic of simplified representation of diagenesis process 43
Fig.3.19-Pore pressure evolution at the bottom of the formation 44

Fig.4.1-Schematic of common laboratory testing conditions for cylindrical samples ... 49
Fig.4.2-Schematic of the pressure transmission test as taken from Ewy & Stankovic (2010) 50
Fig.4.3- Comparison of pore pressure at the center of the sample (r = 0) from the current solutions when CEC=χ = 0 to the results in Abousleiman & Cui (1998) 59
Fig.4.4- Comparison of tangential stress at the edge of the sample (r = R) from the current solutions when CEC=χ = 0 to the results in Abousleiman & Cui (1998) 59
Fig.4.5- Comparison of axial stress at the center of the sample (r = *0*) from the current solutions when CEC=χ = 0 to the results in Abousleiman & Cui (1998) 60
Fig.4.6-Distribution of pore pressure p^{total} along the radial direction (a_{sol} = 0.87) 61
Fig.4.7-Evolution of pore pressure at the center of the sample (a_{sol} = 0.87) 62

Fig.4.8-Distribution of the effective σ'_{rr} along the radial direction (a_{sol} = 0.87)..... 63
Fig.4.9-Distribution of the effective $\sigma'_{\theta\theta}$ along the radial direction (a_{sol} = 0.87)..... 63
Fig.4.10-Distribution of the effective σ'_{zz} along the radial direction (a_{sol} = 0.87)..... 64
Fig.4.11-Comparison between lab measured down stream pore pressure and simulated results using different values of k and χ..... 66
Fig.4.12- Comparison of lab measured down stream pore pressure, Chen et al. (2010) simulated results, and simulated results from this solution using different values of k = 0.3 nD and χ = 0.11 66
Fig.4.13- Comparison of lab measured down stream pore pressure, Chen et al. (2010) simulated results, and simulated results from this solution using different values for poroelastic properties (all with k = 0.3 nD and χ = 0.11)..... 67

Fig.5.1-Geological and wellbore coordinates..... 70
Fig.5.2-The far-field stress components expressed in wellbore coordinate 71
Fig.5.3-Effective tangential stress along $\theta = 90^o$, identical to the results in Abousleiman & Cui (1998)..... 81
Fig.5.4-Effective axial stress along $\theta = 90^o$, identical to the results in Abousleiman & Cui (1998)..... 82
Fig.5.5-Effective radial stress when using $D^a_{eff} = 9.6\times10^{-12}$ (m^2/s) and $D^c_{eff} = 1.47\times10^{-11}$ (m^2/s), the results does not reduce to that of Nguyen & Abousleiman (2010)..... 83
Fig.5.6-Effective tangential stress when using $D^a_{eff} = 9.6\times10^{-12}$ (m^2/s) and $D^c_{eff} = 1.47\times10^{-11}$ (m^2/s), the results does not reduce to that of Nguyen & Abousleiman (2010) 83
Fig.5.7-Effective radial stress, identical to the results in Nguyen & Abousleiman (2010) when using $D^a_{eff} = 2.53\times10^{-10}$ (m^2/s) and $D^c_{eff} = 3.86\times10^{-10}$ (m^2/s)..... 84
Fig.5.8-Effective tangential stress, identical to the results in Nguyen & Abousleiman (2010) when using $D^a_{eff} = 2.53\times10^{-10}$ (m^2/s) and $D^c_{eff} = 3.86\times10^{-10}$ (m^2/s) 84
Fig.5.9-Pore pressure along the direction of S_H at t = 15 minutes..... 86
Fig.5.10-Pore pressure along the direction of S_H at various times 86
Fig.5.11-Effective radial stress along the direction of S_H at t = 15 minutes..... 87
Fig.5.12-Effective tangential stress along the direction of S_H at t = 15 minutes..... 87
Fig.5.13-Effective radial stress along the direction of S_H at t = 15 minutes and CEC = 5, 10, 15 meq./100 grams 88
Fig.5.14-Effective radial stress along the direction of S_H at t = 15 minutes with ν_1 = 0.13, 0.2, 0.25 and ν_3 = 0.3..... 89
Fig.5.15-Effective radial stress along the direction of S_H at t = 15 minutes with E_1 = 7.4, 6.6, 5.8 (GPa) and E_3 = 4.2 (GPa) 89
Fig.5.16-Effective tangential stress along the direction of S_H at t = 15 minutes with ν_1 = 0.13, 0.2, 0.25 and ν_3 = 0.3..... 90
Fig.5. 17-Effective tangential stress along the direction of S_H at t = 15 minutes with E_1 = 7.4, 6.6, 5.8 (GPa) and E_3 = 4.2 (GPa) 90
Fig.5.18-Typical mud pressure and mud salinity history during drilling and leak-off test 91
Fig.5.19-Pore pressure distribution ($\theta = 0^o$) at various times..... 93

Fig.5.20-Effective radial stress distribution ($\theta = 0^o$) at various times..... 93
Fig.5.21-Effective tangential stress distribution ($\theta = 0^o$) at various time..... 94

Abstract

In this study, the porochemoelectroelastic formulation is explained in details and fully expanded to capture the well known anisotropic nature of shale. The formulation is then applied to derive the analytical solutions for rectangular strip sample, cylindrical sample, and inclined wellbore under various loading and in-situ conditions while being exposed to an external fluid. The newly-derived solutions can be considered as necessary extensions of some existing analytical solutions to capture the anisotropic and chemically active nature of shale formations. Numerical examples are also included to illustrate the applications of the derived solutions in shale formations. The results show that ignoring either the porochemoelectroelastic behavior or the anisotropic characteristic of the shale formation will mislead the predictions and assessment of potential problems in laboratory and field operations.

In particular, the presence of negative fixed charges on the surface of clay minerals creates an osmotic pressure at the interface of the sample and the external fluid with magnitude proportional to the CEC of the sample. This Donnan-induced pore pressure when coupled with the load-generated pore pressure and the activity-generated pore pressure can result in significant tensile effective stresses and tensile damages in the shale. The results, thus, explain why some shales disintegrate when brought into contact with certain aqueous solutions while others do not.

Practical implications for field operations have been drawn for both wellbore drilling and hydraulic fracturing. The analyses show clearly that the effective tangential stresses and, hence, the axial stresses around a wellbore are greatly affected by the formation

anisotropic mechanical parameters. In addition, during drilling, the chemically-induced tensile effective radial stress and tangential stress can lead to wellbore spalling which in extreme cases may result in stuck pipe. On the other hand, during hydraulic fracturing, these induced tensile damages can weaken the shale formation leading to a wider fracture width and a shorter fracture length during the fracturing process. In addition, the damaged and weakened formation can exacerbate the problem of proppant embedment resulting in larger fracture closure and reduction of fracture length and productivity. Thus, the results explain why higher clay content intervals are often reported to be more "ductile" compared to lower clay content intervals. Moreover, the use of drilling mud and fracturing fluid having activity similar to the shale formation native pore fluid can help to prevent wellbore spalling and work for the advantage of the fracturing process.

In the laboratory testing context, these complex pore pressure, stresses responses and distributions can complicate the interpretation of experimental results for the effects of fluid chemistry on the rock matrix. Practically, it is recommended to gradually adjust the testing fluid salt concentration or applied load to the desired value so that excessive induced stress and pore pressure buildup inside the tested sample become minimal.

Finally, analysis for shale electrokinetic effects on pore pressure buildup during diagenesis suggests that, in addition to the intrinsically low permeability of shale, the semi-permeable membrane behavior of the clay matrix can effectively hinder the overall pore fluid diffusion process. As a result, the pore pressure buildup inside a shale formation can be much higher than in a clean sand formation under the same

consolidation rate. Hence, taking into account shale electrokinetic effects in basin modeling may give better predictions of overpressure issues in shale.

Chapter 1: Introduction

1.1 Overview on Porochemoelectroelasticity

Porochemoelectroelasticity, simply put, is a necessary extension of the classical poroelastic formulation (*Biot*, 1941) to capture the electrokinetic phenomena observed in chemically active porous media such as shale, clay soil, and biological tissues. The poroelastic formulation concerns the coupled hydro-mechanical behavior of linear-elastic porous media subjected to external actions such as loading and hydraulic pressure changes. To date, poroelasticity has spanned its range of applications to various disciplines from geotechnical and civil engineering, to petroleum and geological engineering, and to biomechanics. A classical application of the theory for petroleum engineers, for example, is the study of subsidence due to petroleum extraction (*Geerstma*, 1973).

On the other hand, it is well known that shale, clay soil, and biological tissues exhibit swelling and shrinking when exposed to aqueous solution. These observed behaviors are the result of the osmotic phenomena, which is non-hydraulically driven fluid flow, due to the imbalance of electro-chemical potentials between the pore fluid and the external environment (*Katchalsky & Curran*, 1967). There is substantial evidence that the negative charges on the surfaces of clay particles in soil and shale or the proteoglycans in cartilage allow these porous media to restrict the flow of certain pore fluid ionic species and behave like semi-permeable membranes, thus, give rise to the aforementioned osmotic phenomenon (*Olsen*, 1969; *Neuzil*, 2000; *Lu et al.*, 2009). Macroscopic transport formulations for coupled and simultaneous flow of the pore

fluid, and ions transport under the applications of hydraulic pressure, electrical potential, and chemical potential gradients have been derived based on non-equilibrium thermodynamics for irreversible processes (*Katchalsky & Curran*, 1967; *Shackelford & Daniel*, 1991; *Yeung & Mitchell*, 1993; *Malusis & Shackelford*, 2002; *Rosanne et al.*, 2005).

The complex physico-electro-chemical interactions within these chemically active porous media require proper quantification of their effects on the mechanical responses of the system. Following this overview are literature surveys on past studies leading to the development of the porochemoelectroelastic formulations. Then, the objectives and approach for the development of this research are reviewed.

1.2 Review on Relevant Studies Leading to the Development of Porochemoelectroelasticity

Early studies analyzed the coupled chemical-mechanical interactions in chemically active porous media were presented by lumping the hydraulic pressure and the activity-generated osmotic pressure into a chemical potential term, ignoring not only the effects of solute transport but also the aforementioned electrokinetic phenomena observed in charged saturated porous media. This lumped chemical potential is then regarded as a modified pressure and used to evaluate the effective stresses. This approach has gained its popularity in the 1990's with studies addressing wellbore stability when drilling in shale formations (*Yew et al.*, 1990; *Sherwood & Bailey*, 1994; *Tan et al.*, 1996). In other simpler approaches, the fluid pressure and solute diffusion effects have been taken into

account; however, the important transient nature of the coupled deformation-diffusion processes (i.e. the time-dependent poroelastic effect) is ignored (*Van Oort*, 1994).

Extension of the Biot's poroelastic theory to account for the effects of solute transport has been the subject of extensive research. These researches have been referred to as porochemoelastic studies as the electrokinetic phenomena and the electrical coupling from ions transport are ignored. The anisotropic porochemoelastic formulations and analytical solution of an inclined wellbore drilled in transversely isotropic shale formation were first given by Ekbote (2002) and later generalized to account for the effects of temperature difference between the drilling mud and the shale formation (*Ekbote & Abousleiman*, 2005; *Ekbote & Abousleiman*, 2006). Applications of the theory to derive analytical and numerical solutions for laboratory characterization of intact cylindrical shale samples have been presented by Sarout (2003), Bunger (2010), and Sarout & Detournay (2011). Recently, the theory was extended to dual-porosity and dual-permeability medium to analyze the effects of mud chemistry on the responses of naturally fractured shale during wellbore drilling and laboratory characterization (*Nguyen & Abousleiman*, 2009; *Nguyen & Abousleiman*, 2010).

Generalizing the poroelastic theory to fully include the coupled chemical and electrokinetic effects has been introduced as early as 1987 using mixture theory and non-equilibrium thermodynamics (*Sachs & Grodzinsky*, 1987; *Corapcioglu*, 1991; *Sherwood*, 1993; *Huyghe & Janssen*, 1999). However, the complication of these approaches has restricted existing analytical solutions to 1-D problems which are limited for laboratory and field applications and fall short from serving as bench mark for validation of numerical schemes (*Gu et al.*, 1999; *Van Meerveld et al.*, 2003).

Recently, based on thermodynamic principles, Nguyen and Abousleiman (2010) have shown that the porochemoelectroelastic constitutive stress-strain relations share the same form with the original Biot's poroelastic formulations. The electrochemical effects only enter through the transient nature of the fluid flow and ion transport due to differences in the electrochemical potentials across the porous medium. Therefore, any existing poroelastic solutions can be generalized to account for the chemically active behavior of charged saturated porous media. Indeed, the approach has been successfully applied to derive solutions for the 2-D anisotropic porochemoelectroelastic Mandel's problem (*Tran & Abousleiman*, 2013) and the 3-D inclined wellbores drilling in shale (*Nguyen & Abousleiman*, 2010; *Tran & Abousleiman*, 2013).

1.3 Research Objectives and Approach

Of particular interest is the electrochemical effects on the stress and pore pressure distributions in shale formations or shale samples during drilling, hydraulic fracturing, or laboratory testing. During these activities, the shale pore pressure is redistributed due to the electrochemical interactions between the invading down-hole or testing fluid and the native pore fluid. Simultaneously, the effective stress and strain distributions in the shale are also modified which can affect the integrity of the shale sample or formation. Indeed, the detrimental effects from shrinking and swelling shales and clay soil have been a chronic and costly problem for the petroleum industry (*Chenevert*, 1998; *Nguyen et al.*, 2009; *Abousleiman et al.*, 2010; *Hemphil et al.*, 2010). Moreover, shales have often been observed to exhibit some degree of anisotropy due to the alternated layering of thin lithofacies, oriented clay particles and organic matter during diagenesis (*Thomsen*, 1986; *Jonhston & Christensen*, 1995). For example, the Woodford shale

Young's modulus measured in direction parallel to sample lamination has been reported to be higher than those measured in direction perpendicular to sample lamination by as much as 30% (*Abousleiman et al.*, 2007; *Sierra et al.*, 2010). In addition, it has been observed that gas/oil shale formations sometimes contain sets of parallel vertical fractures which make these shale formations behave as orthotropic medium when investigated at the reservoir scale. The anisotropic nature of shale has been found to have significant impacts on the responses of shale formations and shale samples during drilling and laboratory testing (*Abousleiman et al.*, 1996; *Abousleiman & Cui*, 1998; *Tran & Abousleiman*, 2013). Therefore, analytical anisotropic porochemoelectroelastic solutions of various geometries and loading conditions relevant to laboratory experiments and field problems would be useful not only for simulating and analyzing these scenarios, but also for validating numerical algorithm of many petroleum industry related geomechanics problems.

Pursuing the aforementioned objectives, the detailed theoretical formulations for anisotropic porochemoelectroelasticity is first presented in Chapter 2. Discussion on the electrokinetic equilibrium conditions in the shale prior to and after being exposed to an external fluid is also included. Then, the analytical solutions for rectangular strip sample, cylindrical sample, and inclined wellbore under various loading and in-situ conditions while being exposed to aqueous solutions are given in subsequent chapters. In each chapter, a brief literature review of existing analytical solutions relevant to the problem geometry is also given. The derived analytical solutions are presented in an order from the simplest to the most complex in terms of problem geometry and the rigorousness of mathematical formulations as follows:

In Chapter 3, the orthotropic porochemoelectroelastic solution for rectangular strip sample (i.e. the famous Mandel's problem) is presented. The Mandel's problem configuration not only mimics laboratory setup for characterizing anisotropic materials, but also resembles a portion of a formation formed by two hydraulic fractures and is away from the fractures tips. Discussions and examples to illustrate the applications of the derived solution to laboratory characterization, hydraulic fracturing analysis, and diagenesis of shale formation are also given.

Then, the porochemoelectroelastic solution for transversely isotropic cylinder is derived and presented in Chapter 4. The cylindrical geometry is the most encountered laboratory testing configuration ranging from the unconfined compression test (uniaxial test), to the confined compression test (triaxial test), the consolidation test (K_o test), and to the pressure transmission tests. The detailed descriptions of these tests, their respective analytical porochemoelectroelastic solutions, and numerical examples illustrating the applications of the analytical solution are also discussed in Chapter 4.

Finally, the analytical porochemoelectroelastic solution for the most mathematical complex problem, i.e. the inclined wellbore drilled in transversely isotropic shale formation, is given in Chapter 5. Application of the solution to analyze the combined effects of porochemoelectroelastic behavior and anisotropy on wellbore responses is also presented. Wellbore responses during a leak-off test conducted soon after drilling are then analyzed to demonstrate the versatility of the solution in simulating complex down-hole conditions.

Chapter 2: Porochemoelectroelasticity

2.1 Introduction

In this chapter, the porochemoelectroelastic governing equations are revisited. In particular, the constitutive relations for chemically active porous media as presented in Nguyen & Abousleiman (2010) are reviewed and extended to anisotropic medium. Then, detailed calculations for initial ion saturation in the shale prior to being exposed to an external fluid are summarized. Finally, the electrokinetic equilibrium between the shale and an external fluid, i.e. the Donnan equilibrium condition, and its observations in geological systems are given.

2.2 Constitutive Relations

Under isothermal conditions ($dT = 0$), the skeleton dissipation function of a porous media saturated with fluid containing N components and subjected to small deformations is (*Coussy*, 2004)

$$\Phi_s = \sigma_{ij} \frac{d\varepsilon_{ij}}{dt} + \sum_r \tilde{\mu}_r \frac{dm_r}{dt} - \frac{d\Psi}{dt} \tag{2.1}$$

where the subscripts "s" and "r" stand for the skeleton and the fluid component "r" respectively. σ_{ij} and ε_{ij} are the components of the second-order Cauchy stress tensor and linearized small strain tensor respectively. Ψ denotes the Helmholtz energy of the porous medium per unit reference volume, and m_r (r = 1, 2, …, N) is the mole of the "r" component in the solution per unit of reference volume. $\tilde{\mu}_r$ is the electrochemical potential and is expressed as (*Katchalsky & Curran*, 1963)

$$\tilde{\mu}_r = V_r p + RT \ln(a_r) + z_r F \psi \tag{2.2}$$

where V_r, a_r, and z_r denote the partial molar volume, the chemical activity, and the valence of the "r" component in the fluid mixture. R is the universal gas constant, T is the temperature, F is the Faraday constant, and ψ is the electrical potential. Due to the additive nature of energy, the Helmholtz energy of the porous medium can be expressed as a sum of the skeleton Helmholtz energy, Ψ_s, and the fluid Helmholtz energy, Ψ_f.

$$\Psi = \Psi_s + \Psi_f = G_f - \phi p = \sum_r m_r \tilde{\mu}_r - \phi p \tag{2.3}$$

where $G_f = \sum m_r \tilde{\mu}_r$ is the Gibbs free energy of the solution and ϕ is the porosity of the rock. Differentiating Eq.2.3 and combine the result with Eq.2.1 yields

$$\Phi_s = \sigma_{ij} \frac{d\varepsilon_{ij}}{dt} - \sum_r m_r \frac{d\tilde{\mu}_r}{dt} + \phi \frac{dp}{dt} + p \frac{d\phi}{dt} - \frac{d\Psi_s}{dt} \tag{2.4}$$

Applying the Gibbs-Duhem relation $-\phi dp + \sum_r m_r d\tilde{\mu}_r = 0$ to the above expression allows the elimination of terms containing the electrochemical potentials in the skeleton dissipation function

$$\Phi_s = \sigma_{ij} \frac{d\varepsilon_{ij}}{dt} + p \frac{d\phi}{dt} - \frac{d\Psi_s}{dt} \tag{2.5}$$

From relations between thermodynamic potentials, $\Psi_s = G_s + \phi p$, the skeleton dissipation function can be alternatively expressed in terms of the skeleton Gibbs free energy as

$$\Phi_s = \sigma_{ij} \frac{d\varepsilon_{ij}}{dt} - \phi \frac{dp}{dt} + \frac{dG_s}{dt} \tag{2.6}$$

If the skeleton is assumed to undergoing reversible process, that is no dissipation from the skeleton, Eq.2.6 reduces to

$$dG_s = \sigma_{ij} d\varepsilon_{ij} - \phi dp \tag{2.7}$$

It is obvious from the above expression that G_s admits ε_{ij} and p as state variables. In other words, $G_s = f(\varepsilon_{ij}, p)$ and

$$\sigma_{ij} = \frac{\partial G_s}{\partial \varepsilon_{ij}} \tag{2.8a}$$

$$\phi = -\frac{\partial G_s}{\partial p} \tag{2.8b}$$

Differentiating Eq.2.8 and taking into account the Maxwell's symmetry relations of thermodynamic potentials yields

$$d\sigma_{ij} = \frac{\partial}{\partial \varepsilon_{ij}}\left(\sigma_{kl} d\varepsilon_{kl} - \phi dp\right) = \frac{\partial \sigma_{kl}}{\partial \varepsilon_{ij}} d\varepsilon_{kl} - \frac{\partial \phi}{\partial \varepsilon_{ij}} dp = C_{ijkl} d\varepsilon_{kl} + \alpha_{ij} dp \tag{2.9a}$$

$$d\phi = -\frac{\partial}{\partial p}\left(\sigma_{ij} d\varepsilon_{ij} - \phi dp\right) = -\frac{\partial \sigma_{ij}}{\partial p} d\varepsilon_{ij} + \frac{\partial \phi}{\partial p} dp = -\alpha_{ij} d\varepsilon_{ij} + \frac{1}{K_\phi} dp \tag{2.9b}$$

In the above expression, C_{ijkl} are the components of the fourth-order elastic stiffness tensor, α_{ij} are the components of the second-order Biot's pore pressure tensor, and $1/K_\phi$ is the pore compressibility (*Wang*, 2000). The relationships between the components of the elastic stiffness tensor and the elastic moduli and poroelastic coefficients of transversely isotropic and orthotropic medium are given in Appendix A. Assuming that the porous medium is completely saturated with fluid and is in isothermal condition, the relation between total fluid content variation, $d\zeta$, and the variation of porosity, $d\phi$, is given as

$$d\zeta = \frac{dm_f}{\rho_f^o} = \frac{d(\phi \rho_f)}{\rho_f^o} = d\phi + \frac{\phi^o}{\rho_f^o} d\rho_f = d\phi + \frac{\phi^o}{K_f} dp \tag{2.10}$$

where m_f is the total fluid content in moles, ρ_f is the fluid mass density in mole/m^3, and $1/K_f$ is the isothermal compressibility of the fluid. The superscript "o" denotes the initial state of each variable. Combining Eq.2.10 with Eq.2.9b yields the familiar constitutive relation for the total fluid content variation

$$d\zeta = -\alpha_{ij} d\varepsilon_{ij} + \left(\frac{1}{K_\phi} + \frac{\phi_o}{K_f} \right) dp = -\alpha_{ij} d\varepsilon_{ij} + \frac{1}{M} dp \tag{2.11}$$

in which M is the Biot's modulus (*Wang*, 2000). The constitutive relation for the variation of individual fluid components can be obtained as follows (*Nguyen & Abousleiman*, 2010)

$$d\zeta_r = \frac{dm_r}{\rho_f^o} = \frac{d(n_r m_f)}{\rho_f^o} = n_r^o d\zeta + \phi^o dn_r = n_r^o \left(-\alpha_{ij} d\varepsilon_{ij} + \frac{1}{M} dp \right) + \phi^o dn_r \tag{2.12}$$

where $n_r = m_r / m_f$ is the mole fraction of the "*r*" component in the solution. Eqs.2.9-10 and Eq.2.12 complete the set of stress-strain constitutive relations for chemically active and charged saturated anisotropic porous medium.

The above constitutive relations shows that the pore pressure instead of the electrochemical potentials is important; and changing the fluid composition (chemical activity) of the pore fluid and/or electrical potential at constant pressure will not affect the stress, strain, and total fluid content in the medium. This is a direct consequence from the fact that G_s admits ε_{ij} and p as state variables instead of $\tilde{\mu}_r$. The electrochemical interactions between different ionic species in the formations, however, enters through the transient nature of the fluid and ion flows due to differences in the electrochemical potentials across the porous medium as will be shown in the next section.

2.3 Transport Equations

Under isothermal condition, the set of phenomenological equations relating the flows and the driving forces for an aqueous pore fluid containing one type of cation and anion are (*Yeung & Mitchell*, 1993)

$$q_i = L_{11}\frac{\partial(-P)}{\partial x_i} + L_{12}\frac{\partial(-\psi)}{\partial x_i} + L_{13}\frac{RT}{n_a^o}\frac{\partial(-n_a)}{\partial x_i} + L_{14}\frac{RT}{n_c^o}\frac{\partial(-n_c)}{\partial x_i} \tag{2.13}$$

$$I_i = L_{21}\frac{\partial(-P)}{\partial x_i} + L_{22}\frac{\partial(-\psi)}{\partial x_i} + L_{23}\frac{RT}{n_a^o}\frac{\partial(-n_a)}{\partial x_i} + L_{24}\frac{RT}{n_c^o}\frac{\partial(-n_c)}{\partial x_i} \tag{2.14}$$

$$J_i^{a,d} = L_{31}\frac{\partial(-P)}{\partial x_i} + L_{32}\frac{\partial(-\psi)}{\partial x_i} + L_{33}\frac{RT}{n_a^o}\frac{\partial(-n_a)}{\partial x_i} + L_{34}\frac{RT}{n_c^o}\frac{\partial(-n_c)}{\partial x_i} \tag{2.15}$$

$$J_i^{c,d} = L_{41}\frac{\partial(-P)}{\partial x_i} + L_{42}\frac{\partial(-\psi)}{\partial x_i} + L_{43}\frac{RT}{n_a^o}\frac{\partial(-n_a)}{\partial x_i} + L_{44}\frac{RT}{n_c^o}\frac{\partial(-n_c)}{\partial x_i} \tag{2.16}$$

with x_i denotes the spatial coordinates. I_i and q_i is the electrical current and the total fluid flux which includes the solvent and its dissolved ions. $J_i^{a,d} \cong J_i^a - n_a q_i / V_f^o$ and $J_i^{c,d} \cong J_i^c - n_c q_i / V_f^o$ are the diffusion mass fluxes (mol.m^{-2}.s^{-1}) of the ion species relative to that of the water solvent in which J_i^a and J_i^c are the absolute mass fluxes of the anion and cation relative to the solid frame work. L_{ij} are the phenomenological coefficients representing the various transport processes. For example, the coefficient L_{11} describes the hydraulic diffusivity (Darcy's law). Whereas, the coefficient L_{22} relates to electrical conductivity (Ohm's law) and the coefficients L_{33}, L_{44} relate to solute/ion diffusion (Fick's law). The symmetry of the phenomenological coefficients matrix is in accordance with Onsager's principle (*Onsager*, 1931). The L_{ij} coefficients as presented Yeung & Mitchell (1993) and Nguyen & Abousleiman (2010) are summarized in Table 2.1.

Table 2.1-Electrokinetic transport coefficients as in Nguyen & Abousleiman (2010)

Coefficients	Formulas	Transport Processes
L_{11}	$\kappa + \frac{\kappa_{eo}^2}{\kappa_e}$	Hydraulic conduction (Darcy's law); κ is the mobility
$L_{12} = L_{21}$	κ_{eo}	Electro osmosis/streaming potential; κ_{eo} is the electro-osmosis coefficient
$L_{13} = L_{31}$	$\left(-\chi\kappa + \frac{D_{eff}^a z_a F \kappa_{eo}}{RT\kappa_e} \right) \frac{n_a^o}{V_f^o}$	Chemical osmosis/streaming potential; χ is the membrane efficiency [0,1].
$L_{14} = L_{41}$	$\left(-\chi\kappa + \frac{D_{eff}^c z_c F \kappa_{eo}}{RT\kappa_e} \right) \frac{n_c^o}{V_f^o}$	
L_{22}	κ_e	Electrical conduction (Ohm's law); κ_e is the electrical conductivity
$L_{23} = L_{32}$	$\frac{D_{eff}^a z_a F}{RT} \frac{n_a^o}{V_f^o}$	Diffusion potential/electrophoresis
$L_{24} = L_{42}$	$\frac{D_{eff}^c z_c F}{RT} \frac{n_c^o}{V_f^o}$	
L_{33}	$\frac{D_{eff}^a}{RT} \frac{n_a^o}{V_f^o} + \left(\frac{D_{eff}^a z_a F}{RT} \frac{n_a^o}{V_f^o} \right)^2 \frac{1}{\kappa_e} + \left(\frac{\chi n_a^o}{V_f^o} \right)^2 \kappa$	Solute diffusion (Fick's first law); $D_{eff}^{a,c}$ is the effective anion/cation diffusion coefficients: $D_{eff}^{a,c} = (1-\chi)\phi^\tau D^{a,c}$ For perfect membrane ($\chi = 1$), there is no ionic flow.
L_{44}	$\frac{D_{eff}^a}{RT} \frac{n_c^o}{V_f^o} + \left(\frac{D_{eff}^c z_c F}{RT} \frac{n_c^o}{V_f^o} \right)^2 \frac{1}{\kappa_e} + \left(\frac{\chi n_c^o}{V_f^o} \right)^2 \kappa$	
$L_{34} = L_{43}$	$\left(\frac{F}{RTV_f^o} \right)^2 \frac{D_{eff}^a D_{eff}^c z_a z_c n_a^o n_c^o}{\kappa_e} + \left(\frac{\chi}{V_f^o} \right)^2 n_a^o n_c^o \kappa$	Coupled solute diffusion

2.4 Other Governing Equations

Other governing equations necessary for the solutions are the equilibrium equations,

$$\sigma_{ji,j} = 0 \tag{2.17}$$

the strain-displacement and rotation equations,

$$\varepsilon_{ij} = \frac{1}{2}\left(\frac{\partial u_i}{\partial x_j} + \frac{\partial u_j}{\partial x_i} \right) \tag{2.18}$$

and the mass and electrical charge balance equations for the whole fluid and its individual components

$$\partial\zeta / \partial t = -\vec{\nabla}.\vec{q} \tag{2.19}$$

$$\partial\zeta_a / \partial t = -V_o^f \vec{\nabla}.\vec{J}^a = -V_o^f \vec{\nabla}.(\vec{J}^{a,d} + n_a \vec{q} / V_o^f) \tag{2.20}$$

$$\partial\zeta_c / \partial t = -V_o^f \vec{\nabla}.\vec{J}^c = -V_o^f \vec{\nabla}.(\vec{J}^{c,d} + n_c \vec{q} / V_o^f) \tag{2.21}$$

$$\partial\rho_e / \partial t = -\vec{\nabla}.\vec{I} \tag{2.22}$$

in which $\vec{\nabla}$ is the gradient vector, and Einstein's convention for repeated indices is used.

2.5 The Initial Ion Saturation in Shales

It is well known that the constituent clays surfaces in the shale matrix contain excess negative charges, so called the negative fixed charge. Prior to drilling, the shale formation contains m_{fc}^o moles of negative fixed charge, and is saturated with pore fluid containing m_a^o mole of anion, m_c^o mole of cation at an initial pore pressure p_o. The electrical neutrality condition requires that the amount of cation in the pore fluid to be greater than the amount of anion as shown in Fig.2.1 and is expressed as

$$n_{fc} z_{fc} + n_a^o z_a + n_c^o z_c = 0 \tag{2.23}$$

where $n_{fc} = m_{fc} / m_{total}^o$, $n_a^o = m_a^o / m_{total}^o$, $n_c^o = m_c^o / m_{total}^o$ is the native mole fraction of the fixed charge, anion, cation in the shale formation respectively and m_{total}^o is the total mole of all charged species. z_{fc}, z_a, z_c is, respectively, the valence of the fixed charge, anion, and cation in the shale formation.

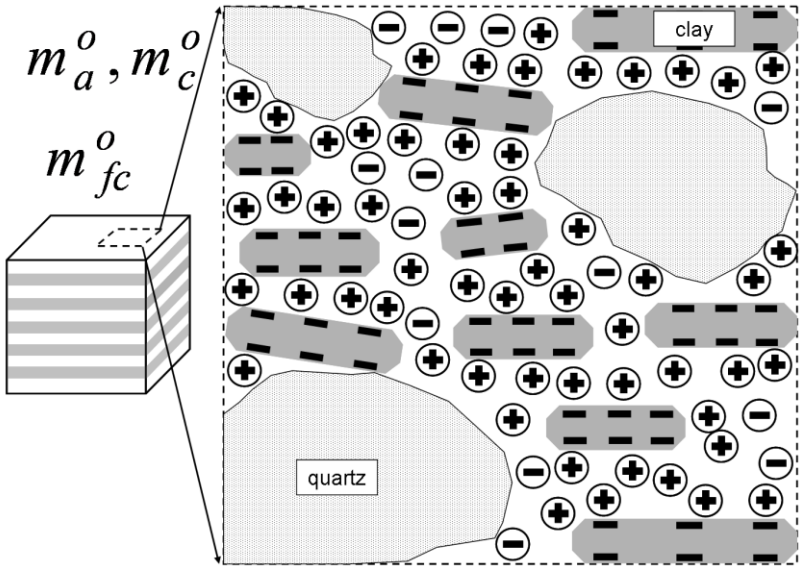


Fig.2.1-The initial equilibrium condition of shale formation

Imagine that a piece of the shale formation rock is submerged into a bath containing diluted solution of a C_xA_y salt with concentration expressed in term of mole fraction of the solutes, n_s^{eq}, that is in equilibrium with the pore fluid. The electrochemical equilibrium condition between the outer solution and the shale formation initial state requires that

$$\begin{cases} \tilde{\mu}_f^{eq} = \tilde{\mu}_f^o \\ \tilde{\mu}_a^{eq} = \tilde{\mu}_a^o \\ \tilde{\mu}_c^{eq} = \tilde{\mu}_c^o \end{cases} \tag{2.24}$$

Substitution of Eq.2.2 into Eq.2.24 and assuming diluted solution yields

$$\begin{cases} V_f^o p_{eq} + RT \ln\left[1-(x+y)n_s^{eq}\right] = V_f^o p_o + RT \ln\left[1-(n_a^o + n_c^o)\right] \\ V_f^o p_{eq} + RT \ln\left[x n_s^{eq}\right] + z_a F\psi_{eq} = V_f^o p_o + RT \ln\left[n_a^o\right] + z_a F\psi_o \\ V_f^o p_{eq} + RT \ln\left[y n_s^{eq}\right] + z_c F\psi_{eq} = V_f^o p_o + RT \ln\left[n_c^o\right] + z_c F\psi_o \end{cases} \tag{2.25}$$

For formations saturated with diluted solution of a 1:1 salt (e.g. NaCl, KCl), i.e. $x = y = 1$, applying the electro neutrality condition for the salt, i.e. $xz_c + yz_a = 0$, gives the

native mole fraction of each ion species in a shale formation as follows (*Nguyen & Abousleiman*, 2010)

$$n_a^o = \frac{1}{2z_a}\left[-z_{fc}n_{fc} - \sqrt{(z_{fc}n_{fc})^2 - 4z_a z_c (n_s^o)^2}\right] \tag{2.26}$$

$$n_c^o = \frac{1}{2z_c}\left[-z_{fc}n_{fc} + \sqrt{(z_{fc}n_{fc})^2 - 4z_a z_c (n_s^o)^2}\right] \tag{2.27}$$

with

$$n_{fc} = 10^{-2}\, CEC\, \frac{(1-\phi_o)\rho_{shale} V_f^o}{\phi_o} \tag{2.28}$$

$$n_s^o = \frac{1-a_f^o}{2} \tag{2.29}$$

in which CEC stands for Cation Exchange Capacity measured in milli-equivalent per 100 grams of dry clay (meq./100 grams) and ρ_{shale} is the average density of the shale constituencies measured in g/cc. n_s^o is the solute mole fraction in the formation fluid, and a_f^o is the water activity of the pore fluid which can be estimated from retrieved core samples using an osmometer. Derivation for n_a^o and n_c^o of salt solution of different *x*:*y* can be carried out analogously.

2.6 The Donnan Equilibrium Phenomena

2.6.1 The Electrochemical Equilibrium of Shale and External Fluids

During the laboratory testing, drilling, or hydraulic fracturing processes, the shale is often exposed to an external solution (so called mud) with solute concentration, n_s^{mud}, different from its native pore fluid as illustrated in Fig.2.2.

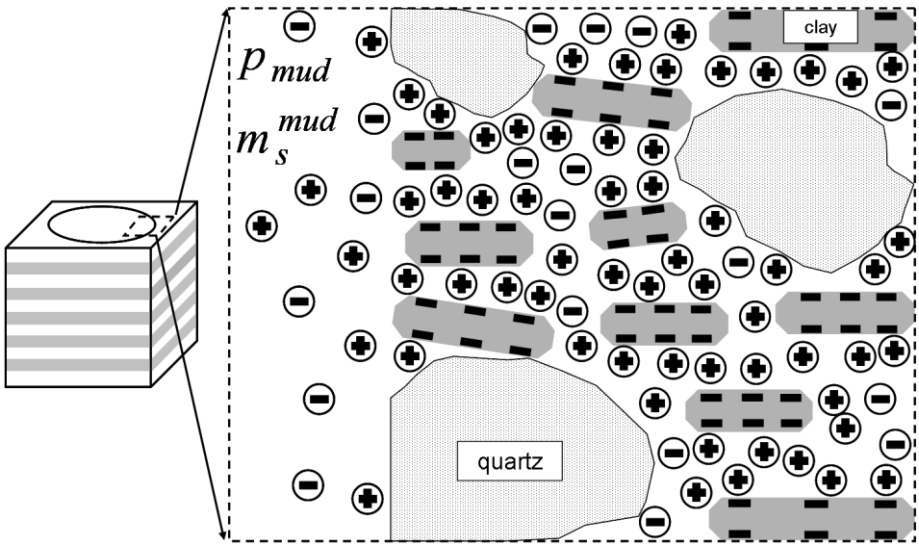


Fig.2.2: The condition at wellbore drilling (or exposing to external fluid)

Because of the difference in solute concentration between the mud and the native pore fluid, the following conditions are required to avoid infinite fluxes at the mud-shale interface

$$\begin{cases} \tilde{\mu}_f^{mud} = \tilde{\mu}_f^o \\ \tilde{\mu}_a^{mud} = \tilde{\mu}_a^o \\ \tilde{\mu}_c^{mud} = \tilde{\mu}_c^o \end{cases} \tag{2.30}$$

Assuming that the mud also contains 1:1 salt and that $z_c = 1 \text{and} z_a = z_{fc} = -1$, the formation ion concentrations at the mud-shale interface can be derived as

$$n_a^{shale}(t)\Big|_{\text{int}\,erface} = \frac{1}{2}\left[-n_{fc} + \sqrt{n_{fc}^2 + 4\left[n_s^{mud}(t)\right]^2}\right] \tag{2.31}$$

$$n_c^{shale}(t)\Big|_{\text{int}\,erface} = \frac{1}{2}\left[n_{fc} + \sqrt{n_{fc}^2 + 4\left[n_s^{mud}(t)\right]^2}\right] \tag{2.32}$$

with

$$n_s^{mud}(t) = \frac{1 - a_{mud}(t)}{2} \tag{2.33}$$

Eqs.2.31-2.32 show that the total ion mole fraction (i.e. the sum of anion and cation) in the shale formation at the mud-shale interface, $n_o^a\big|_{\text{int }erface} + n_o^c\big|_{\text{int }erface} = \sqrt{n_{fc}^2 + 4\left[n_s^{mud}(t)\right]^2}$, is larger than or equal to the mud total ion concentration of $2n_s^{mud}$. Consequently, there is an induced osmotic pressure at the mud-shale interface

$$\begin{aligned}\Delta p_{mud/shale}(t) = p_{shale}\big|_{\text{int }erface} - p_{mud}(t) &= \frac{RT}{V_f^o}\left[n_a^{shale}(t)\Big|_{r=Rw} + n_c^o(t)\Big|_{r=Rw} - 2n_s^{mud}(t)\right] \\ &= \frac{RT}{V_f^o}\left[\sqrt{n_{fc}^2 + 4\left[n_s^{mud}(t)\right]^2} - 2n_s^{mud}(t)\right]\end{aligned} \tag{2.34}$$

Eq.2.34 shows that for the same mud solute concentration, the higher the CEC of the formation, the larger the osmotic pressure differential developed at the mud-shale interface. When the formation is free of fixed charge (CEC = 0), the pressure and ion concentrations are indeed continuous at the mud-shale interface. The discontinuities of ion concentrations and pore pressure at the interface of a charged saturated porous media and an external fluid are known in chemistry as the Donnan equilibrium effect (*Overbeek*, 1956).

2.6.2 Evidence of Donnan Equilibrium in Geological Systems

Following the same procedure to obtain Eq.2.31, the anion concentration in a shale layer that is in equilibrium with an adjacent sand layer having solute concentration n_{solute}^{sand} is:

$$n_a^{shale} = \frac{1}{2}\left[-n_{fc} + \sqrt{n_{fc}^2 + 4\left(n_{solute}^{sand}\right)^2}\right] \tag{2.35}$$

Assuming that both the sand layer and the shale layer are saturated with a 1:1 salt, the anion concentration in the sand layer is $n_a^{sand} = n_{solute}^{sand}$. Comparing the expression for shale anion concentration and sand anion concentration, it can be easily shown that

$$n_a^{shale} = \frac{1}{2}\left[-n_{fc} + \sqrt{n_{fc}^2 + 4\left(n_{solute}^{sand}\right)^2}\right] \le n_a^{sand} \tag{2.36}$$

Therefore, in a sand-shale sequence, the anion concentration of a shale layer is likely smaller than that of the adjacent sands. Indeed, measurements of anion content in sand-shale sequences have revealed that the anion (Cl^-) concentration in the shale layer is significantly smaller than that of the adjacent sand layers that it is in equilibrium with (*Schmidt*, 1973; *Chiligarian*, 1983; *Jones et al.*, 1989).

2.7 Summary

In this chapter, the anisotropic porochemoelectroelastic formulations are presented. The derived constitutive relations show that the pore pressure instead of the electrochemical potentials is important; i.e. changing the fluid composition (i.e. the chemical activity) of the pore fluid and/or electrical potential at constant pressure will not affect the stress, strain, and total fluid content in the medium. The electro-chemical interactions between different ionic species in the formations, however, enter through the transient nature of the fluid flow and ions transport due to differences in the electrochemical potentials across the porous medium. In addition, the electrokinetic contribution of clays negative fixed charges manifests itself as an osmotic pressure and a discontinuity in ion concentration (i.e. the Donnan equilibrium condition) at the shale and external fluid interface. Proper modeling for the electrokinetic phenomenon requires not only the ion

diffusion coefficients, rock membrane efficiency, but also the amount of clay fixed charges which can be estimated from sample Cation Exchange Capacity (CEC).

Chapter 3: The Mandel's Problem[1]

3.1 Introduction

The Mandel's problem (*Mandel*, 1953) involves an infinitely long rectangular specimen sandwiched between two rigid and impermeable plates as shown in Fig.3.1. The lateral sides of the specimen are free of any applied stresses and hydraulic pressure. On the other hand, a force $2F$ is applied to the rigid plates at $t = 0^+$.

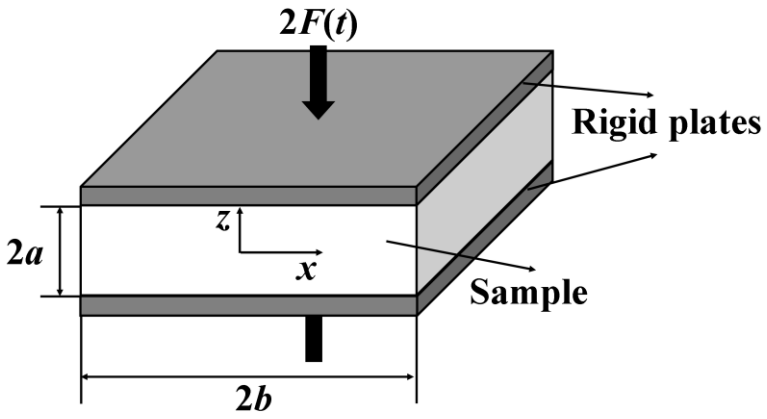


Fig.3.1-The original Mandel's problem (*Mandel*, 1953)

The first analytical solutions to this problem geometry were presented by Mandel (1953) for isotropic specimen. The solutions demonstrate a non-monotonic pore water pressure response (known as the Mandel-Cryer effect) resulting from the coupled pore pressure buildup and displacement. This is a distinctive feature of the Biot's poroelastic theory (1941) in contrast to the traditional uncoupled Terzaghi (1943). Abousleiman et al. (1996) have extended the original Mandel's problem to transversely isotropic media. Later, Hoang & Abousleiman (2009) provided the orthotropic poroviscoelastic solutions accounting for the viscous and orthotropic natures of the porous matrix. Recently, the

[1] Parts of this chapter have been published in Tran & Abousleiman, *Mech. Res. Comm.* (2013)

Mandel's problem solutions for a naturally fractured specimen have been derived by Nguyen & Abousleiman (2010) using dual-porosity and dual-permeability poroelasticity approach.

The Mandel's problem has recently been used by reservoir engineers as a benchmark for numerical algorithms to simulate the stresses and pore pressure responses in subsurface formation during water and steam flooding (*Yin et al*., 2006; *Fakcharoenphol et al*., 2012). This problem geometry also matches many testing configurations in biomechanics and geomechanics for anisotropic material (*Hoang & Abousleiman*, 2009).

In this chapter, the transversely isotropic poroelastic Mandel's problem solutions (*Abousleiman et al*., 1996) are generalized to orthotropic porochemoelectroelastic medium. The solution is then used to investigate the electrochemical effects on the stresses and pore pressure distribution in shale during laboratory testing, diagenesis, and hydraulic fracturing. During these activities, the shale pore pressure is redistributed due to the electrochemical interactions between the outer environment fluid and the native pore fluid which simultaneously alter the effective stresses and strains distribution. These phenomena are known to be attributable to overpressure and integrity problems of shale formations (*Neuzil*, 2000; *Abousleiman et al*., 2010). The presented solutions not only serve as benchmarks for geomechanics modelers to validate their numerical algorithms but also can be used for simulating experimental testing results and predicting shale formation responses during hydraulic fracturing and diagenesis processes as illustrated with the numerical examples.

3.2 Problem Descriptions

3.2.1 The Porochemoelectroelastic Mandel's Problem

In this work, the Mandel's problem boundary conditions are generalized as shown in Fig.3.2a so that the lateral sides of the specimen are subjected to hydraulic pressure, $P(t)$, and normal stress, $S(t)$, while being exposed to a fluid with solute molar concentration $n_s^{sol}(t)$. Such generalization is necessary to capture the possible laboratory testing conditions and in-situ conditions during hydraulic fracturing and diagenesis. For example, shown in Fig.3.2b is the schematic of an unjacketed triaxial test with the sample being tested for the fluid chemistry effects on its mechanical properties. The prescribed load, $2F(t)$, and strain, $2e(t)$, on the impermeable rigid plates simulate the load and stroke-control testing conditions respectively. The geometry and boundary conditions shown in Fig.3.2a can also be used to analyze the responses of a rectangular portion of a shale formation formed by two parallel fractures and is away from the fracture tips as depicted in Fig.3.2c. Finally, a 90^o rotation of either the left or the right half of Fig.3.2a can be utilized to simulate the sediments consolidation in a channel depositional environment as illustrated in Fig.3.2d.

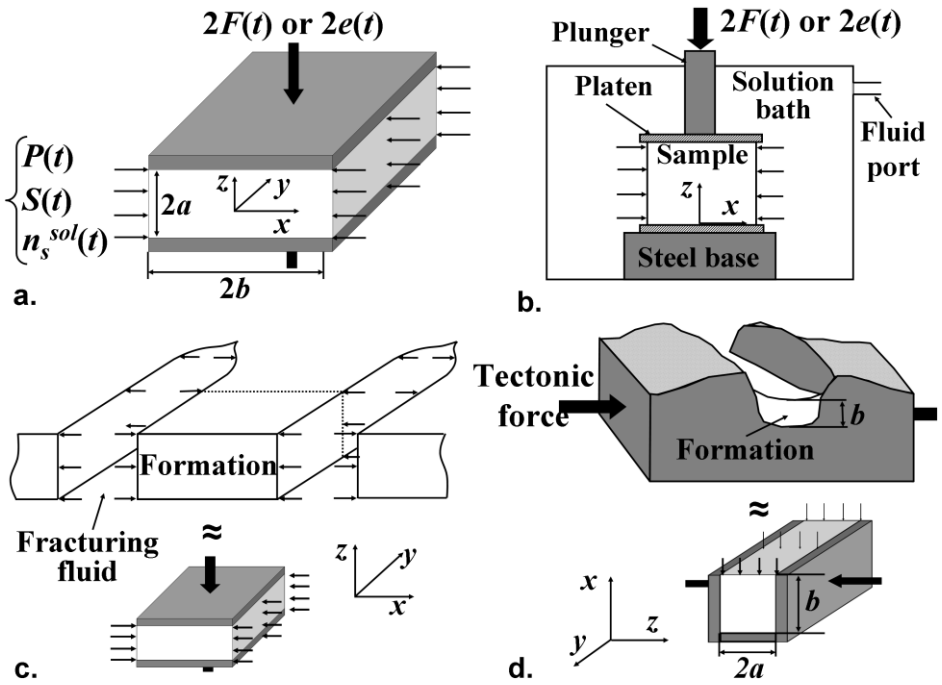


Fig.3.2-(a) Schematic of generalized boundary conditions for Mandel's problem, (b) Unjacketed compression test, (c) Hydraulic fracturing, (d) Consolidation of formation in a channel depositional environment

Because the specimen is long, the plane-strain condition, namely that the displacement and flux vanish in the *y*-direction, prevails. In addition, because of the two rigid plates all horizontal planes remain horizontal during the entire loading process (i.e. $\partial \varepsilon_{zz} / \partial x = 0$ and $\varepsilon_{xz} = 0$) and fluid flux is only in the *x*-direction. The material is so oriented that the *xy*, *xz*, and *yz* planes coincide with the planes of material symmetry. Throughout the disseration, the sign convention for stresses and strains is compression positive.

3.2.2 Boundary Conditions

Following the descriptions in Fig.3.2a, the perturbed state boundary conditions at $x = \pm b$ are as follows

$$\sigma_{xx} = S(t) - S_{xx} = \Delta S \tag{3.1a}$$

$$p = P(t) + \left[\sqrt{n_{fc}^2 + 4\left[n_s^{sol}(t)\right]^2} - 2n_s^{sol}(t) \right] \left(RT / V_f^o \right) - p_o = \Delta P(t) \tag{3.1b}$$

$$p_a = \left[n_s^{sol}(t) + \Delta n_a^{sol/shale}(t) - n_a^o\right]\left(RT / V_f^o\right) = \Delta P_a(t) \tag{3.1c}$$

$$p_c = \left[n_s^{sol}(t) + \Delta n_c^{sol/shale}(t) - n_c^o\right]\left(RT / V_f^o\right) = \Delta P_c(t) \tag{3.1d}$$

The boundary conditions at $z = \pm a$ are $\int_{-b}^{b} \sigma_{zz}\, dx = 2F(t)$ for load-control mode and $\varepsilon_{zz} = e(t)$ for stroke-control mode.

3.3 Analytical Solutions

In the Cartesian coordinate system, the porochemoelectroelastic stress-strain constitutive relations taking into account the plane-strain conditions are

$$\sigma_{xx} = C_{11}\varepsilon_{xx} + C_{13}\varepsilon_{zz} + \alpha_1 p \tag{3.2a}$$

$$\sigma_{yy} = C_{12}\varepsilon_{xx} + C_{23}\varepsilon_{zz} + \alpha_2 p \tag{3.2b}$$

$$\sigma_{zz} = C_{13}\varepsilon_{xx} + C_{33}\varepsilon_{zz} + \alpha_3 p \tag{3.2c}$$

$$\xi = -\alpha_1\varepsilon_{xx} - \alpha_3\varepsilon_{zz} + p / M \tag{3.2d}$$

$$\xi_a = n_a^o\left[-\alpha_1\varepsilon_{xx} - \alpha_3\varepsilon_{zz} + p / M\right] + \phi^o n_a \tag{3.2e}$$

$$\xi_c = n_c^o\left[-\alpha_1\varepsilon_{xx} - \alpha_3\varepsilon_{zz} + p / M\right] + \phi^o n_c \tag{3.2f}$$

where the subscripts "1", "2", and "3" denote properties in the *x*-, *y*-, and *z*-directions respectively. In this work, the problem shall be solved using Laplace transform technique. In the Laplace transform domain, substitution of the constitutive relations into the equilibrium equations while taking into account the condition $\partial\varepsilon_{zz} / \partial x = 0$ gives

$$C_{11}\left(d\tilde{\varepsilon}_{xx} / dx\right) + \alpha_1\left(d\tilde{p} / dx\right) = 0 \tag{3.3}$$

where the tilde sign denotes variables in the Laplace transform domain. Substituting the constitutive equations and the flow equations into the mass and electrical charge

balance equations while assuming electrostatic condition ($\partial\rho_e / \partial t = 0$), and ignoring the ion transport by advection terms gives (*Nguyen & Abousleiman*, 2010)

$$s\begin{bmatrix} -\alpha_1 & \frac{1}{M} & 0 & 0 \\ -n_a^o\alpha_1 & \frac{n_a^o}{M} & \frac{\phi^o V_f^o}{RT} & 0 \\ -n_c^o\alpha_1 & \frac{n_c^o}{M} & 0 & \frac{\phi^o V_f^o}{RT} \end{bmatrix}\begin{bmatrix} \widetilde{\varepsilon}_{xx} \\ \widetilde{p} \\ \widetilde{p}_a \\ \widetilde{p}_c \end{bmatrix} = [D]\frac{d^2}{dx}\begin{bmatrix} \widetilde{p} \\ \widetilde{p}_a \\ \widetilde{p}_c \end{bmatrix} + s\alpha_3\begin{bmatrix} 1 \\ n_a^o \\ n_c^o \end{bmatrix}\widetilde{\varepsilon}_{zz} \tag{3.4a}$$

with s is the Laplace variable and

$$[D] = \begin{bmatrix} \kappa & -\chi\kappa & -\chi\kappa \\ n_a^o(1-\chi)\kappa & \frac{D_{eff}^a V_f^o}{RT} - n_a^o(1-\chi)\chi\kappa & -n_a^o(1-\chi)\chi\kappa \\ n_c^o(1-\chi)\kappa & -n_c^o(1-\chi)\chi\kappa & \frac{D_{eff}^c V_f^o}{RT} - n_c^o(1-\chi)\chi\kappa \end{bmatrix} \tag{3.4b}$$

Substituting of the integration of Eq.3.3 into Eq.3.4a gives

$$\underbrace{s\begin{bmatrix} \left(\frac{\alpha_1^2}{C_{11}} + \frac{1}{M}\right) & 0 & 0 \\ n_a^o\left(\frac{\alpha_1^2}{C_{11}} + \frac{1}{M}\right) & \frac{\phi^o V_f^o}{RT} & 0 \\ n_c^o\left(\frac{\alpha_1^2}{C_{11}} + \frac{1}{M}\right) & 0 & \frac{\phi^o V_f^o}{RT} \end{bmatrix}}_{[Y]}\begin{bmatrix} \widetilde{p} \\ \widetilde{p}_a \\ \widetilde{p}_c \end{bmatrix} = [D]\frac{d^2}{dx^2}\begin{bmatrix} \widetilde{p} \\ \widetilde{p}_a \\ \widetilde{p}_c \end{bmatrix} + s\alpha_3\begin{bmatrix} 1 \\ n_a^o \\ n_c^o \end{bmatrix}\widetilde{\varepsilon}_{zz} + s\alpha_1\begin{bmatrix} 1 \\ n_a^o \\ n_c^o \end{bmatrix}C_o \tag{3.5}$$

where C_o is a constant of integration. Solving Eq.3.5 for $\widetilde{p}$, $\widetilde{p}_a$, $\widetilde{p}_c$ using matrix diagonalization technique gives

$$\widetilde{p} = f_1 C_o + g_1\widetilde{\varepsilon}_{zz} + \sum_{i=1}^{3} m_{1i} C_i \cosh(\xi_i x) \tag{3.6a}$$

$$\widetilde{p}_a = f_2 C_o + g_2\widetilde{\varepsilon}_{zz} + \sum_{i=1}^{3} m_{2i} C_i \cosh(\xi_i x) \tag{3.6b}$$

$$\tilde{p}_c = f_3 C_o + g_3 \tilde{\varepsilon}_{zz} + \sum_{i=1}^{3} m_{3i} C_i \cosh(\xi_i x) \tag{3.6c}$$

with $\xi_i = \sqrt{s/\lambda_i}$ in which λ_i are the eigenvalues of the matrix $[Z] = [Y]^{-1}[D]$ with $\{m_{1i}, m_{2i}, m_{3i}\}$ as its corresponding eigenvectors, $f_i = \alpha_1 [Y]^{-1} \{1 \quad n_a^o \quad n_c^o\}^T$, and $g_i = \alpha_3 [Y]^{-1} \{1 \quad n_a^o \quad n_c^o\}^T$. Once the pore pressure solutions are obtained, the solutions for stresses, strains, and displacements can be easily derived using the constitutive relations as follows

$$\tilde{\varepsilon}_{xx} = A_o C_o - \frac{\alpha_1}{C_{11}} g_1 \tilde{\varepsilon}_{zz} - \frac{\alpha_1}{C_{11}} \sum_{i=1}^{3} m_{1i} C_i \cosh(\xi_i x) \tag{3.7}$$

$$\tilde{\sigma}_{xx} = C_{11} C_o + C_{13} \tilde{\varepsilon}_{zz} \tag{3.8}$$

$$\tilde{\sigma}_{zz} = A_1 C_o + A_2 \tilde{\varepsilon}_{zz} + A_3 \sum_{i=1}^{3} m_{1i} C_i \cosh(\xi_i x) \tag{3.9}$$

$$\tilde{u}_x = A_o C_o x - \frac{\alpha_1}{C_{11}} g_1 \tilde{\varepsilon}_{zz} x - \frac{\alpha_1}{C_{11}} \sum_{i=1}^{3} m_{1i} C_i \frac{\sinh(\xi_i x)}{\xi_i} \tag{3.10}$$

with

$$A_o = 1 - f_1 \alpha_1 / C_{11} \tag{3.11a}$$

$$A_1 = C_{13} - \frac{\alpha_1 C_{13}}{C_{11}} f_1 + \alpha_3 f_1 \tag{3.11b}$$

$$A_2 = C_{33} - \frac{\alpha_1 C_{13}}{C_{11}} g_1 + \alpha_3 g_1 \tag{3.11c}$$

$$A_3 = \alpha_3 - \frac{\alpha_1 C_{13}}{C_{11}} \tag{3.11d}$$

The constants of integration C_o, C_1, C_2, C_3 are determined using the boundary conditions. For the load-control case, the constants of integration are

$$C_o = \frac{A_2 \Delta\widetilde{S}}{\eta} - \frac{C_{13}}{\eta}\left[\frac{F}{a} - \frac{A_3}{a}\sum_{i=1}^{3} m_{1i} C_i \frac{\sinh(\xi_i a)}{\xi_i}\right] \tag{3.12}$$

$$\begin{bmatrix} C_1 \\ C_2 \\ C_3 \end{bmatrix} = [G]^{-1}\eta \begin{bmatrix} \eta\Delta\widetilde{p} - \left(aA_2\Delta\widetilde{S} - C_{13}\widetilde{F}\right)f_1 - \left(h\widetilde{F}\eta - A_1\Delta\widetilde{S}\right)ag_1 \\ \eta\Delta\widetilde{p}_a - \left(aA_2\Delta\widetilde{S} - C_{13}\widetilde{F}\right)f_2 - \left(h\widetilde{F}\eta - A_1\Delta\widetilde{S}\right)ag_2 \\ \eta\Delta\widetilde{p}_c - \left(aA_2\Delta\widetilde{S} - C_{13}\widetilde{F}\right)f_3 - \left(h\widetilde{F}\eta - A_1\Delta\widetilde{S}\right)ag_3 \end{bmatrix} \tag{3.13}$$

with

$$\eta = C_{11}A_2 - C_{13}A_1 \tag{3.14a}$$

$$h = \frac{C_{13}A_1 + \eta}{aA_2\eta} \tag{3.14b}$$

$$G_{ij} = m_{ij}\cosh(\xi_j a) - \left(hA_3 g_i m_{1j} - \frac{C_{13}A_3}{\eta a} f_i m_{1j}\right)\frac{\sinh(\xi_j a)}{\xi_j} \tag{3.14c}$$

For the stroke-control case, the constants of integration are

$$C_o = \frac{\Delta\widetilde{S}}{C_{11}} - \frac{C_{13}}{C_{11}}\widetilde{e} \tag{3.15}$$

$$\begin{bmatrix} C_1 \\ C_2 \\ C_3 \end{bmatrix} = [G]^{-1}\frac{1}{C_{11}} \begin{bmatrix} C_{11}\left(\Delta\widetilde{p} - \widetilde{e}g_1\right) - \left(\Delta\widetilde{S} - C_{13}\widetilde{e}\right)f_1 \\ C_{11}\left(\Delta\widetilde{p}_a - \widetilde{e}g_2\right) - \left(\Delta\widetilde{S} - C_{13}\widetilde{e}\right)f_2 \\ C_{11}\left(\Delta\widetilde{p}_c - \widetilde{e}g_3\right) - \left(\Delta\widetilde{S} - C_{13}\widetilde{e}\right)f_3 \end{bmatrix} \tag{3.16}$$

with

$$G_{ij} = m_{ij}\cosh(\xi_j a) - \left(hA_3 g_i m_{1j} - \eta a C_{13}A_3 f_i m_{1j}\right)\left[\sinh(\xi_j a)/\xi_j\right] \tag{3.17}$$

For the load-control case, the expression for vertical strain is

$$\widetilde{\varepsilon}_{zz} = h\widetilde{F} - \frac{A_1}{\eta}\Delta\widetilde{S} - \frac{A_1 C_{13} + \eta}{aA_2\eta}A_3\sum_{i=1}^{3} m_{1i}C_i\frac{\sinh(\xi_i a)}{\xi_i} \tag{3.18}$$

while $\widetilde{\varepsilon}_{zz} = \widetilde{e}$ for the stroke-control case. The vertical displacement is obtained by integrating $\widetilde{\varepsilon}_{zz}$ with respect to z

$$\tilde{u}_z\big|_{z=l} = \int_0^l \tilde{\varepsilon}_{zz} dz \tag{3.19}$$

The perturbed solutions in time domain can be obtained using numerical inverse Laplace transform algorithms such as the Stehfest's algorithm (*Stehfest*, 1970). In this work, the inverse Laplace transform is done using Stehfest's algorithm with 8 terms. The total solutions for stresses and pore pressure are simply the sum of the initial states and the perturbed states as follows

$$p^{total} = p_o + p \tag{3.20a}$$

$$\sigma_{xx}^{total} = S_{xx} + \sigma_{xx} \tag{3.20b}$$

$$\sigma_{zz}^{total} = S_{zz} + \sigma_{zz} \tag{3.20c}$$

The superscript "total" in this work shall indicate the total solution and, when using for stresses, it also implies the total stresses (i.e. stresses including pore fluid pressure). The effective stress, i.e. total stress minus the pore pressure, shall be indicated with a superscript comma. For example, the effective stress in the *x*-direction will be

$$\sigma_{xx}^{'} = \sigma_{xx}^{total} - p^{total} \tag{3.21}$$

3.4 Solutions Validations with Special Cases

If the pore fluid and the testing fluid are both free of salt/solutes (i.e. $a_{sol} = a^o_f = 1$), the current solutions have to reduce to the case of a poroelastic Mandel's problem regardless of the sample membrane efficiency (χ). On the other hand, if the rock is free of clay (i.e. CEC = 0, $\chi = 0$), the current solutions should also recover the poroelastic Mandel's solutions despite any difference in activities between the outer fluid and the native pore fluid. This is because, in the latter case, the ions are free to transport

between the outer environment and pore fluid in the absence of the membrane. Consequently, the water (solvent) does not need to move from one place to another in order to balance the difference in ion concentration and, thus, no additional pore pressure is created.

In this section, the solutions are validated against these special cases by comparing the generated pore pressure and displacements with those reported in Abousleiman et al. (1996). Table 3.1 summarizes the anisotropic elastic and poroelastic parameters of Trafalgar shale used by Aboulseiman et al. (1996). The specimen is assumed to have cross-section of 10 cm × 10 cm. The applied forces on the specimen top is assumed to be $F = 10^6$ N per m of specimen width. The sample is assumed to be oriented so that the applied load is perpendicular to the specimen isotropic plane.

Table 3.1-Summary of Trafalgar shale properties (Abousleiman et al., 1996)

Parameters	Values
Young's modulus in isotropic plane (GPa)	20.6
Young's modulus in transverse direction (GPa)	17.3
Poisson's ratio in isotropic plane	0.189
Poisson's ratio in transverse direction	0.246
Biot's coefficient in isotropic plane	0.733
Biot's coefficient in transverse direction	0.749
Biot's modulus (GPa)	15.8
Permeability (D)	1×10^{-7}

Shown in Fig.3.3-Fig.3.5 are, respectively, the comparisons for the pore pressure evolution at the center of the sample, the lateral displacement at the sample edge ($x = b$), and the vertical displacement at the sample top ($z = a$). The agreement between the results from this solution and those of Abousleiman et al. (1996) confirms the behavior and correctness of the current solutions in these special cases.

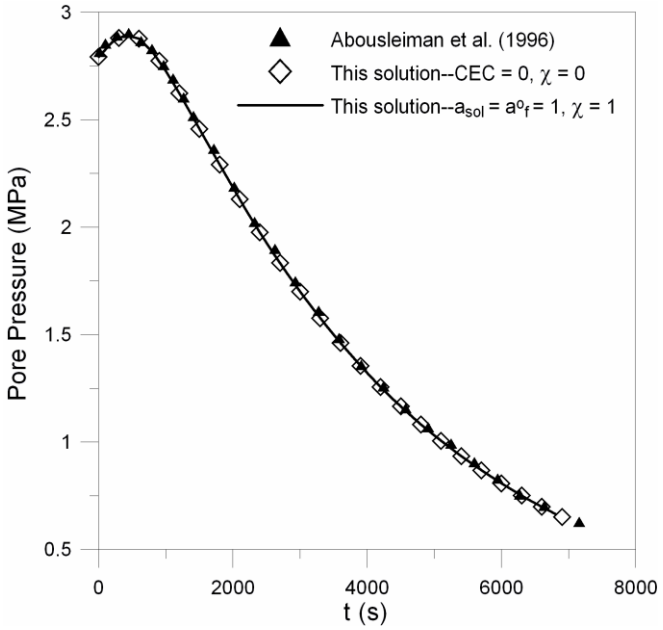


Fig.3.3-Comparison of pore pressure at the center from the current solutions when $a_{sol} = a^o_f = 1$ and CEC=$\chi = 0$ to the results in Abousleiman et al. (1996)

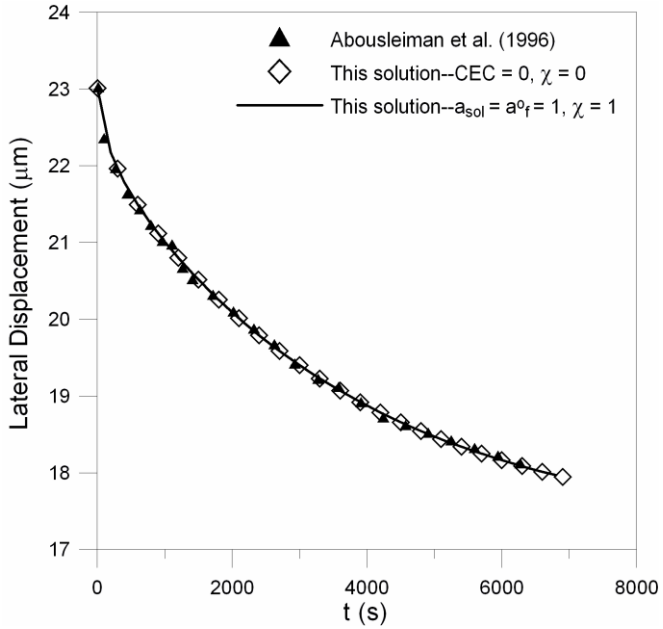


Fig.3.4-Comparison of lateral displacement ($x = b$) from the current solutions when $a_{sol} = a^o_f = 1$ and CEC=$\chi = 0$ to the results in Abousleiman et al. (1996)

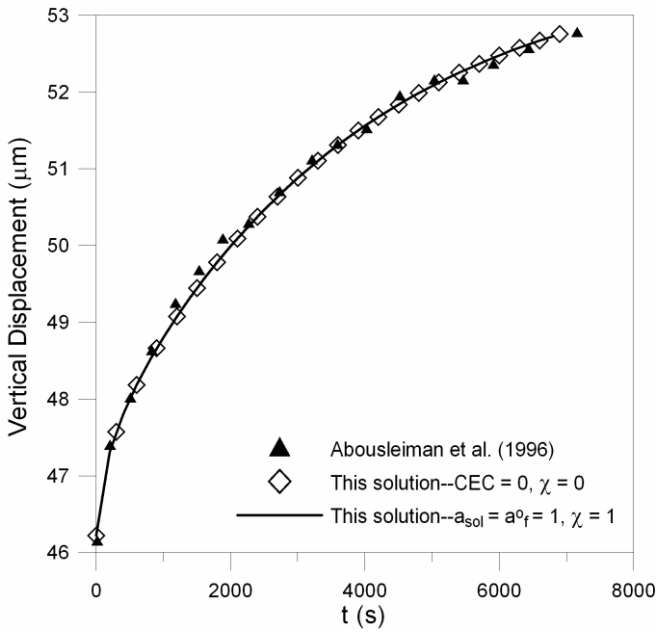


Fig.3.5-Comparison of vertical displacement ($z = a$) from the current solutions when $a_{sol} = a^o_f = 1$ and CEC=$\chi = 0$ to the results in Abousleiman et al. (1996)

3.5 Examples of Applications

3.5.1 Laboratory Characterization for The Fluid Effects on Shale

Consider a Woodford shale specimen with width of 2 cm (i.e. $2b$ = 2 cm), thickness of 2 cm (i.e. $2a$ = 2 cm), porosity of 15%, permeability of 200 nD, and CEC of 10 meq./100 gr. The sample is initially free of any stresses, pore pressure, and is saturated with pore fluid having activity a_o^f = 0.89. The sample membrane efficiency is assumed to be χ = 0.2. The specimen is then submerged into a chamber containing a testing fluid having higher salinity than the pore fluid with a_{sol} = 0.87 and is at zero hydraulic pressure (i.e. P(t) = $S(t)$ = 0 MPa). Simultaneously, an axial load $2F$ = 20 kN/m is applied to the rigid plates by the plunger. This setup mimics the laboratory characterization for shale properties variations under fluid exposure. The applied axial load is to assure a good contact between the plunger, the rigid plates and the sample so that acoustic monitoring for the effects of fluid chemistry on sample acoustic properties (or poroelastic

properties) can be achieved. The anisotropic poroelastic properties of the Woodford shale as reported in Abousleiman et al. (2007) are summarized in Table 3.2. The sample is oriented so that the material isotropic plane coincides with the *x*-*y* plane. The relationships between the elastic stiffness, C_{ij}, and the elastic moduli and poroelastic coefficients of transversely isotropic and orthotropic medium are given in Appendix A.

Table 3.2-Summary of Woodford shale properties

Parameters	Values	Notes
Young's modulus in isotropic plane (GPa)	7.4	Calculated with $E_1/E_3 = 1.75$ as from dynamic measurements
Young's modulus in transverse direction (GPa)	4.2	From quasi-static measurements
Poisson's ratio in isotropic plane	0.13	Calculated with $\nu_1/\nu_3 = 0.42$
Poisson's ratio in transverse direction	0.30	From quasi-static measurements
Biot's coefficient in isotropic plane	0.85	Assume $K_s = 40$ GPa
Biot's coefficient in transverse direction	0.88	Assume $K_s = 40$ GPa
Biot's modulus (GPa)	12.0	Assume $K_s = 40$ GPa, $K_f = 2.3$ GPa
Effective diffusion coefficient of Na^+ (m^2/s)	1.60×10^{-10}	$D^{Na+} = 1.33\times10^{-9}$, $\tau=1$
Effective diffusion coefficient of Cl^- (m^2/s)	2.44×10^{-10}	$D^{Cl-} = 2.03\times10^{-9}$, $\tau=1$
Porosity	0.15	From Hg-injection
Permeability (nD)	200	From pulse decay
Membrane efficiency	0.2	Assume
CEC (meq./100 gr of dry clay)	10	Measured; Woodford CEC = 5-15
Native activity	0.89	Measured; Woodford $a_o^f = 0.87$-0.89
Matrix density (g/cc)	2.3	From XRD mineralogy and porosity

Shown in Fig.3.6 is the pore pressure, p^{total}, distribution along the *x*-axis at different times with the normalized distance from sample center defined as $\bar{x} = x/b$. The pore pressure jump with magnitude of 0.29 MPa at the sample edge ($\bar{x} = 1$) corresponds to the osmotic pressure created by the Donnan equilibrium effect as previously discussed. Due to the application of the axial stress, an initial pore pressure surge with magnitude of 0.51 MPa is observed inside the sample. The Mandel-Cryer effect can be clearly observed at t = 5 s when pore pressure at the center of the sample reaches a higher value than the original pore pressure jump. The pore pressure drop near the sample edge at t = 5 s is a result of pore water drawing out of the sample due to the higher salt concentration in the testing fluid compared to the pore fluid. As time elapses, more

water is drawn out of the sample and the pressure drop front propagates toward the center. It is noteworthy that the pressure drop near the sample edge only appears when the rock matrix has the ability to partially restrain the ion transport ($\chi \neq 0$) as previously discussed. Finally, after approximately 48 hrs, the pore pressure inside the sample approaches an equilibrium value equal to the Donnan equilibrium pressure. The evolution of the pore pressure at the center of the sample is summarized in Fig.3.7. The lateral displacements distributions along the sample width are shown in Fig.3.8. Because of the initial pore pressure jump as previously explained, the lateral displacement of the sample edge for t = 0.005 s is larger than those in the period t = 5 s - 10000 s when water is drawn out of the sample from hydraulic and ion diffusion.

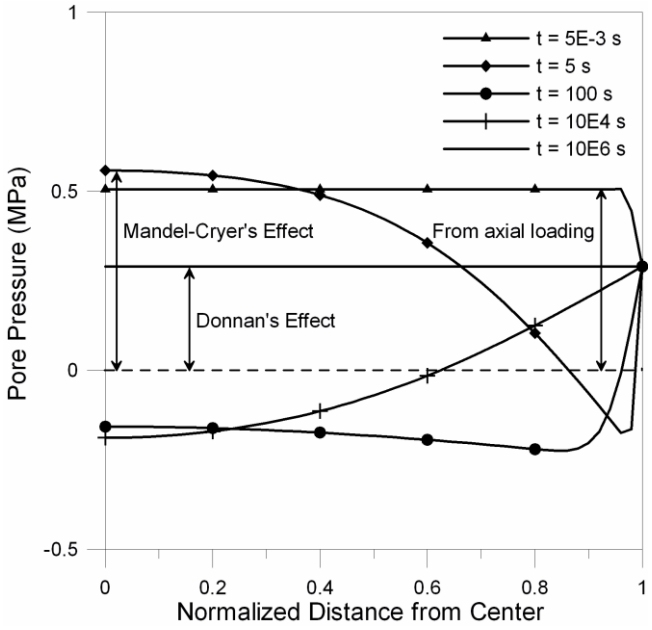


Fig.3.6-Distribution of pore pressure p^{total} along the sample width (a_{sol} = 0.87)

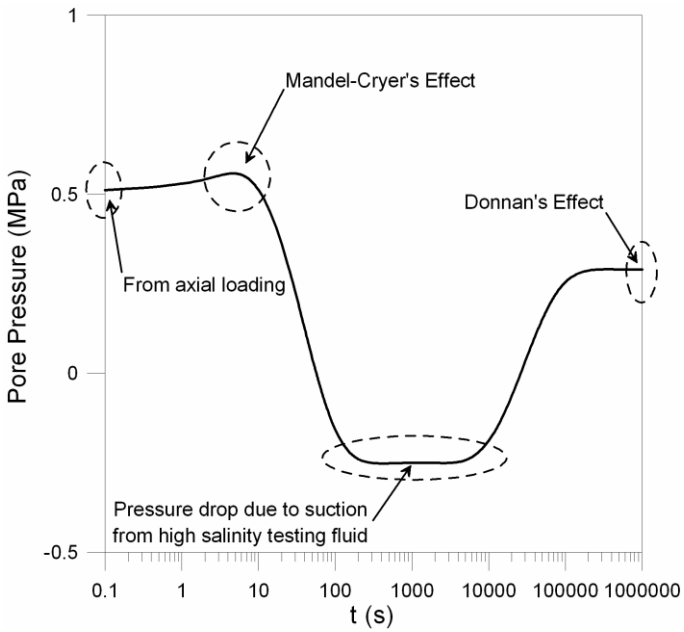


Fig.3.7-Evolution of pore pressure at the center of the sample (a_{sol} = 0.87)

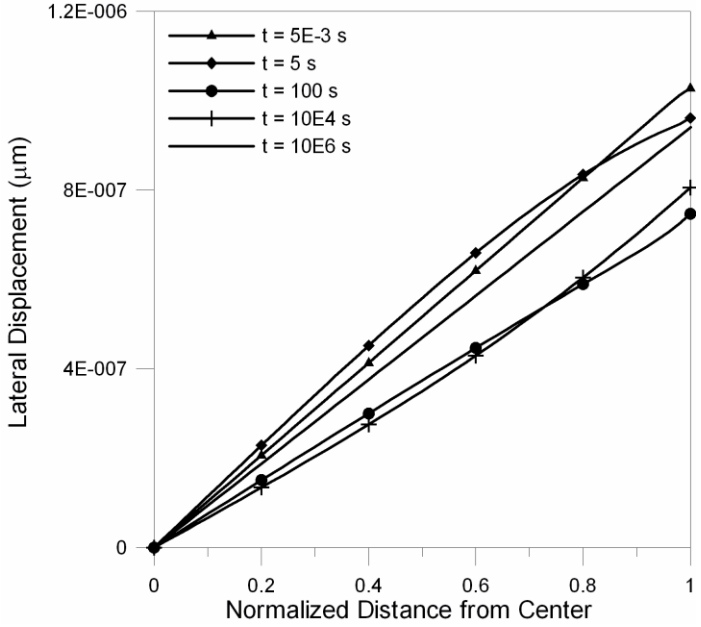


Fig.3.8-Distribution of lateral displacement (u_x) along the sample width (a_{sol} = 0.87)

The distributions of the effective horizontal stress, σ'_{xx}, and the effective vertical stress, σ'_{zz}, are shown in Fig.3.9 and Fig.3.10 respectively. Since confining pressure is absence in this example, the total stress σ_{xx}^{total} is trivial and the effective stress σ'_{xx} simply becomes $\sigma'_{xx} = 0 - p^{total}$. The results show that tensile stresses (negative values) can

develop inside the sample due to the induced pore pressure from the Donnan equilibrium effect, applied load, and Mandel-Cryer effect.

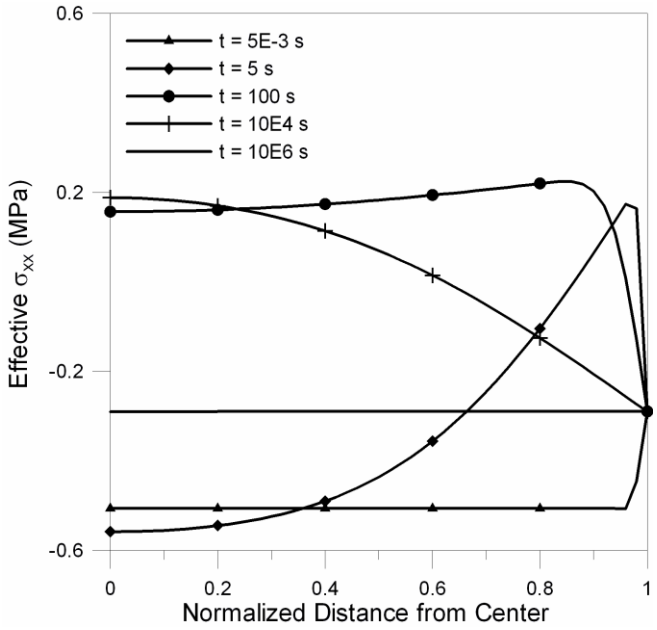


Fig.3.9-Distribution of the effective σ'_{xx} along the sample width (a_{sol} = 0.87)

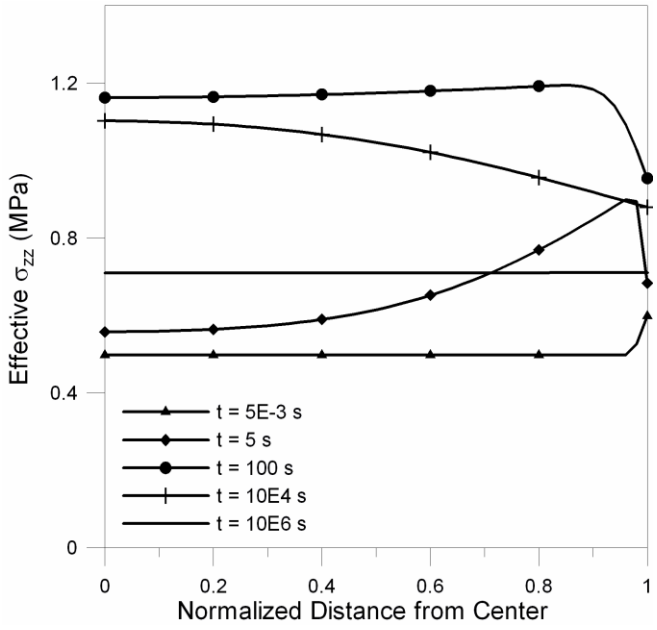


Fig.3.10-Distribution of the effective σ'_{zz} along the sample width (a_{sol} = 0.87)

Given that the Woodford shale tensile strength is 4-12 MPa (*Abousleiman et al.*, 2007; *Sierra et al.*, 2010), these induced tensile stress will not result in tensile damages for the Woodford sample under testing conditions used in this example. It can be observed

from Fig.3.10 that the suction of pore pressure out of the sample due to the higher salinity testing fluid helps to reduce induced tensile stress (see curves at t = 100 s, 10^4 s). Therefore, if a testing fluid with lower activity than the pore fluid is used, the induced osmotic pressure due to influx of water (solvent) to the sample from the testing fluid will increase the magnitude of tensile σ'_{xx} which may lead to tensile damage of the sample. For example, shown in Figs.3.11-3.12 is the distribution of pore pressure and effective σ'_{xx} of the Woodford shale sample when exposed to testing fluid with activity a_{sol} = 1 (deionized water). In this case, the induced tensile σ'_{xx} is as high as 5.5 MPa which can possibly cause some tensile damages to the sample.

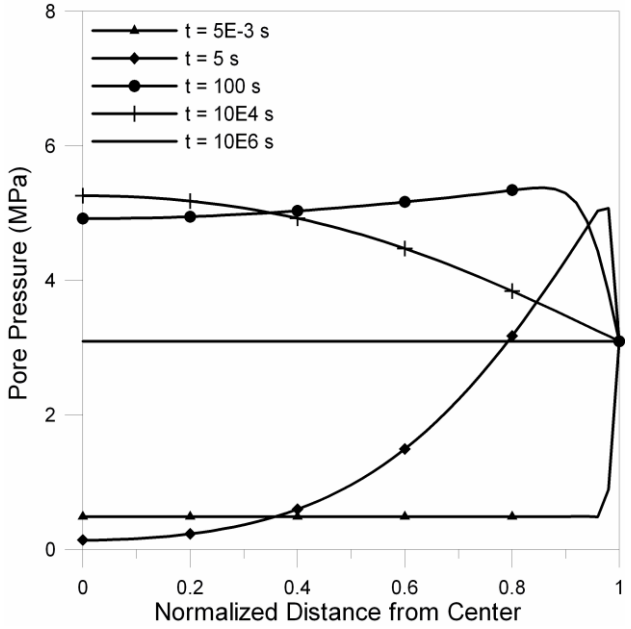


Fig.3.11-Distribution of pore pressure p^{total} along the sample width (a_{sol} = 1)

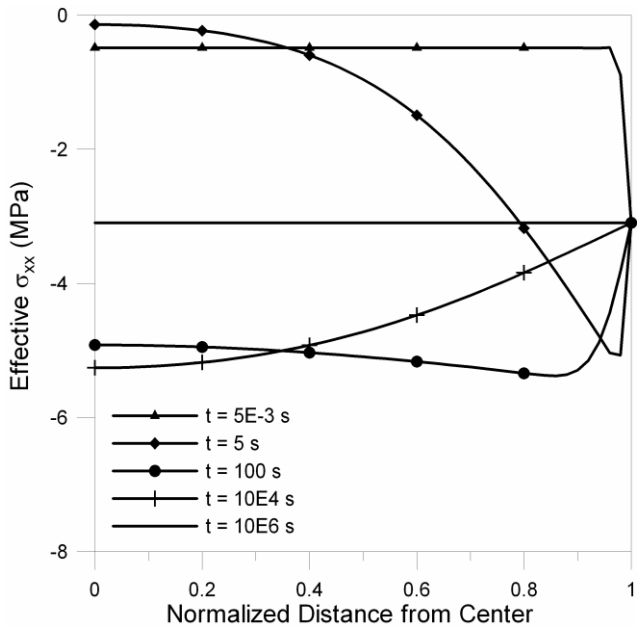


Fig.3.12-Distribution of the effective σ'_{xx} along the sample width (a_{sol} = 1)

The results from these analyses explain why while some shale can disintegrate when brought in contact with aqueous solution, others remain intact. In addition, shale samples with the same total clay content may not behave similarly when exposed to testing fluid. Indeed, whether or not a shale sample becomes damaged when exposed to aqueous solution depends on the amount of reactive clay minerals (i.e. how high the sample CEC is), and the difference in activity between the native pore fluid and the testing fluid. The results also show that the magnitude of the Donnan-induced pore pressure is rather small when compare to the load-generated pore pressure or activity-generate pore pressure. However, application of load to the sample while exposing it to aqueous solution can exacerbate the problem and lead to tensile damages in the sample. The tensile damages when occur can complicate the interpretation for the effects of fluid chemistry on the rock matrix. Practically, these damages can be avoided by gradually adjust the salt concentration of the testing fluid and the applied load to the desired value so that excessive stress and pore pressure buildup can be minimized.

3.5.2 Hydraulic Fracturing in Shale

Consider a horizontal well drilled in the Woodford formation and intersects with existing vertical natural fractures which have been observed to have spacing of approximately 1.2 m. Hydraulic fracturing is then conducted using fracturing fluid with activity of 0.95 which corresponds to a 2.5% in molar concentration of KCl commonly added to the water-based fluid for clay stabilizers (*Black & Hower*, 1965). During this process, the existing natural vertical fractures reopens and, thus, mimics the geometry shown in Fig.3.2c with $2b$ = 1.2 m. In this example, the fractures are contained vertically in an interval with thickness of 10 m (i.e. $2a$ = 10 m). The formation is assumed to be at depth 1829 m and is subjected to the following in-situ conditions S_{zz} = 41 MPa, $S_{xx} = S_{yy}$ = 25 MPa, p_o = 18 MPa, T = 100 ^{o}C. The fracturing process is conducted at a constant hydraulic pressure of 35 MPa so that $P(t) = S(t)$ = 35 MPa. In addition, it is assumed that the formation vertical expansion is restricted by the massive overlying layers ($e(t)$ = 0). The formation properties used for simulation are assumed similar to the previous example.

Fig.3.13 shows the distributions of pore pressure, p^{total} , along the width of the formation at 10, 20, and 30 minutes into the fracturing process. It can be seen that due to the compression of the hydraulic pressure on the formation, a pore pressure jump above the virgin pore pressure is observed inside the formation. Similar to the previous example, the Donnan equilibrium condition creates an osmotic pressure surge at the mud/shale interface ($\bar{x} = 1$). In addition, the lower salt concentration fracturing fluid has induced a pressure peak inside the formation near the fracture face due to influx of the water from the fracturing fluid into the formation. The distribution of lateral displacement along the

formation width is shown in Fig.3.14. The negative values denote displacement of the formation right half to the left due to hydraulic pressure. Due to the long diffusion time of the pore fluid pressure, the displacement during the entire fracturing process is mostly the elastic response under the action of the fracturing fluid pressure.

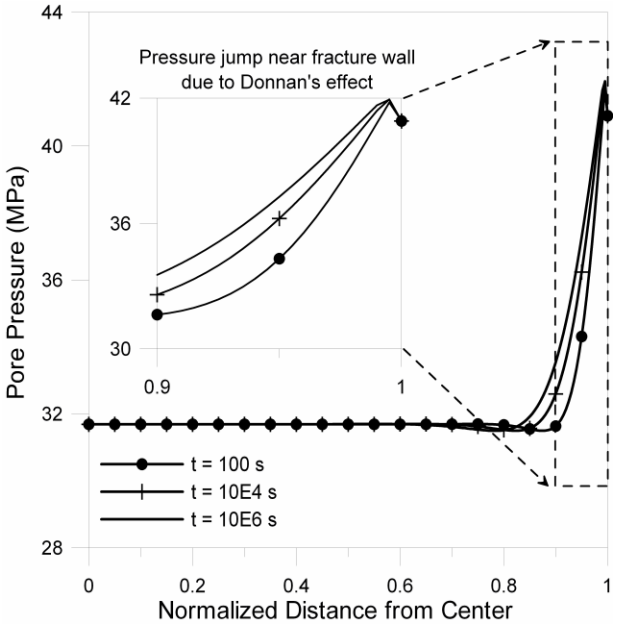


Fig.3.13-Distribution of p^{total} along the formation width

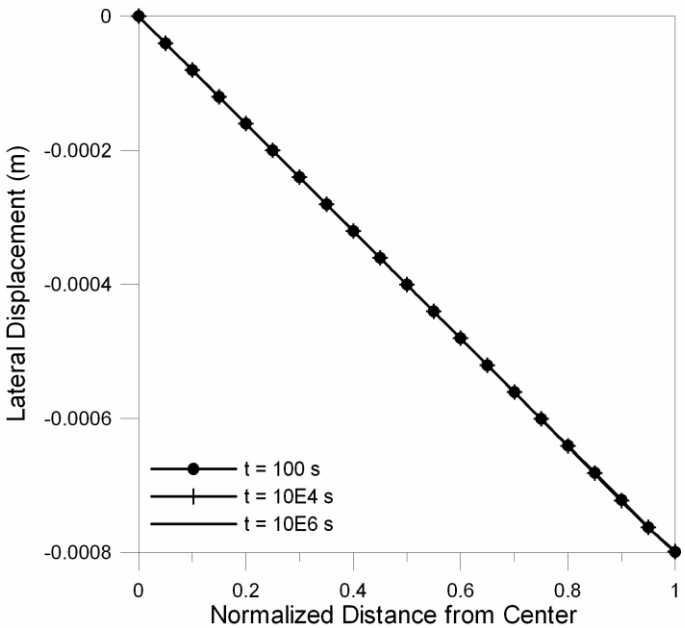


Fig.3.14-Distribution of horizontal displacement, u_x, along the formation width

Displayed in Fig.3.15 and Fig.3.16 are the distributions of the effective σ'_{xx} and σ'_{zz} along the formation width at various times during the hydraulic fracturing process. Similar to earlier discussion, the load-generated pore pressure and the osmotic-generated pressure have created a tensile zone near the fracture face which can lead to tensile damages and reduce the stiffness of the shale formation. Consequently, for the same fracturing condition, the fracture aperture can become wider leading to a shorter fracture length. In addition, the damaged and weaker formation can exacerbate the problem of proppant embedment which may lead to fracture closure and reduction of fracture length and productivity as illustrated in Fig.3.17.

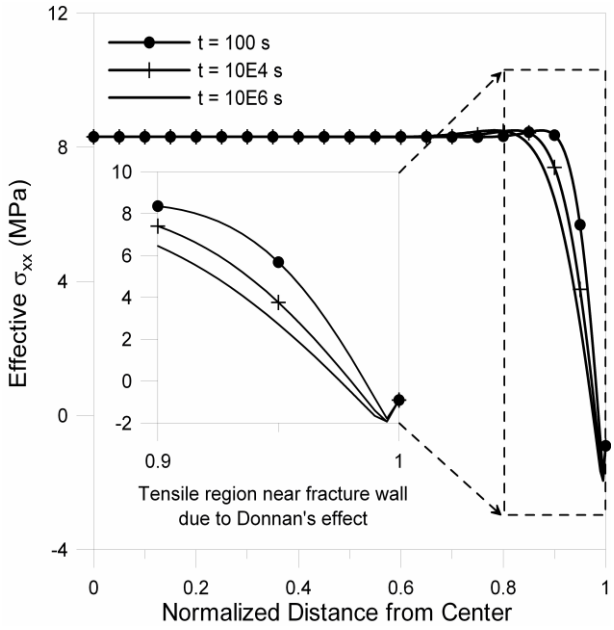


Fig.3.15-Distribution of the effective σ'_{xx} along the formation width

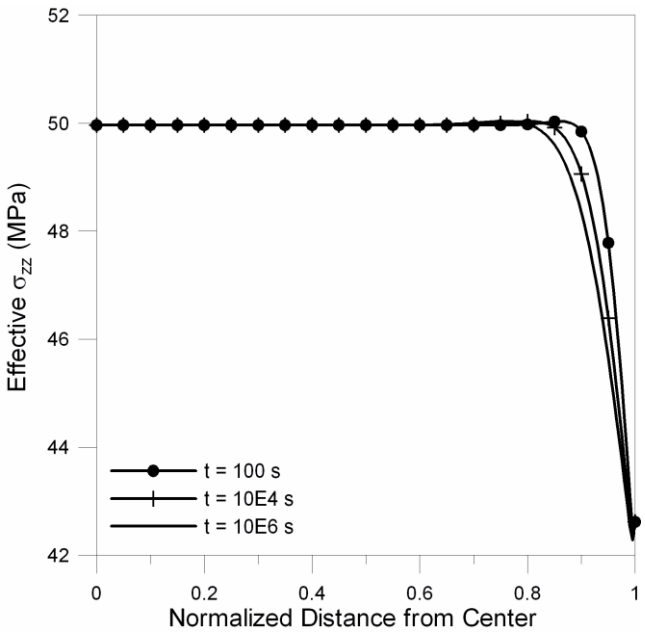


Fig.3.16-Distribution of the effective σ'_{zz} along the formation width

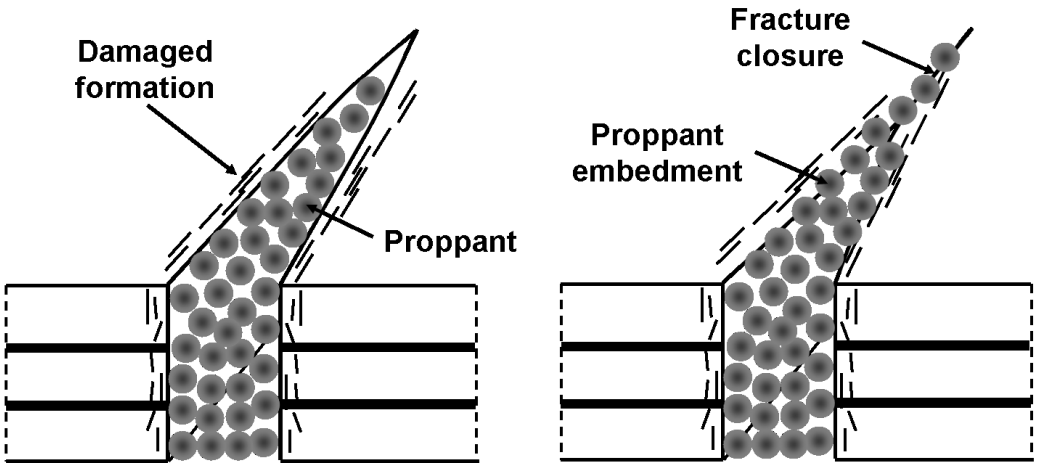


Fig.3.17-Illustration of fracture closure due to proppant embedment on a chemically damaged and weakened formation

According to Eq.2.30, the higher the formation CEC, the larger the induced pore pressure at the fracture surface and the more severe this tensile zone becomes. Thus, these phenomena can explain why high clay intervals are often observed as more "ductile" (or harder to create long fracture) from field operations. Practically, the chemically-induced tensile damages can be minimized by using a fracturing fluid with water activity equal to or slightly less than the native pore water activity so that the pore pressure peak due to fracturing fluid influx into the formation can be eliminated.

3.5.3 Diagenesis of Clay-rich Sediment

The diagenesis of clay-rich sediments into a shale formation can be simplified with 3 separate phases as illustrated in Fig.3.18. Initially, the sediments mixture contains the same fluid with the outer environment fluid as depicted in Fig.3.18a. However, the presence of fixed charges on the surfaces of the clay sediments requires expulsion of some of the pore fluid anion to the outer environment as discussed earlier. In addition, an osmotic pressure, p_o, develops at the interface of the sediments mixture and the outer environment according to the Donnan equilibrium condition. Since the permeability of the mixture is relatively high during deposition and early compaction, it is assumed that a uniform pore pressure with magnitude p_o exists throughout the mixture during these processes as illustrated in Fig.3.18b. It should be noticed that this osmotic pore pressure, p_o, shall remain constant as long as there is no change in the outer environment fluid activity or the formation CEC. The deposition of overlaying formations shall create additional pore pressure buildup inside the shale formation as shown in Fig.3.18c. The diffusion of this additional pore pressure buildup shall be governed by both the formation permeability and membrane efficiency.

In this numerical example, consider the diagenesis of a smectite-rich clay mixture with CEC = 20 meq./100 g, membrane efficiency of 0.2, and porosity of 20% in a channel depositional environment where the environment fluid has activity of 0.98. Applying Eq.2.30 the initial pore pressure due to Donnan equilibrium effect in the mixture is calculated to be 3.22 MPa. At the end of deposition process, the shale formation is assumed to have thickness of 40 m (i.e. b = 40 m) and width of 100 m (i.e. $2a$ = 100 m). The formation permeability and poroelastic properties used for simulation are those of

the Woodford shale. The depositional rate of overlaying sand layers with bulk density of 2.2 g/cc is assumed to be 1 m/year. As a result the formation is compacted under applied load $S(t)$ = 2.2 kPa/year × t. In this example, it is assumed that the outer environment fluid activity remains at a constant value of 0.98 and that the lateral expansion of the formation is assumed to be zero (i.e. $e(t) = 0$) which is valid in non-tectonic regions.

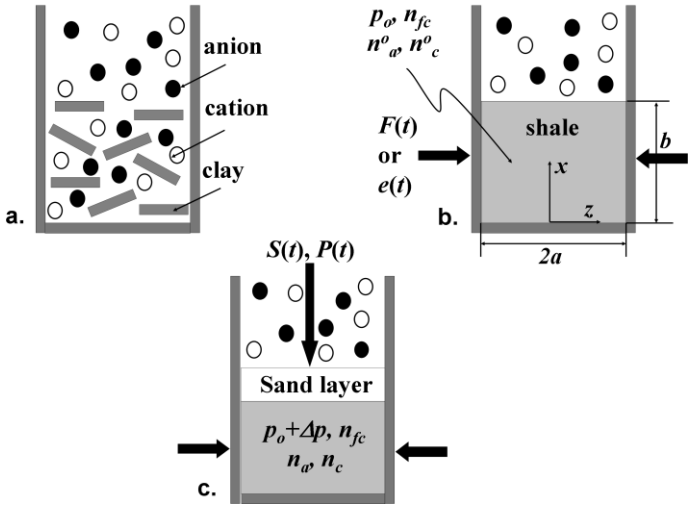


Fig.3.18-Schematic of simplified representation of diagenesis process

Shown in Fig.3.19 is the pore pressure evolution at the bottom of the shale formation. The pressure shown in Fig.3.18 is the amount of overpressure in the formation at a given time. The total formation pressure that is measured by down-hole tools is the sum of the overpressure and the hydrostatic pressure of the column of water above the formation. For the purpose of comparison, the plot for pore pressure evolution of a clean sand formation (i.e. CEC = 0, $\chi = 0$) and those of shale formations with different membrane efficiency (χ = 0, 0.2, 0.4) consolidated under the same conditions are also shown in Fig.3.18. It can be observed that the semi-permeable membrane behavior of the shale matrix hinders the exchange of the pore fluid ions with the outer environment

and, thus, effectively making the overall pore fluid diffusion process slower. As a result, the achieved steady-state pore pressure is larger for formation with higher membrane efficiency. Therefore, the usually observed high pressure in shale formations is attributable to the Donnan equilibrium effects and the semi-permeable behavior of the charged clay matrix in addition to the intrinsically low permeability of shale. However, it should be noticed that the actual process of diagenesis may involve clay mineral transformation and, thus, will be much more complicated than what can be captured by the analytical solution. In particular, while the transformation of the original smectite clay minerals with high CEC values (~20-25 meq./100 g) to illite and chlorite clay minerals with much lower CEC values (~5-10 meq./100 g) can reduce the magnitude of the Donnan equilibrium pressure. However, this transformation process releases additional pore water which can counter the reduction in the Donnan equilibrium pressure and create a very complicated pore pressure diffusion process.

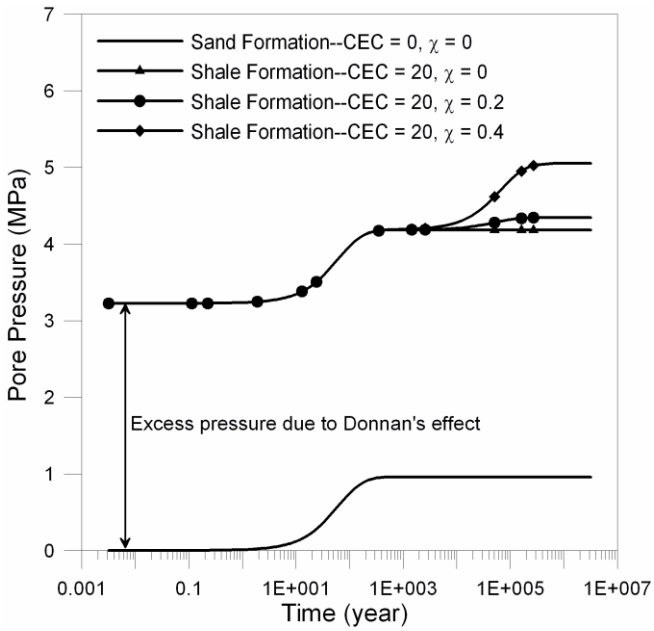


Fig.3.19-Pore pressure evolution at the bottom of the formation

3.6 Summary

In this chapter, the anisotropic porochemoelectroelastic for the Mandel's problem is given. Numerical examples illustrating the applications of the solutions for laboratory characterization, hydraulic fracturing, and diagenesis of shale are included.

In the context of laboratory characterization, the analyses show that the presence of negative fixed charges on the constituent clay minerals create an osmotic pressure at the interface of the sample and the testing fluid with magnitude proportional to the CEC of the sample according to the Donnan equilibrium condition. The results also show that the magnitude of the Donnan-induced pore pressure is rather small when compare to the load-generated pore pressure or activity-generate pore pressure. However, this Donnan-induced pore pressure when coupled with the pore pressure surge due to the applied load and the use of a high activity (i.e. low salinity) testing fluid can result in significant tensile effective stresses in the sample. For weak shale samples this induced tensile stress can lead to tensile damages of the samples. The results, thus, explain why some shales disintegrate when brought into contact with certain aqueous solutions while others do not. In addition, the complex pore pressure, stresses responses and distributions, and induced tensile damages can complicate the interpretation of experimental results for the effects of fluid chemistry on the rock matrix. Practically, it is recommended to gradually adjust the testing fluid salt concentration or applied load to the desired value so that excessive induced stress and pore pressure buildup become minimal.

Similarly, for hydraulic fracturing application, the Donnan equilibrium effects and the use of a low salinity (or high activity) fracturing fluid can induce a tensile damage zone

near the fracture surface. Consequently, the formation becomes weaker and can deform more easily under application of hydraulic pressure, leading to a wider fracture width. For the same pumping rate, a wider fracture width will result in a shorter fracture length. In addition, the damaged and weaker formation can exacerbate the problem of proppant embedment which may lead to fracture closure and reduction of fracture length and productivity. Practically, the use of fracturing fluid having similar activity with the formation native pore fluid can help to prevent the tensile damages and work for the advantage of the fracturing process.

Regarding the diagenesis of clay-rich sediments, the analyses show that the fixed charged of the clay minerals can induce a significant initial osmotic pressure in the formation. As the consolidation process continues, the semi-permeable membrane behavior of the shale matrix hinders the exchange of ions between the pore fluid and the outer environment, thus, effectively making overall the pore fluid diffusion process slower. As a result, the pore pressure buildup inside a shale formation can be much higher than in a clean sand formation under the same consolidation rate. Hence, taking into account the shale electrokinetic effects in basin modeling may give better predictions of overpressure issues in shale.

Chapter 4: The Full Cylinder Problem

4.1 Introduction

Laboratory characterizations of geo-material, especially shale rocks, often involve fluid exposure to simulate the in-situ conditions or to study the fluid effects on sample properties (*Chenevert*, 1998; *Hemphill et al.*, 2008; *Abousleiman et al.*, 2010). During these procedures, the sample pore pressure can be redistributed due to load application coupled with the induced osmotic flow from the electrochemical interactions between the pore fluid and the tested fluid. Simultaneously, the effective stress, strain and displacement distributions are modified which mislead interpretations of testing results.

The first analytical solution to address the coupled hydro-mechanical responses of an isotropic porous cylinder during uniaxial testing was presented by Amstrong et al. (1984). Since then, a number of analytical solutions accounting for different effects from testing conditions and material properties have been introduced. In particular, the analytical solution for transversely isotropic poroelastic cylinder under uniaxial testing and various mode of triaxial testing was derived by Abousleiman & Cui (1998). Extension of the solution to capture the viscoelastic behavior of shale was given by Abousleiman et al. (1996) and, later, generalized to anisotropic material by Hoang & Abousleiman (2010). Recently, Bunger (2009) presented the isotropic porochemoelastic solution of a cylinder under uniaxial loading condition. The dual-porosity and dual-permeability porochemoelastic solution for testing of naturally fractured cylindrical shale samples was later given by Nguyen (2010).

In this chapter, the anisotropic porochemoelectroelastic solution for cylinders is given to simulate some of the most common encountered laboratory testing configurations for shale rock. The solution is useful for simulate and analyze the experimental testing results as will be illustrated with the unconfined compression test and pressure transmission test.

4.2 Problem Descriptions

Shown in Fig.4.1 are two common laboratory testing conditions often imposed on geo- and bio- samples. The sample is cored orthogonal to the apparent bedding plane so that the material isotropic plane lies horizontally. In Fig.4.1a, an axial load $F(t)$ (load-control mode) or an axial strain $e(t)$ (stroke-control mode) is applied to the sample top and bottom while a confining pressure $S_{rr}(t)$ is applied laterally. Meanwhile, the tested sample is exposed to a testing solution with solute mole fraction of $n_s^{sol}(t)$ at hydraulic pressure $p_o(t)$. This configuration depicts a sample being tested for fluid exposure effects under a triaxial setup. When there is no applied confining pressure (i.e. $S_{rr}(t) = 0$), the set up becomes an unconfined compression test (or uniaxial test). On the other hand, when $S_{rr}(t) = p_o(t) = F(t) = 0$, the set up turns into a free swelling test. Shown in Fig.4.1b is the setup of the K_o test (also known as oedometer or uniaxial strain test in soil mechanics) in which the sample sandwiched between two rigid porous plates and confined laterally by a rigid and impermeable ring. The top and bottom of the sample can also be exposed to fluid with solute mole fraction of n_s^{sol} and hydraulic pressure $p_o(t)$ as in the previous setup to characterize the fluid effects on sample under 1-D consolidation.

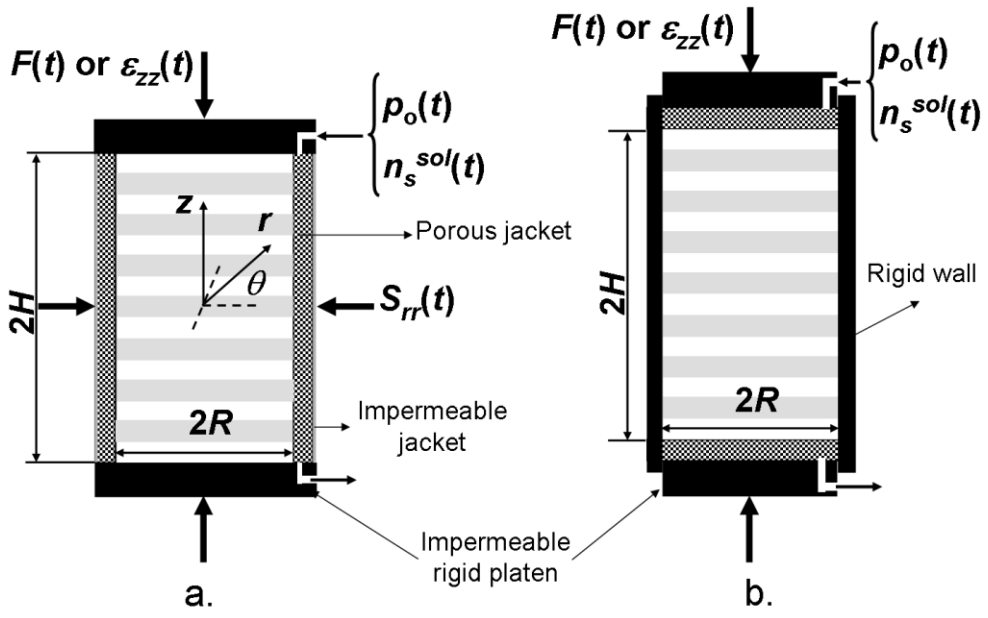


Fig.4.1-Schematic of common laboratory testing conditions for cylindrical samples

The experiment setup depicted in Fig.4.1b can also be used to simulate the pressure transmission test as shown in Fig.4.2 (*Ewy & Stankovic*, 2010; *Chen et al.*, 2010). The test can be briefly described as imposing a testing fluid with different chemical composition than the native pore fluid on one end of a cylindrical sample and record the pore pressure change at the other end of the sample. The recorded pore pressure is then used to estimate the sample flow properties such as permeability, membrane efficiency, and effective ion transport coefficients by best-fitting an analytical solution. Although the pressure transmission test is often conducted under confining pressure instead of uniaxial strain condition as depicted in Fig.4.1b, the flow regime during a pressure transmission test is still a 1-D flow along the *z*-direction similar to that of the setup shown in Fig.4.1b. Hence, the solution for Fig.4.1b can be used as a first order approximation to analyze the poroelastic pressure transmission test. Solutions

accounting for the effects of sample lateral expansion can only be achieved using numerical simulation and is beyond the scope of this research.

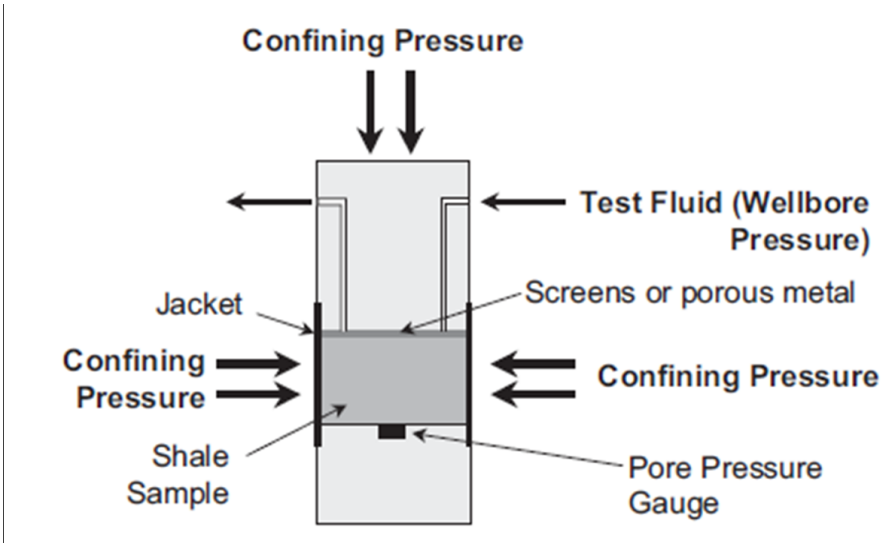


Fig.4.2-Schematic of the pressure transmission test as taken from Ewy & Stankovic (2010)

For the testing conditions depicted in Fig.4.1a, the boundary conditions imposed at the sample surface ($r = R$) are as follows

$$\sigma_{rr} = S_{rr}(t) \tag{4.1}$$

$$p = p_o(t) + \frac{RT}{V_f^o}\left[\sqrt{n_{fc}^2 + 4\left[n_s^{sol}(t)\right]^2} - 2n_s^{sol}(t)\right] = P(t) \tag{4.2}$$

$$p_a = \frac{RT}{V_f^o}\left[n_s^{sol}(t) + \Delta n_a^{sol/sample}(t)\right] = P_a(t) \tag{4.3}$$

$$p_c = \frac{RT}{V_f^o}\left[n_s^{sol}(t) + \Delta n_c^{sol/sample}(t)\right] = P_c(t) \tag{4.4}$$

Whereas for the testing conditions depicted in Fig.4.1b, the boundary conditions at $z = H$ are as follows

$$p = P(t) \tag{4.5}$$

$$p_a = P_a(t) \tag{4.6}$$

$$p_c = P_c(t) \tag{4.7}$$

with $\sigma_{zz} = F(t)/\pi R^2$ for load-control mode and $\varepsilon_{zz} = e(t)$ for stroke-control mode.

4.3 Analytical Solutions

4.3.1 Solutions for Unconfined Compression and Triaxial Test

As depicted in Fig.4.1, the problem is axisymmetric which leads to vanishing of all shear stresses ($\sigma_{r\theta} = \sigma_{\theta z} = \sigma_{rz} = 0$). Hence, the constitutive relations in the cylindrical coordinate system are expressed as follows

$$\sigma_{rr} = C_{11}\varepsilon_{rr} + C_{12}\varepsilon_{\theta\theta} + C_{13}\varepsilon_{zz} + \alpha_1 p \tag{4.8a}$$

$$\sigma_{\theta\theta} = C_{12}\varepsilon_{rr} + C_{11}\varepsilon_{\theta\theta} + C_{13}\varepsilon_{zz} + \alpha_1 p \tag{4.8b}$$

$$\sigma_{zz} = C_{13}\varepsilon_{rr} + C_{13}\varepsilon_{\theta\theta} + C_{33}\varepsilon_{zz} + \alpha_3 p \tag{4.8c}$$

$$\zeta = -\alpha_1\varepsilon_{rr} - \alpha_1\varepsilon_{\theta\theta} - \alpha_3\varepsilon_{zz} + \frac{1}{M}p = -\alpha_1\varepsilon - \alpha_3\varepsilon_{zz} + \frac{1}{M}p \tag{4.8d}$$

$$\zeta_a = n_a^o\left[-\alpha_1\varepsilon - \alpha_3\varepsilon_{zz} + \frac{1}{M}p\right] + \phi^o n_a \tag{4.8e}$$

$$\zeta_c = n_c^o\left[-\alpha_1\varepsilon_{rr} - \alpha_3\varepsilon_{zz} + \frac{1}{M}p\right] + \phi^o n_c \tag{4.8f}$$

The equilibrium equations and strain-displacement equations for axisymmetric problems are

$$\frac{\partial\sigma_{rr}}{\partial r} + \frac{\sigma_{rr} - \sigma_{\theta\theta}}{r} = 0 \tag{4.9}$$

$$\frac{\partial\sigma_{zz}}{\partial z} = 0 \tag{4.10}$$

$$\varepsilon_{rr} = \frac{\partial u_r}{\partial r} \tag{4.11}$$

$$\varepsilon_{\theta\theta} = \frac{u_r}{r} \tag{4.12}$$

$$\varepsilon_{zz} = \frac{\partial u_z}{\partial z} \tag{4.13}$$

The mass and electrical charge balance equations for the whole fluid and its individual components

$$\frac{\partial \zeta}{\partial t} = -\vec{\nabla}.\vec{q} \tag{4.14}$$

$$\frac{\partial \zeta_a}{\partial t} = -V_o^f \vec{\nabla}.\vec{J}^a = -V_o^f \vec{\nabla}.(\vec{J}^{a,d} + n_a \vec{q} / V_o^f) \tag{4.15}$$

$$\frac{\partial \zeta_c}{\partial t} = -V_o^f \vec{\nabla}.\vec{J}^c = -V_o^f \vec{\nabla}.(\vec{J}^{c,d} + n_c \vec{q} / V_o^f) \tag{4.16}$$

$$\frac{\partial \rho_e}{\partial t} = -\vec{\nabla}.\vec{I} \tag{4.17}$$

with $\vec{\nabla} = \frac{\partial}{\partial r}\hat{r} + \frac{\partial}{\partial z}\hat{z}$ is the gradient vector in the cylindrical coordinate system taking into account the axisymmetric conditions.

The problem solution is obtained using Laplace transform technique. Under the Laplace transform domain, substitution of the stress-strain relations into the equilibrium equation in radial direction yields

$$C_{11}\frac{d\tilde{\varepsilon}}{dr} + \alpha_1 \frac{d\tilde{p}}{dr} = 0 \tag{4.18}$$

which gives $\tilde{\varepsilon} = -(\alpha_1 / C_{11})\tilde{p} + C_o$ where C_o is a constant of integration. Follow Nguyen & Abousleiman (2010), substituting the stress-strain relations and the transport equations in the radial direction into the mass and electrical charge balance equations while assuming electrostatic condition ($\partial \rho_e / \partial t = 0$), and ignoring the ion transport by advection terms gives

$$s\begin{bmatrix} -\alpha_1 & \frac{1}{M} & 0 & 0 \\ -n_a^o\alpha_1 & \frac{n_a^o}{M} & \phi^o\frac{V_f^o}{RT} & 0 \\ -n_c^o\alpha_1 & \frac{n_c^o}{M} & 0 & \phi^o\frac{V_f^o}{RT} \end{bmatrix}\begin{bmatrix} \widetilde{\varepsilon} \\ \widetilde{p} \\ \widetilde{p}_a \\ \widetilde{p}_c \end{bmatrix} = [D]\nabla^2\begin{bmatrix} \widetilde{p} \\ \widetilde{p}_a \\ \widetilde{p}_c \end{bmatrix} + s\alpha_3\begin{bmatrix} 1 \\ n_a^o \\ n_c^o \end{bmatrix}\widetilde{\varepsilon}_{zz} \tag{4.19}$$

with

$$[D] = \begin{bmatrix} \kappa & -\chi\kappa & -\chi\kappa \\ n_a^o(1-\chi)\kappa & \frac{D_{eff}^a V_f^o}{RT} - n_a^o(1-\chi)\chi\kappa & -n_a^o(1-\chi)\chi\kappa \\ n_c^o(1-\chi)\kappa & -n_c^o(1-\chi)\chi\kappa & \frac{D_{eff}^c V_f^o}{RT} - n_c^o(1-\chi)\chi\kappa \end{bmatrix} \tag{4.20}$$

and $\nabla^2 = d^2/dr^2 + (1/r)d/dr$. The tilde sign denotes Laplace transform solution and s is the Laplace variable. Substitution of the results of Eq.4.18 into Eq.4.19 gives a system of differential equations involving only the pressure terms ($\widetilde{\varepsilon}_{zz}$ is known variable from loading conditions)

$$\underbrace{s\begin{bmatrix} \frac{\alpha_1^2}{C_{11}} + \frac{1}{M} & 0 & 0 \\ n_a^o\left(\frac{\alpha_1^2}{C_{11}} + \frac{1}{M}\right) & \phi^o\frac{V_f^o}{RT} & 0 \\ n_c^o\left(\frac{\alpha_1^2}{C_{11}} + \frac{1}{M}\right) & 0 & \phi^o\frac{V_f^o}{RT} \end{bmatrix}}_{[Y]}\begin{bmatrix} \widetilde{p} \\ \widetilde{p}_a \\ \widetilde{p}_c \end{bmatrix} = [D]\nabla^2\begin{bmatrix} \widetilde{p} \\ \widetilde{p}_a \\ \widetilde{p}_c \end{bmatrix} + s\alpha_1\begin{bmatrix} 1 \\ n_a^o \\ n_c^o \end{bmatrix}C_o + s\alpha_3\begin{bmatrix} 1 \\ n_a^o \\ n_c^o \end{bmatrix}\widetilde{\varepsilon}_{zz} \tag{4.21}$$

Applying the matrix diagonalization technique (Farlow, 1993), the general solution of Eq.4.21 can be obtained as follows

$$\begin{cases} \widetilde{p} = f_1 C_o + \sum_{i=1}^{3} m_{1i} C_i I_o(\xi_i r) + g_1 \widetilde{\varepsilon}_{zz} \\ \widetilde{p}_a = f_2 C_o + \sum_{i=1}^{3} m_{2i} C_i I_o(\xi_i r) + g_2 \widetilde{\varepsilon}_{zz} \\ \widetilde{p}_c = f_3 C_o + \sum_{i=1}^{3} m_{3i} C_i I_o(\xi_i r) + g_3 \widetilde{\varepsilon}_{zz} \end{cases} \tag{4.22}$$

with C_i are constants of integration to be determined from the boundary conditions, $I_n(\xi_i r)$ is the modified Bessel function of the first kind of order n, $\xi_i = \sqrt{s/\lambda_i}$, in which λ_i are the eigenvalues of the matrix $[Z]=[Y]^{-1}[D]$ with $\{m_{1i}, m_{2i}, m_{3i}\}$ as its corresponding eigenvectors, $[f]=\alpha_1[Y]^{-1}\begin{bmatrix}1 & n_a^o & n_c^o\end{bmatrix}^T$, and $[g]=\alpha_3[Y]^{-1}\begin{bmatrix}1 & n_a^o & n_c^o\end{bmatrix}^T$. Once the pressure solutions are derived, the general solutions for stress, strain, and displacement are straightforward to obtain using the stress-strain relations and strain-displacement relations. For brevity of presentation, these derivations shall not be presented here.

For the stroke-control testing conditions, the constant of integrations take the following form

$$\begin{bmatrix} C_1 \\ C_2 \\ C_3 \end{bmatrix} = [G]^{-1} \begin{bmatrix} \widetilde{P} + \dfrac{2\eta\widetilde{e}}{\beta} f_1 - \dfrac{2}{\beta}\widetilde{S}_{rr} f_1 - \widetilde{e} g_1 \\ \widetilde{P}_a + \dfrac{2\eta\widetilde{e}}{\beta} f_2 - \dfrac{2}{\beta}\widetilde{S}_{rr} f_2 - \widetilde{e} g_2 \\ \widetilde{P}_c + \dfrac{2\eta\widetilde{e}}{\beta} f_3 - \dfrac{2}{\beta}\widetilde{S}_{rr} f_3 - \widetilde{e} g_3 \end{bmatrix} \tag{4.23}$$

and

$$C_o = \frac{2}{\beta}\left(\widetilde{S}_{rr} - \eta\widetilde{e} - \frac{2G}{C_{11}} \alpha_1 \sum_{i=1}^{3} \frac{m_{1i} I_1(\xi_i R) C_i}{\xi_i R} \right) \tag{4.24}$$

with the matrix [G] components expressed as

$$G_{ij} = -\frac{4G}{\beta C_{11}} \alpha_1 f_i \frac{m_{1j} I_1(\xi_j R)}{\xi_j R} + m_{ij} I_o(\xi_j R) \tag{4.25}$$

where

$$\beta = C_{11} + C_{12} + 2Gf_1\alpha_1 / C_{11} \tag{4.26a}$$

$$\eta = C_{13} + g_1 G\alpha_1 / C_{11} \tag{4.26b}$$

For the load-control testing conditions, $\widetilde{\varepsilon}_{zz}$ takes the following form

$$\widetilde{\varepsilon}_{zz} = \frac{1}{b}\left[\frac{\widetilde{F}}{\pi R^2} - hC_o - 2\left(\alpha_3 - \frac{C_{13}\alpha_1}{C_{11}}\right)\sum_{i=1}^{3}\frac{m_{1i}C_i I_1(\xi_i R)}{\xi_i R}\right] \tag{4.27}$$

and the constant of integrations become

$$\begin{bmatrix} C_1 \\ C_2 \\ C_3 \end{bmatrix} = [G]^{-1}\begin{bmatrix} \widetilde{P} - \left(\widetilde{S}_{rr} - \dfrac{\eta\widetilde{F}}{b\pi R^2}\right)\left(f_1 - \dfrac{h}{b}g_1\right)\Big/\left(\dfrac{\beta}{2} - \dfrac{\eta h}{b}\right) \\ \widetilde{P}_a - \left(\widetilde{S}_{rr} - \dfrac{\eta\widetilde{F}}{b\pi R^2}\right)\left(f_2 - \dfrac{h}{b}g_2\right)\Big/\left(\dfrac{\beta}{2} - \dfrac{\eta h}{b}\right) \\ \widetilde{P}_c - \left(\widetilde{S}_{rr} - \dfrac{\eta\widetilde{F}}{b\pi R^2}\right)\left(f_3 - \dfrac{h}{b}g_3\right)\Big/\left(\dfrac{\beta}{2} - \dfrac{\eta h}{b}\right) \end{bmatrix} \tag{4.28}$$

and

$$C_o = \frac{1}{\beta/2 - \eta h/b}\left\{\widetilde{S}_{rr} - \frac{\eta\widetilde{F}}{b\pi R^2} - \left[\frac{2\eta}{b}\left(\alpha_3 - \frac{C_{13}\alpha_1}{C_{11}}\right) - \frac{2G}{C_{11}}\alpha_1\right][d]^T[C]\right\} \tag{4.29}$$

where the [G] matrix components are expressed as

$$G_{ij} = m_{ij}I_o(\xi_j R) - 2\left(\alpha_3 - \frac{C_{12}}{C_{11}}\alpha_1\right)\left[\frac{g_i}{b} + \frac{\dfrac{\eta}{b} - \dfrac{G\alpha_1}{C_{11}}}{\dfrac{\beta}{2} - \dfrac{\eta h}{b}}\left(f_i - \frac{h}{b}g_i\right)\right]\frac{m_{1j}I_1(\xi_j R)}{\xi_j R} \tag{4.30}$$

and

$$b = \alpha_3 g_1 - C_{13}g_1 / C_{11} \tag{4.31a}$$

$$h = C_{13} + \alpha_3 f_1 - C_{13}\alpha_1 f_1 / C_{11} \tag{4.31b}$$

4.3.2 Solutions for Confined Compression Test

The experimental setup of this problem leads to

$$u_r = u_\theta = 0; \quad \varepsilon_{rr} = \varepsilon_{\theta\theta} = 0; \quad q_r = q_\theta = 0 \tag{4.32}$$

and all non-trivial variables are dependent on *z* and *t* only. Under the Laplace transform domain, substitution of the stress-strain relations into the equilibrium equation in the z-direction yields

$$C_{33}\frac{d\tilde{\varepsilon}_{zz}}{dz} + \alpha_3\frac{d\tilde{p}}{dz} = 0 \tag{4.33}$$

Applying the same steps to obtain Eq.4.19 results in the following diffusion type equations

$$\underbrace{s\begin{bmatrix} -\alpha_3 & 1/M & 0 & 0 \\ -n_a^o\alpha_3 & n_a^o/M & \phi^o\left(V_f^o/RT\right) & 0 \\ -n_c^o\alpha_3 & n_c^o/M & 0 & \phi^o\left(V_f^o/RT\right) \end{bmatrix}}_{[Y]}\begin{bmatrix} \tilde{\varepsilon}_{zz} \\ \tilde{p} \\ \tilde{p}_a \\ \tilde{p}_c \end{bmatrix} = [D]\frac{d^2}{dz^2}\begin{bmatrix} \tilde{p} \\ \tilde{p}_a \\ \tilde{p}_c \end{bmatrix} \tag{4.34}$$

Following the same procedure described in the previous section, the solution for $\tilde{p}$, $\tilde{p}_a$, $\tilde{p}_c$ are

$$\begin{cases} \tilde{p} = f_1 C_o + \sum_{i=1}^{3} m_{1i}\left(C_i e^{\sqrt{\xi_i}z} + C_{i+3}e^{-\sqrt{\xi_i}z}\right) \\ \tilde{p}_a = f_2 C_o + \sum_{i=1}^{3} m_{2i}\left(C_i e^{\sqrt{\xi_i}z} + C_{i+3}e^{-\sqrt{\xi_i}z}\right) \\ \tilde{p}_c = f_3 C_o + \sum_{i=1}^{3} m_{3i}\left(C_i e^{\sqrt{\xi_i}z} + C_{i+3}e^{-\sqrt{\xi_i}z}\right) \end{cases} \tag{4.35}$$

with C_o, C_i, C_{i+3} (i = 1, 2, 3) are constant of integrations. $\xi_i = \sqrt{s/\lambda_i}$ where λ_i are the eigenvalues of the matrix $[Z] = [Y]^{-1}[D]$ with $\{m_{1i}, m_{2i}, m_{3i}\}$ as its corresponding eigenvectors, and $[f] = \alpha_1[Y]^{-1}\begin{bmatrix} 1 & n_a^o & n_c^o \end{bmatrix}^T$. Since the problem is symmetric through the *x*-*y* plane at $z = 0$, $d\tilde{p}/dz = d\tilde{p}_a/dz = d\tilde{p}_c/dz = 0$ which leads to $C_i = C_{i+3}$. Hence, Eq.4.35 reduces to

$$\begin{cases} \widetilde{p} = f_1 C_o + 2\sum_{i=1}^{3} m_{1i} C_i \cosh\left(\sqrt{\xi_i}\, z\right) \\ \widetilde{p}_a = f_2 C_o + 2\sum_{i=1}^{3} m_{2i} C_i \cosh\left(\sqrt{\xi_i}\, z\right) \\ \widetilde{p}_c = f_3 C_o + 2\sum_{i=1}^{3} m_{3i} C_i \cosh\left(\sqrt{\xi_i}\, z\right) \end{cases} \tag{4.36}$$

Using the boundary conditions described in Fig.4.1b, it can be shown that for load-control testing conditions

$$C_o = \widetilde{F} / (C_{33} \pi R^2) \tag{4.37}$$

$$\begin{bmatrix} C_1 \\ C_2 \\ C_3 \end{bmatrix} = \frac{1}{2} [G]^{-1} \begin{bmatrix} \widetilde{P} - f_1 \widetilde{F} / \left(C_{33} \pi R^2\right) \\ \widetilde{P}_a - f_2 \widetilde{F} / \left(C_{33} \pi R^2\right) \\ \widetilde{P}_c - f_3 \widetilde{F} / \left(C_{33} \pi R^2\right) \end{bmatrix} \tag{4.38}$$

with

$$G_{ij} = m_{ij} \cosh\left(\sqrt{\xi_j} H\right)$$

On the other hand, for the stroke-control testing conditions, the coefficients of integrations become

$$C_o = \frac{\widetilde{e}}{\eta} + \frac{\alpha_3}{\eta C_{33}} \sum_{i=1}^{3} m_{1i} C_i \cosh\left(\sqrt{\xi_i} H\right) \tag{4.39}$$

$$\begin{bmatrix} C_1 \\ C_2 \\ C_3 \end{bmatrix} = [H]^{-1} \begin{bmatrix} \widetilde{P} - f_1 \widetilde{e} / \gamma \\ \widetilde{P}_a - f_2 \widetilde{e} / \gamma \\ \widetilde{P}_c - f_3 \widetilde{e} / \gamma \end{bmatrix} \tag{4.40}$$

with

$$H_{ij} = (2 + \alpha_3 f_i / C_{33}) m_{ij} \cosh\left(\sqrt{\xi_j} H\right) \tag{4.41}$$

$$\gamma = 1 - f_1 \alpha_3 / C_{33} \tag{4.42}$$

4.4 Solutions Validations for Special Cases

As previously discussed, when the pore fluid and the testing fluid are both free of salt (i.e. $a_{sol} = a^o_f = 1$), the current solutions shall reduce to the poroelastic solutions regardless of the sample membrane efficiency (χ) or cation exchange capacity (CEC). Similarly, if the specimen is free of clay (i.e. CEC = 0, $\chi = 0$), the current solutions will also recover the poroelastic solutions for any difference in activities between the outer fluid and the native pore fluid as ions are free to transport between the outer fluid and pore fluid in the absence of the membrane and, thus, the water does not need to flow from one place to another in order to balance the difference in ion concentration. In this section, the analytical solution for tri-axial testing is validated by comparing the results from the current solution when CEC = 0 and $\chi = 0$ with those from the transversely isotropic poroelastic solutions of Abousleiman & Cui (1998) with elastic and poroelastic parameters used for simulation are those from the Trafalgar shale as summarized in Table 3.1. It should be noticed that the specimen radius (R) is 0.032 m instead of 0.1 m as reported in Abousleiman & Cui (1998) which is a typo. In addition, the convention of stress and strain in Abousleiman & Cui (1998) is tension positive while in this paper compressive stresses and strains are positive.

Shown in Fig.4.3-Fig.4.5 are, respectively, the comparison for the pore pressure, axial stress evolution at the center of the sample ($r = 0$), and the tangential stress at the sample edge ($r = R$) for different values of Young's modulus anisotropic ratio (nE = E_1/E_3) while the Poisson's ratio is assumed to be isotropic at $\nu = 0.189$. The agreement between the results has, thus, confirmed the behavior and the correctness of the current solutions in these special cases.

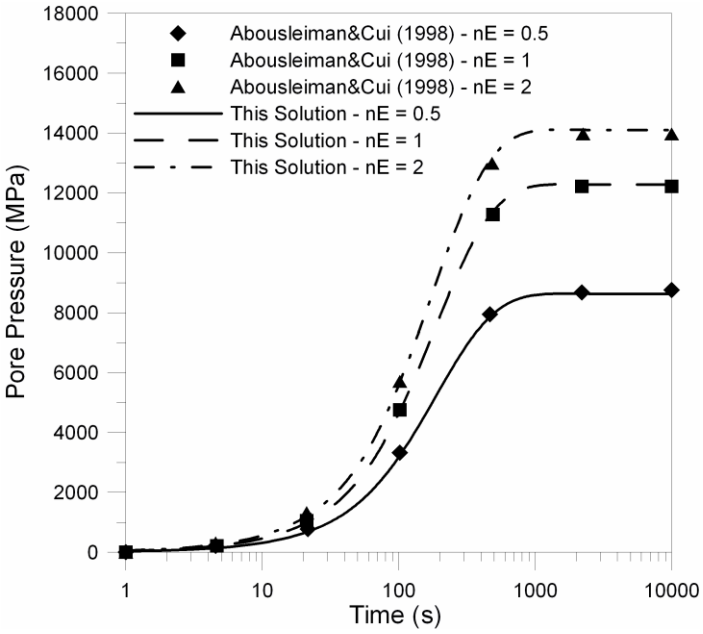


Fig.4.3- Comparison of pore pressure at the center of the sample ($r = 0$) from the current solutions when CEC=$\chi = 0$ to the results in Abousleiman & Cui (1998)

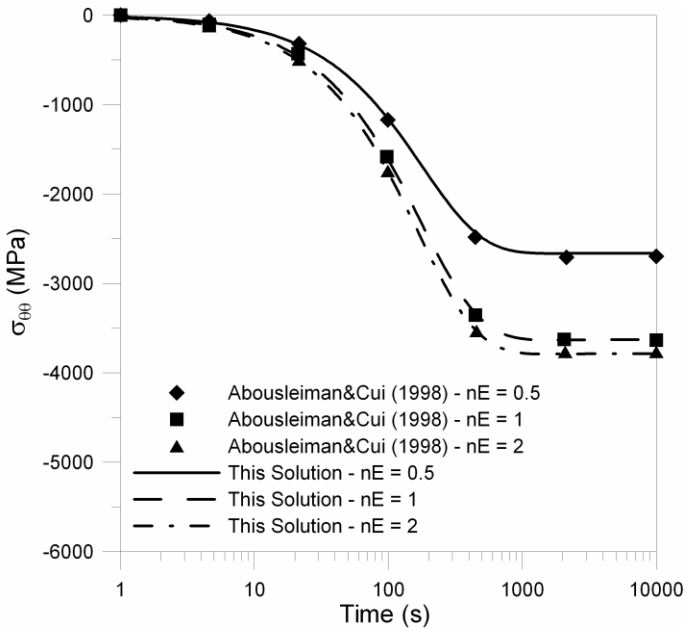


Fig.4.4- Comparison of tangential stress at the edge of the sample ($r = R$) from the current solutions when CEC=$\chi = 0$ to the results in Abousleiman & Cui (1998)

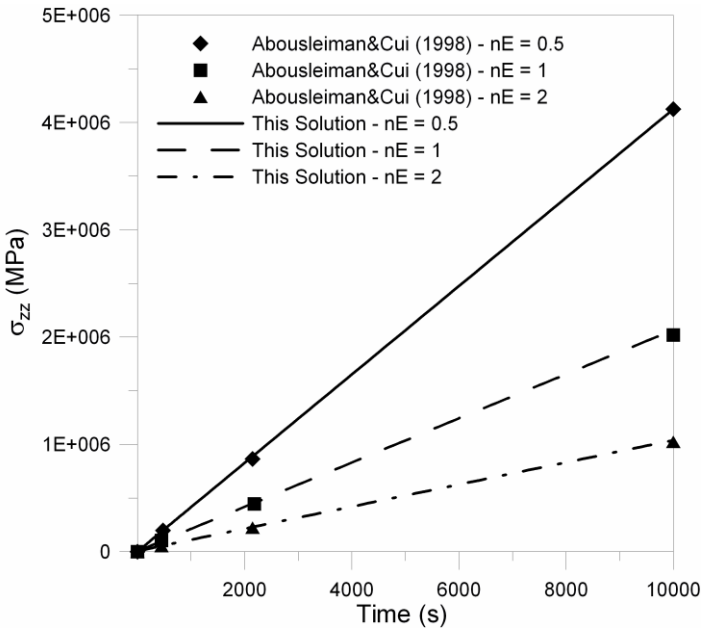


Fig.4.5- Comparison of axial stress at the center of the sample (*r = 0*) from the current solutions when CEC=χ = 0 to the results in Abousleiman & Cui (1998)

4.5 Examples of Applications

4.5.1 Laboratory Testing for the Fluid Chemistry Effects

Consider a Woodford shale specimen with radius of 2 cm (i.e. R = 2 cm), thickness of 8 cm (i.e. h = 8 cm) with geological and elastic properties identical to those used in the previous example of Chapter 3 (see Table 3.2). The sample is initially free of any stresses, pore pressure, and is saturated with pore fluid having activity a_o^f = 0.89. The specimen is then submerged into a chamber containing testing fluid with a_{sol} = 0.87 and without being subjected to hydraulic or confinement pressure (i.e. P(t) = S(t) = 0 MPa). Simultaneously, an axial load F = 0.4 kN is applied to the rigid plates to assure a good contact between the rigid platens and the specimen such that acoustic monitoring can be achieved. Shown in Fig.4.6 is the pore pressure, p^{total}, distribution along the radial direction for the case of low testing fluid activity (a_{sol} = 0.87 > a_o^f = 0.89) at different times with the normalized distance from sample center defined as $\bar{r} = r / R$. The pore

pressure jump with magnitude of 0.29 MPa at the sample edge ($\bar{r} = 1$) corresponds to the osmotic pressure created by the Donnan equilibrium effect as previously discussed. Due to the application of the axial stress, an initial pore pressure surge with magnitude of 0.50 MPa is observed inside the sample. The Mandel-Cryer effect can be clearly observed from the plot at t = 5 s when the pore pressure at the sample center reaches a value higher than the original pore pressure jump. The pore pressure drop near the sample edge at t = 5 s is a result of pore water being drawn out of the sample due to the higher salt concentration in the testing fluid. As time elapses, more and more water is drawn out of the sample and the pressure drop front propagates toward the center. Finally, after approximately 48 hrs, the pore pressure inside the sample approaches an equilibrium value equal to the Donnan equilibrium pressure.

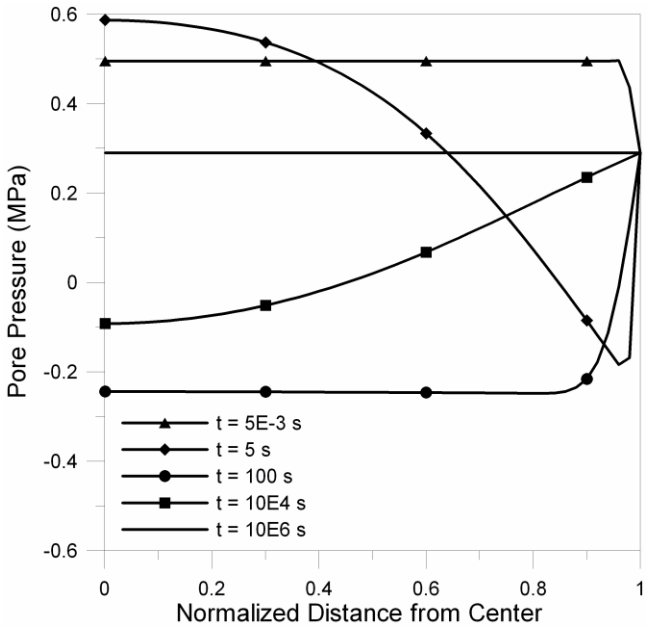


Fig.4.6-Distribution of pore pressure p^{total} along the radial direction (a_{sol} = 0.87)

The evolution of the pore pressure at the center of the sample is summarized in Fig.4.7. Also, shown in Fig.4.7 is the comparison of the pore pressure evolution at the center of the sample between the cylindrical geometry and rectangular geometry. It can be

observed that the Mandel-Cryer effect is more significant in the cylindrical geometry and the diffusion process in the cylindrical geometry appear to be faster than in the rectangular geometry. Similar observations have been reported in Nguyen (2010) when studying the Mandel-type problem for dual porosity and dual permeability medium.

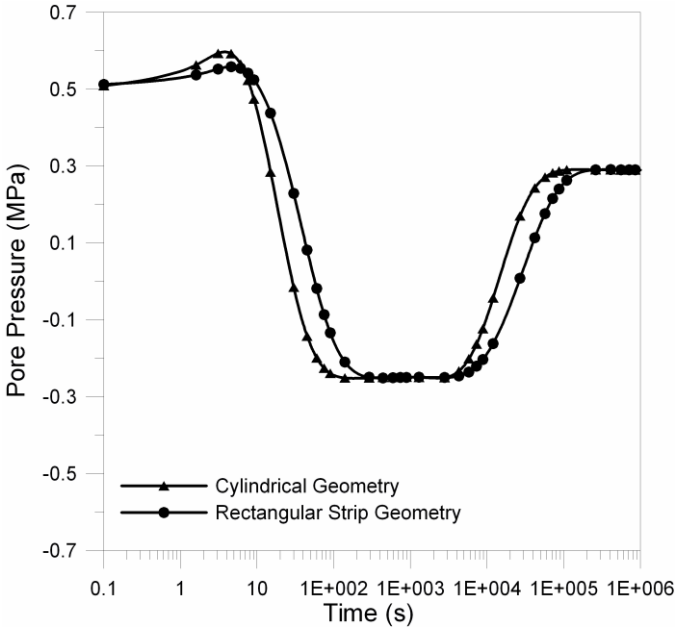


Fig.4.7-Evolution of pore pressure at the center of the sample (a_{sol} = 0.87)

Shown in Figs.4.8-4.10 are respectively the distributions of effective stresses σ'_{rr}, $\sigma'_{\theta\theta}$, and σ'_{zz} along the radial direction for the case of low activity mud. The results show that significant tensile stresses can develop at and near the sample edge due the Donnan equilibrium effect. Similar to earlier discussions in Chapter 3, these induced tensile stresses are unlikely to cause tensile damages on the tested Woodford sample given that the Woodford shale tensile strength has been measured to be 4 -12 MPa. It should also be noticed that the total radial stress $\sigma_{rr}^{total} \neq 0$ despite there is not applied confining pressure on the sample. In other words, the effective radial stress becomes $\sigma'_{rr} = \sigma_{rr}^{total} - p^{total}$ instead of $\sigma'_{xx} = 0 - p^{total}$ as in the case of the rectangular strip problem of Chapter 3.

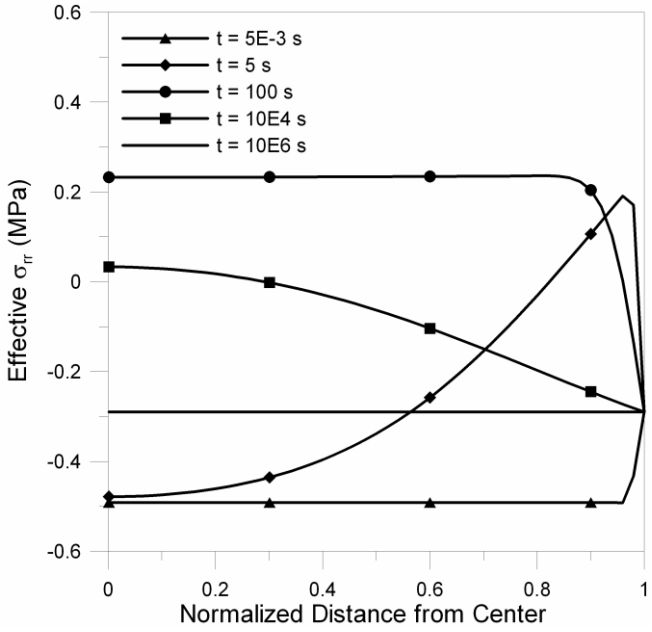


Fig.4.8-Distribution of the effective σ'_{rr} along the radial direction (a_{sol} = 0.87)

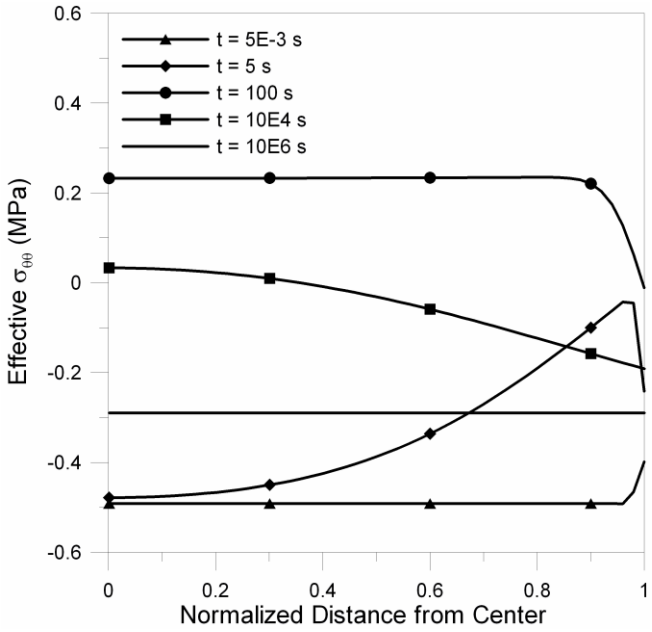


Fig.4.9-Distribution of the effective $\sigma'_{\theta\theta}$ along the radial direction (a_{sol} = 0.87)

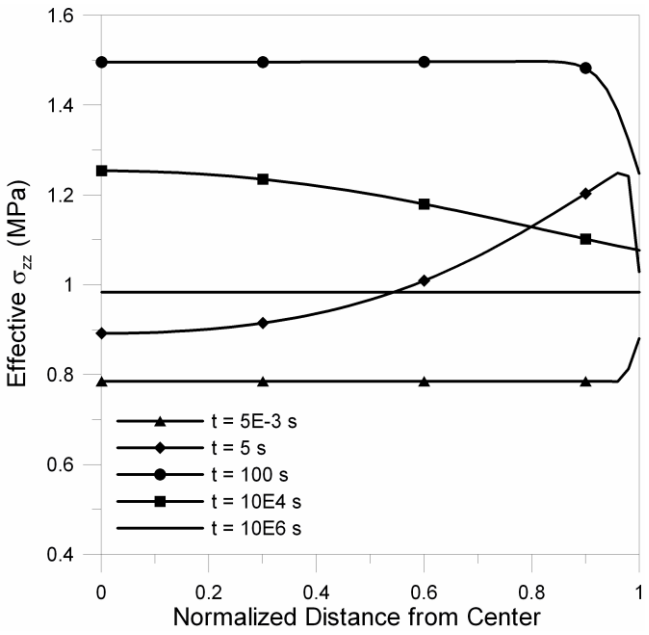


Fig.4.10-Distribution of the effective σ'_{zz} along the radial direction (a_{sol} = 0.87)

4.5.2 Determination of the Coupled Hydro-Electro-Chemical Flow Parameters Using the Pressure Transmission Test Data

In this section, the solution for confined compression test (presented in section 4.3.2) will be used to simulate the pressure transmission test data and result reported by Chen et al. (2010). The shale sample native pore fluid activity is determined to be 0.96 and the sample is exposed to a testing fluid with activity a_{sol} = 0.8 at 1000 psi hydraulic pressure. Others geological and mechanical properties of the samples are assumed and collected from the literature as summarized in Table 4.1. This simulation aims at determining the permeability and membrane efficiency (χ) of the sample by varying these variables to obtain a best fit to the reported results. It is noteworthy that the poroelastic effects have been ignored in the solution of Chen et al. (2010) (hence, the solution shall be referred simply as the diffusion solution in this study). Thus, simulation using a rock permeability k = 0.068 nD and membrane efficiency χ = 0.043

as estimated by Chen et al. (2010) while varying the rock poroelastic properties to obtain a best fit is also included to illustrate the poroelastic effects on determination of specimen flow properties.

Table 4. 1-Summary of shale sample properties use for simulation

Properties	Values	Notes
Porosity (%)	14	Assumed
CEC (meq/100 gr)	20	Ewy & Stankovic (2010) Use same shale with this example
k (nD)	4-8	Ewy & Stankovic (2010)
Grain density (g/cc)	2.68-2.72	//
Effective diffusion coefficient of Na^+ (m^2/s)	1.60×10^{-10}	Assumed: $D^{Na+} = 1.33\times10^{-9}$, $\tau=1$
Effective diffusion coefficient of Cl^- (m^2/s)	2.44×10^{-10}	Assumed: $D^{Cl-} = 2.03\times10^{-9}$, $\tau=1$
K (MPa)	1217	Assumed
ν	0.25	//
E (MPa)	1850	//
K_S (MPa)	40000	//
M (MPa)	20000	//

Shown in Fig.4.11 is the comparison between the recorded down stream pore pressure and the simulated pore pressure at different combination of k and χ. The results show that when k = 3 nD and χ = 0.11. Shown in Fig.4.12 is the comparison between this research best fit and the simulated results using the diffusion solution. The results show that the estimated k and χ from this solution is significantly larger than those estimated using the diffusion solution. Such discrepancies can be the results of ignoring the poroelastic effects. Shown in Fig.4.13 are the plots of simulated results using the permeability and membrane efficiency determined in Chen et al. (2010) for different sample Young's modulus and Biot's modulus (with k = 0.3 nD and χ = 0.11). The results show that in order to closely recover the result from the diffusion solution, the sample has to be very stiff (E = 95 GPa, M = 85 GPa) so that the poroelastic effect can be ignored. Therefore, it is important to include the poroelastic effect in simulating the pore pressure responses in pressure transmission test, especially for tests performed on soft rocks.

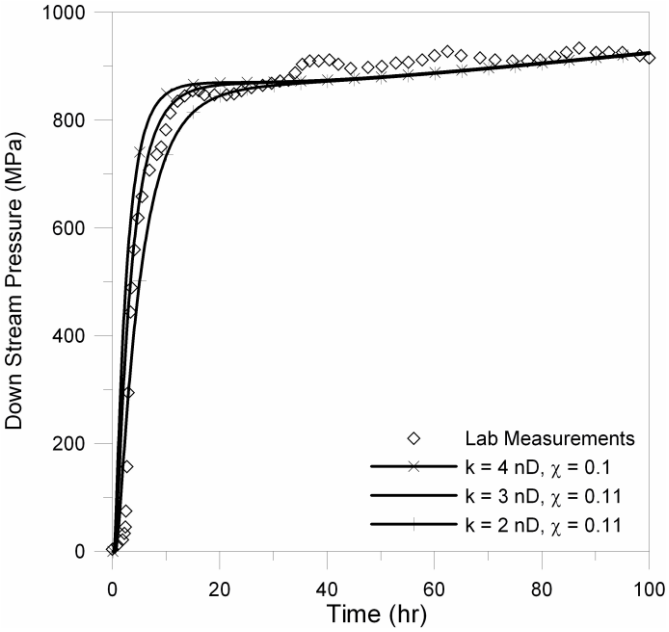


Fig.4.11-Comparison between lab measured down stream pore pressure and simulated results using different values of k and χ

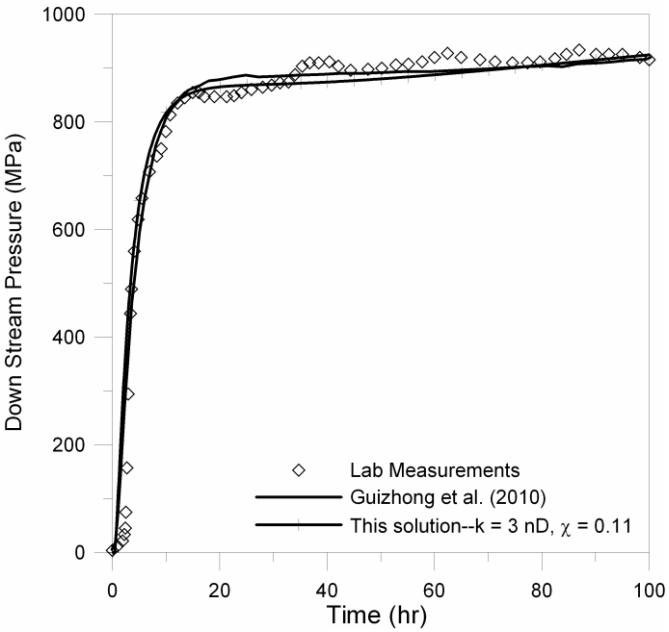


Fig.4.12- Comparison of lab measured down stream pore pressure, Chen et al. (2010) simulated results, and simulated results from this solution using different values of k = 0.3 nD and χ = 0.11

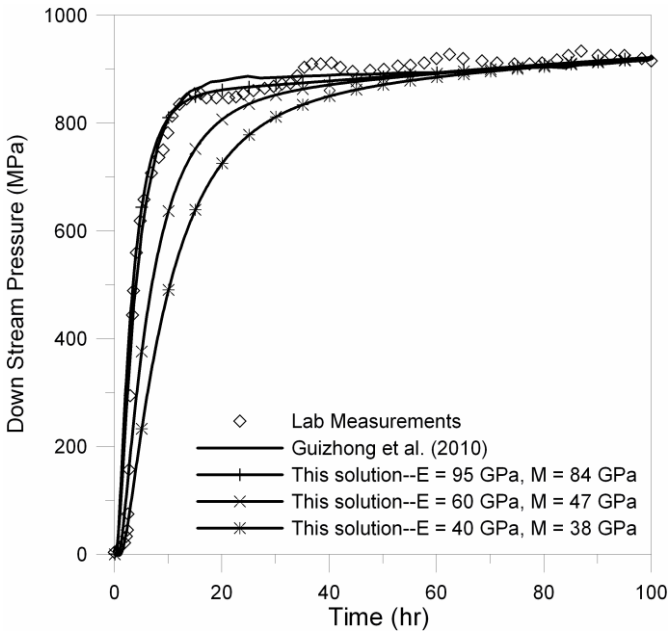


Fig.4.13- Comparison of lab measured down stream pore pressure, Chen et al. (2010) simulated results, and simulated results from this solution using different values for poroelastic properties (all with k = 0.3 nD and χ = 0.11)

4.6 Summary

In this chapter, the anisotropic porochemoelectroelastic for cylinder is given. Numerical examples illustrating the applications of the solutions for uniaxial testing with samples being exposed to testing fluid of different chemistry, and determination of shale diffusion parameters with pressure transmission test are included.

Regarding unixial testing of a cylindrical shale sample, the analyses show that shales with higher fixed charges content (more reactive clay, e.g. smectite) create a significant osmotic pressure at the interface of the sample and the testing fluid due to the Donnan effect. This fixed-charge-induced pressure when coupled with the pore pressure surge due to applied load and the activity-generated pore pressure can result in significant tensile effective stresses in the sample which may lead to tensile damages of the sample. These damages can complicate the interpretation for the effects of fluid chemistry on the rock matrix and it is recommended to gradually bring the salt concentration of the

testing fluid and the applied load to the desired value so that excessive stress and pore pressure buildup can be minimized.

In the context of laboratory characterization for shale diffusion parameters using pressure transmission test, the results show that ignoring the coupled electrochemical and poroelastic effects can lead to significant underestimation of the rock permeability and membrane efficiency. The problem can exacerbate in soft sedimentary rocks in which it is well known that the coupled hydro-mechanical effects of poroelasticity is more pronounced.

Chapter 5: The Wellbore Problem[2]

5.1 Introduction

With increasing shale drilling and fracturing activities for oil and gas production, the effects of coupled chemical-mechanical processes on the stability of wellbore drilling in shale formations have become a topic of extensive research. For example, the isotropic solution of a plane strain wellbore was derived by lumping the activity-generated osmotic pressure and pore pressure into a chemical potential term and ignoring the solute transport effect (*Sherwood & Bailey*, 1994). Later, the fully coupled anisotropic formulation for chemically active formations were presented and used to obtain the analytical solution for inclined boreholes subjected to in-situ state of stress in isotropic and transversely isotropic formations (*Ekbote & Abousleiman*, 2006). However, the electrical coupling effects were also neglected in this model. Recently, the porochemoelectroelastic analytical solution of inclined wellbore in isotropic formations was derived and presented by (*Nguyen & Abousleiman*, 2010).

In this chapter, the anisotropic porochemoelectroelastic solution for an inclined borehole drilled in transversely isotropic chemically active shale formation is presented. The solution finds a wide range of applications in the petroleum industry as illustrated through the examples of wellbore drilling and leak-off test in the Woodford Shale formation.

[2] This chapter have been published in Tran & Abousleiman, *J. App. Mech.* (2013)

5.2 The Inclined Wellbore Problem

5.2.1 Problem Descriptions

Consider an infinitely long wellbore drilled perpendicular to the isotropic plane of a transversely isotropic shale formation as shown in Fig.5.1. Also shown in Fig.5.1 is a Cartesian coordinate system *X*-*Y*-*Z* chosen with *X* and *Y* axes coinciding with S_H and S_h, respectively. The wellbore coordinate systems *x*-*y*-*z* and *r*-θ-*z* are also adopted to describe the stress state at far-field and around the wellbore. The coordinate system *x*-*y*-*z* is obtained from *X*-*Y*-*Z* by such rotation that *Z* becomes *z* while *y* remains in the horizontal plane (*Cui et al.*, 1997). Finally, the wellbore polar coordinate system *r*-θ-*z* is simply the complementary polar coordinate system of *x*-*y*-*z*.

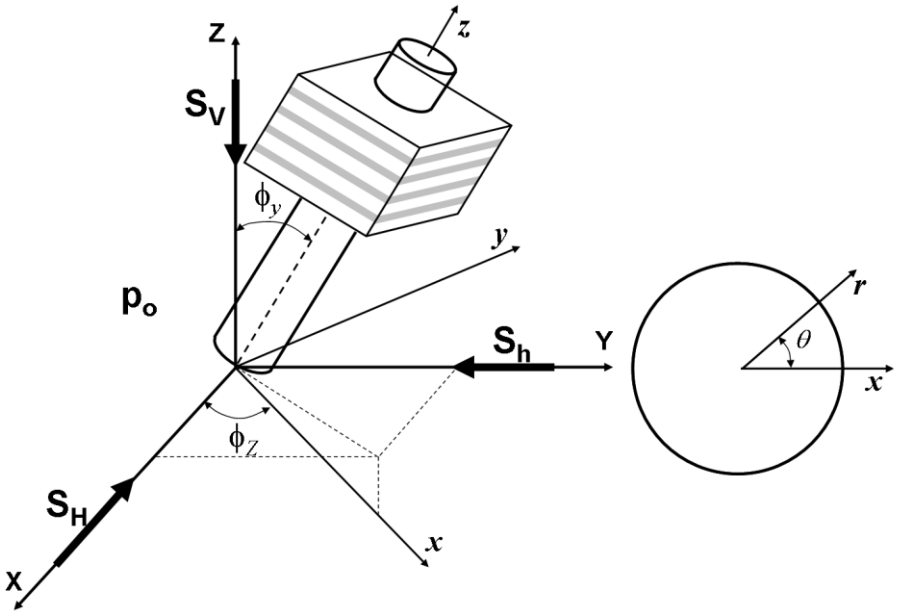


Fig.5.1-Geological and wellbore coordinates

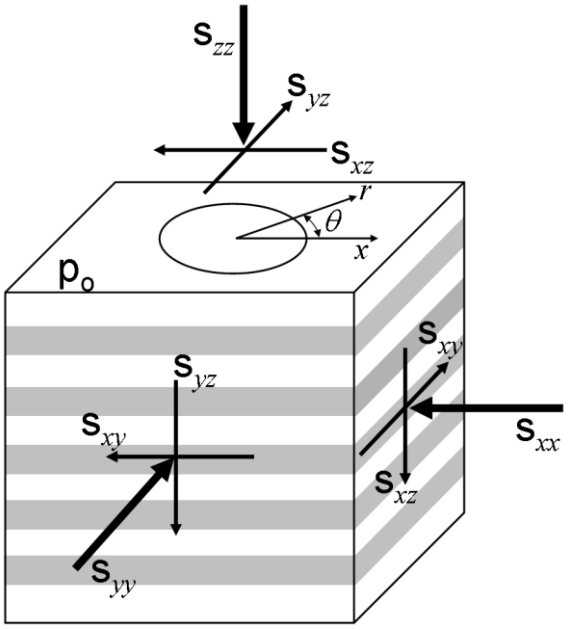


Fig.5.2-The far-field stress components expressed in wellbore coordinate

The in-situ stresses in the rock formation prior to borehole excavation can be expressed in terms of wellbore coordinate system, *x-y-z*, as shown in Fig.5.2. The transformed stress components obey the following relation

$$\begin{bmatrix} S_{xx} \\ S_{yy} \\ S_{zz} \\ S_{xy} \\ S_{xz} \\ S_{yz} \end{bmatrix} = \begin{bmatrix} \cos^2\phi_Z \cos^2\phi_y & \sin^2\phi_Z \cos^2\phi_y & \sin^2\phi_y \\ \sin^2\phi_Z & \cos^2\phi_Z & 0 \\ \cos^2\phi_Z \sin^2\phi_y & \sin^2\phi_Z \sin^2\phi_y & \cos^2\phi_y \\ -\cos\phi_Z \cos\phi_y \sin\phi_Z & \sin\phi_Z \cos\phi_y \cos\phi_Z & 0 \\ \cos^2\phi_Z \cos\phi_y \sin\phi_y & \sin^2\phi_Z \cos\phi_y \sin\phi_y & \sin\phi_y \cos\phi_y \\ -\cos\phi_Z \sin\phi_y \sin\phi_Z & \sin\phi_Z \sin\phi_y \cos\phi_Z & 0 \end{bmatrix} \begin{bmatrix} S_H \\ S_h \\ S_V \end{bmatrix} \tag{5.1}$$

In wellbore cylindrical coordinate *r-θ-z*, the far-field stress components are as follows:

$$S_{rr} = M_o + S_o \cos 2(\theta - \theta_o) \tag{5.2a}$$

$$S_{\theta\theta} = M_o - S_o \cos 2(\theta - \theta_o) \tag{5.2b}$$

$$S_{r\theta} = -S_o \sin 2(\theta - \theta_o) \tag{5.2c}$$

$$S_{rz} = S_{xz} \cos(\theta) + S_{yz} \sin(\theta) \tag{5.2d}$$

$$S_{\theta z} = -S_{xz} \sin(\theta) + S_{yz} \cos(\theta) \tag{5.2e}$$

with

$$M_o = \frac{S_{xx} + S_{yy}}{2} \tag{5.2f}$$

$$S_o = \sqrt{\left(\frac{S_{xx} - S_{yy}}{2}\right)^2 + S_{xy}^2} \tag{5.2g}$$

$$\theta_o = \frac{1}{2}\arctan\frac{2S_{xy}}{S_{xx} - S_{yy}} \tag{5.2h}$$

5.2.2 Boundary Conditions

The boundary conditions imposed at the wellbore wall ($r = R_w$) are as follows

$$\sigma_{rr} = \{M_o + S_o \cos[2(\theta - \theta_o)]\}H(-t) + p_{mud}(t)H(t) \tag{5.3a}$$

$$\sigma_{r\theta} = -S_o \cos[2(\theta - \theta_o)]H(-t) \tag{5.3b}$$

$$\sigma_{rz} = (S_{xz}\cos\theta + S_{yx}\sin\theta)H(-t) \tag{5.3c}$$

$$p = p_o H(-t) + [p_{mud}(t) + \Delta p_{mud/shale}(t)]H(t) \tag{5.3d}$$

$$p_a = \frac{RT}{V_f^o}\left\{n_a^o H(-t) + \left[n_s^{mud}(t) + \Delta n_a^{mud/shale}(t)\right]H(t)\right\} \tag{5.3e}$$

$$p_c = \frac{RT}{V_f^o}\left\{n_c^o H(-t) + \left[n_s^{mud}(t) + \Delta n_c^{mud/shale}(t)\right]H(t)\right\} \tag{5.3f}$$

where $H(t)$ is the Heaviside step function and

$$\Delta n_{mud/shale}^{a}(t) = n_a^{shale}\Big|_{r=Rw}(t) - n_s^{mud}(t) \tag{5.3g}$$

$$\Delta n_{mud/shale}^{c}(t) = n_c^{shale}\Big|_{r=Rw}(t) - n_s^{mud}(t) \tag{5.3h}$$

The boundary conditions as $r \longrightarrow \infty$ are

$$\sigma_{xx} = S_{xx} \tag{5.4a}$$

$$\sigma_{yy} = S_{yy} \tag{5.4b}$$

$$\sigma_{zz} = S_z z \tag{5.4c}$$

$$\sigma_{xy} = S_{xy} \tag{5.4d}$$

$$\sigma_{yz} = S_{yz} \tag{5.4e}$$

$$\sigma_{xz} = S_{xz} \tag{5.4f}$$

$$p = p_o \tag{5.4g}$$

$$p_a = \frac{RTn_a^o}{V_f^o} \tag{5.4h}$$

$$p_c = \frac{RTn_c^o}{V_f^o} \tag{5.4i}$$

This problem, in spite of the formation anisotropy, can still be decomposed into three sub-problems, namely, a poroelastic plane strain problem (*Problem I*), an elastic uniaxial problem (*Problem II*), and an elastic anti-plane shear problem (*Problem III*) (*Abousleiman & Cui*, 1998). Each of the problems can be solved separately and superimposed at the end to arrive at the total solutions.

5.3 Analytical Solutions

5.3.1 Solution for Poroelastic Plane Strain Problem

The solution for this problem can only be solved analytically in the Laplace transform domain (*Carter & Booker*, 1982). To facilitate Laplace transform technique, the solution is solved for the perturbed states so that all variables vanish identically at $r \rightarrow \infty$ and at $t = 0$. The perturbed boundary conditions at the wellbore wall for *Problem I* are

$$\sigma_{rr} = -M_o - S_o \cos\left[2(\theta - \theta_o)\right] + p_{mud}(t) \tag{5.5a}$$

$$\sigma_{r\theta} = S_o \cos\left[2(\theta - \theta_o)\right] \tag{5.5b}$$

$$p = -p_o + p_{mud}(t) + \Delta p_{mud/shale}(t) = \Delta p(t) \tag{5.5c}$$

$$p_a = \frac{RT}{V_f^o}\left[-n_a^o + n_s^{mud}(t) + \Delta n_a^{mud/shale}(t)\right] = \Delta p_a(t) \tag{5.5d}$$

$$p_c = \frac{RT}{V_f^o}\left[-n_c^o + n_s^{mud}(t) + \Delta n_c^{mud/shale}(t)\right] = \Delta p_c(t) \tag{5.5e}$$

These boundary conditions can further be decomposed into an axis-symmetric loading part (*Part 1*) as follows

$$\sigma_{rr} = -M_o + p_{mud}(t) \tag{5.6a}$$

$$\sigma_{r\theta} = 0 \tag{5.6b}$$

$$p = \Delta p(t) \tag{5.6c}$$

$$p_a = \Delta p_a(t) \tag{5.6d}$$

$$p_c = \Delta p_c(t) \tag{5.6e}$$

and a deviatoric loading part (*Part 2*)

$$\sigma_{rr} = -S_o \cos\left[2(\theta - \theta_o)\right] \tag{5.7a}$$

$$\sigma_{r\theta} = S_o \cos\left[2(\theta - \theta_o)\right] \tag{5.7b}$$

$$p = p_a = p_c = 0 \tag{5.7c}$$

For the borehole problems it is natural to employ the cylindrical coordinate system. The constitutive relations under plane strain condition ($\varepsilon_{zz} = 0$) is simplified to

$$\sigma_{rr} = C_{11}\varepsilon_{rr} + C_{12}\varepsilon_{\theta\theta} + \alpha_1 p \tag{5.8a}$$

$$\sigma_{\theta\theta} = C_{12}\varepsilon_{rr} + C_{11}\varepsilon_{\theta\theta} + \alpha_1 p \tag{5.8b}$$

$$\sigma_{r\theta} = 2C_{44}\varepsilon_{r\theta} = 2G_1\varepsilon_{r\theta} \tag{5.8c}$$

$$\xi = -\alpha_1\left(\varepsilon_{rr} + \varepsilon_{\theta\theta}\right) + \frac{1}{M}p = -\alpha_1\varepsilon_{kk} + \frac{1}{M}p \tag{5.8d}$$

$$\xi_a = n_a^o\left[-\alpha_1\varepsilon_{kk} + \frac{1}{M}p\right] + \phi^o n_a \tag{5.8e}$$

$$\xi_c = n_c^o\left[-\alpha_1\varepsilon_{kk} + \frac{1}{M}p\right] + \phi^o n_c \tag{5.8f}$$

where C_{ij} are the anisotropic elastic stiffness coefficients, α_i are the anisotropic Biot's pore pressure coefficients. The subscripts "1" and "2" denote properties in the isotropic plane (r-θ plane) and "3" when used denotes properties along the material axis of symmetry (z-direction).

In the polar coordinate system, the equilibrium equations as presented in Chapter 2 become

$$\frac{\partial\sigma_{rr}}{\partial r} + \frac{1}{r}\frac{\partial\sigma_{\theta r}}{\partial\theta} + \frac{\partial\sigma_{zr}}{\partial z} + \frac{\sigma_{rr} - \sigma_{\theta\theta}}{r} = 0 \tag{5.9a}$$

$$\frac{\partial\sigma_{r\theta}}{\partial r} + \frac{1}{r}\frac{\partial\sigma_{\theta\theta}}{\partial\theta} + \frac{\partial\sigma_{z\theta}}{\partial z} + \frac{\sigma_{r\theta} + \sigma_{\theta r}}{r} = 0 \tag{5.9b}$$

$$\frac{\partial\sigma_{rz}}{\partial r} + \frac{1}{r}\frac{\partial\sigma_{\theta z}}{\partial\theta} + \frac{\partial\sigma_{zz}}{\partial z} + \frac{\sigma_{rz}}{r} = 0 \tag{5.9c}$$

whereas the strain-displacement equations become

$$\varepsilon_{rr} = \frac{\partial u_r}{\partial r} \tag{5.10a}$$

$$\varepsilon_{\theta\theta} = \frac{1}{r}\frac{\partial u_\theta}{\partial\theta} + \frac{u_r}{r} \tag{5.10b}$$

$$\varepsilon_{zz} = \frac{\partial u_z}{\partial z} \tag{5.10c}$$

$$\varepsilon_{r\theta} = \frac{1}{2}\left(\frac{1}{r}\frac{\partial u_r}{\partial\theta} + \frac{\partial u_\theta}{\partial r} - \frac{u_\theta}{r}\right) \tag{5.10d}$$

$$\varepsilon_{rz} = \frac{1}{2}\left(\frac{\partial u_r}{\partial z} + \frac{\partial u_z}{\partial r}\right) \tag{5.10e}$$

$$\varepsilon_{\theta z} = \frac{1}{2}\left(\frac{\partial u_\theta}{\partial z} + \frac{1}{r}\frac{\partial u_z}{\partial\theta}\right) \tag{5.10f}$$

$$\omega_z = \frac{1}{2}\left(-\frac{1}{r}\frac{\partial u_r}{\partial \theta} + \frac{\partial u_\theta}{\partial r} + \frac{u_\theta}{r}\right) \tag{5.10g}$$

, and the conservation equations become

$$\frac{\partial \zeta}{\partial t} = -\vec{\nabla}.\vec{q} \tag{5.11a}$$

$$\frac{\partial \zeta_a}{\partial t} = -V_o^f \vec{\nabla}.\vec{J}^a = -V_o^f \vec{\nabla}.(\vec{J}^{a,d} + n_a \vec{q}/V_o^f) \tag{5.11b}$$

$$\frac{\partial \zeta_c}{\partial t} = -V_o^f \vec{\nabla}.\vec{J}^c = -V_o^f \vec{\nabla}.(\vec{J}^{c,d} + n_c \vec{q}/V_o^f) \tag{5.11c}$$

$$\frac{\partial \rho_e}{\partial t} = -\vec{\nabla}.\vec{I} \tag{5.11d}$$

with $\vec{\nabla} = \frac{\partial}{\partial r}\hat{r} + \frac{1}{r}\frac{\partial}{\partial \theta}\hat{\theta} + \frac{\partial}{\partial z}\hat{z}$ is the gradient vector in the cylindrical coordinate system.

Substituting the stress-strain relations and the transport equations into the mass and electrical charge balance equations while assuming electrostatic condition ($\partial \rho_e / \partial t = 0$), and ignoring the ion transport by advection terms gives (*Nguyen & Abousleiman*, 2010; *Tran & Abousleiman*, 2013)

$$\frac{\partial}{\partial t}\begin{bmatrix} -\alpha_1 & \frac{1}{M} & 0 & 0 \\ -n_a^o\alpha_1 & \frac{n_a^o}{M} & \frac{\phi^o V_f^o}{RT} & 0 \\ -n_a^o\alpha_1 & \frac{n_a^o}{M} & 0 & \frac{\phi^o V_f^o}{RT} \end{bmatrix}\begin{bmatrix} \varepsilon_{kk} \\ p \\ p_a \\ p_c \end{bmatrix} = [D]\nabla^2\begin{bmatrix} p \\ p_a \\ p_c \end{bmatrix} \tag{5.12a}$$

with

$$[D] = \begin{bmatrix} \kappa & -\chi\kappa & -\chi\kappa \\ n_a^o(1-\chi)\kappa & \frac{D_{eff}^a V_f^o}{RT} - n_a^o(1-\chi)\chi\kappa & -n_a^o(1-\chi)\chi\kappa \\ n_c^o(1-\chi)\kappa & -n_c^o(1-\chi)\chi\kappa & \frac{D_{eff}^c V_f^o}{RT} - n_c^o(1-\chi)\chi\kappa \end{bmatrix} \tag{5.12b}$$

and $\nabla^2 = \frac{\partial^2}{\partial r^2} + \frac{1}{r}\frac{\partial}{\partial r} + \frac{1}{r^2}\frac{\partial^2}{\partial \theta^2}$ is the Laplacian in polar coordinate.

Substituting the stress-strain relations into the equilibrium equations and taking into account the strain-displacement equations gives

$$C_{11}\frac{\partial \varepsilon_{kk}}{\partial r} + \alpha_1 \frac{\partial p}{\partial r} - \frac{2G_1}{r}\frac{\partial \omega_z}{\partial \theta} = 0 \tag{5.13a}$$

$$\frac{C_{11}}{r}\frac{\partial \varepsilon_{kk}}{\partial \theta} + \alpha_1 \frac{\partial p}{\partial \theta} + 2G_1 \frac{\partial \omega_z}{\partial r} = 0 \tag{5.13b}$$

The boundary conditions as shown in Eq.5.6-7 suggest the following form for the general solutions (*Carter & Booker*, 1982)

$$\{p, p_a, p_c, \zeta, \sigma_{rr}, \sigma_{\theta\theta}, \varepsilon_{rr}, \varepsilon_{\theta\theta}, \varepsilon_{kk}, u_r\} = \{P, P_a, P_c, Z, S_{rr}, S_{\theta\theta}, E_{rr}, E_{\theta\theta}, E, U_r\}\cos[n(\theta - \theta_o)] \tag{5.14}$$

$$\{\sigma_{r\theta}, \omega_z, u_\theta\} = \{S_{r\theta}, W, U_\theta\}\sin[n(\theta - \theta_o)] \tag{5.15}$$

with $n = 0$ for axis-symmetric loading and $n = 2$ for deviatoric loading. P, P_a, P_c, Z, S_{rr}, $S_{\theta\theta}$, $S_{r\theta}$, E_{rr}, $E_{\theta\theta}$, $E_{r\theta}$, W_z, E_{kk}, U_r, U_θ are functions of time and radial distance only. Incorporating Eq.5.14-15 into Eq.5.13 and seeking for bounded solutions gives

$$\widetilde{W} = -\frac{C_{11}}{2G_1} C_o r^{-n} \tag{5.16}$$

$$\widetilde{E} + \frac{\alpha_1}{C_{11}}\widetilde{P} = C_o r^{-n} \tag{5.17}$$

where C_o is a constant of integration to be determined from boundary conditions, the tilde sign denotes Laplace transform solution, and s is the Laplace variable. Substituting Eq.5.17 into the Laplace transform of Eq.5.12 and taking into account Eq.5.14 yields

$$\underbrace{s\begin{bmatrix} \frac{\alpha_1^2}{C_{11}}+\frac{1}{M} & 0 & 0 \\ n_a^o\left(\frac{\alpha_1^2}{C_{11}}+\frac{1}{M}\right) & \frac{\phi^o V_f^o}{RT} & 0 \\ n_c^o\left(\frac{\alpha_1^2}{C_{11}}+\frac{1}{M}\right) & 0 & \frac{\phi^o V_f^o}{RT} \end{bmatrix}}_{[Y]}\begin{bmatrix} \widetilde{P} \\ \widetilde{P}_a \\ \widetilde{P}_c \end{bmatrix} = [D]\nabla_n^2\begin{bmatrix} \widetilde{P} \\ \widetilde{P}_a \\ \widetilde{P}_c \end{bmatrix} + \alpha_1 s C_o r^{-n}\begin{bmatrix} 1 \\ n_a^o \\ n_c^o \end{bmatrix} \tag{5.18}$$

with $\nabla_n^2 = \frac{d^2}{dr^2}+\frac{1}{r}\frac{d}{dr}-\frac{n^2}{r^2}$.

Solving Eq.5.18 for $\widetilde{P}$, $\widetilde{P}_a$, $\widetilde{P}_c$ using matrix diagonalization technique (*Farlow*, 1993) gives

$$\widetilde{P} = f_1 C_o r^{-n} + \sum_{i=1}^{3} m_{1i} C_i K_n(\xi_i r) \tag{5.19}$$

$$\widetilde{P}_a = f_2 C_o r^{-n} + \sum_{i=1}^{3} m_{2i} C_i K_n(\xi_i r) \tag{5.20}$$

$$\widetilde{P}_c = f_3 C_o r^{-n} + \sum_{i=1}^{3} m_{3i} C_i K_n(\xi_i r) \tag{5.21}$$

with C_i are constants of integration to be determined from the boundary conditions, $K_n(\xi_i r)$ is the modified Bessel function of the second kind of order n, $\xi_i = \sqrt{s/\lambda_i}$, in which λ_i are the eigenvalues of the matrix $[Z] = [Y]^{-1}[D]$ with $\{m_{1i}, m_{2i}, m_{3i}\}$ as its corresponding eigenvectors, and $f_i = \alpha_1 [Y]^{-1}\begin{bmatrix} 1 & n_a^o & n_c^o \end{bmatrix}^T$.

Substituting Eq.5.19 into the constitutive equations and the strain-displacement equations, the expressions for stresses in the Laplace transform domain are obtained as follows

$$\widetilde{S}_{rr} = 2G_1\left[\frac{nC_{11}}{4G_1}+\frac{2-n}{4}\left(1-\frac{\alpha_1 f_1}{C_{11}}\right)+\frac{C_{12}}{2G_1}\left(1-\frac{\alpha_1 f_1}{C_{11}}\right)+\frac{\alpha_1 f_1}{2G_1}\right]C_o r^{-n} - 2G_1(1+n)C_4 r^{-n-2}$$
$$-2(n^2-n)\frac{\alpha_1 G_1}{C_{11}}\sum_{i=1}^{3}\frac{m_{1i}C_i K_n(\xi_i r)}{\xi_i^2 r^2} - 2\frac{\alpha_1 G_1}{C_{11}}\sum_{i=1}^{3}\frac{m_{1i}C_i K_{n+1}(\xi_i r)}{\xi_i r} \tag{5.22}$$

$$\widetilde{S}_{\theta\theta} = 2G_1\left[-\frac{nC_{11}}{4G_1}+\frac{2+n}{4}\left(1-\frac{\alpha_1 f_1}{C_{11}}\right)+\frac{C_{12}}{2G_1}\left(1-\frac{\alpha_1 f_1}{C_{11}}\right)+\frac{\alpha_1 f_1}{2G_1}\right]C_o r^{-n} + 2G_1(1+n)C_4 r^{-n-2}$$
$$+2(n^2+n)\frac{\alpha_1 G_1}{C_{11}}\sum_{i=1}^{3}\frac{m_{1i}C_i K_n(\xi_i r)}{\xi_i^2 r^2} + 2\frac{\alpha_1 G_1}{C_{11}}\sum_{i=1}^{3}\frac{m_{1i}C_i K_{n-1}(\xi_i r)}{\xi_i r} + 2\frac{\alpha_1 G_1}{C_{11}}\sum_{i=1}^{3}m_{1i}C_i K_n(\xi_i r) \tag{5.23}$$

$$\widetilde{S}_{r\theta} = G_1\left\{\left[-\frac{nC_{11}}{2G_1(1-n)}-\frac{2n}{4}\left(1-\frac{\alpha_1 f_1}{C_{11}}\right)\right]C_o r^{-n} - 2(1+n)C_4 r^{-n-2} - 2n\frac{\alpha_1}{C_{11}}\sum_{i=1}^{3}\frac{m_{1i}C_i K_{n-1}(\xi_i r)}{\xi_i r}\right.$$
$$\left.-2(n^2+n)\frac{\alpha_1}{C_{11}}\sum_{i=1}^{3}\frac{m_{1i}C_i K_n(\xi_i r)}{\xi_i^2 r^2}\right\} \tag{5.24}$$

where C_4 is the constant of integration to be determined from the boundary conditions. For brevity, the complete solutions for each loading part with the corresponding constant of integrations are presented in the Appendix B. From there, the solution in time domain can be obtained using numerical inverse Laplace transform algorithms such as the Stehfest's algorithm (*Stehfest*, 1970).

5.3.2 Solution for Uniaxial Stress Problem

The solution for this problem is purely elastic (*Cui et al.*, 1997; *Abousleiman & Cui*, 1998)

$$\sigma_{zz} = S_{zz} - 2\nu_3 M_o - (\alpha_3 - 2\nu_3\alpha_1)p_o \tag{5.25}$$

5.3.3 Solution for Anti-plane Shear Problem

The solution for this problem is also purely elastic (*Cui et al.*, 1997; *Abousleiman & Cui*, 1998)

$$\sigma_{rz} = \left(S_{xz}\cos\theta + S_{yz}\sin\theta\right)\left(1-\frac{R_w^2}{r^2}\right) \tag{5.26}$$

$$\sigma_{\theta z} = \left(S_{yz}\cos\theta - S_{xz}\sin\theta\right)\left(1+\frac{R_w^2}{r^2}\right) \tag{5.27}$$

5.3.4 Complete Solution for Inclined Wellbore Problem

The final (total) solution are achieved by superimpose the solutions of individual problems

$$p^{total} = p_o + p^{(1)} + p^{(2)} \tag{5.28}$$

$$p_a^{total} = \frac{RT}{V_f^o}n_a^o + p_a^{(1)} + p_a^{(2)} \tag{5.29}$$

$$p_c^{total} = \frac{RT}{V_f^o}n_c^o + p_c^{(1)} + p_c^{(2)} \tag{5.30}$$

$$\sigma_{rr}^{total} = M_o + S_o\cos\left[2(\theta-\theta_o)\right] + \sigma_{rr}^{(1)} + \sigma_{rr}^{(2)} \tag{5.31}$$

$$\sigma_{\theta\theta}^{total} = M_o - S_o\cos\left[2(\theta-\theta_o)\right] + \sigma_{\theta\theta}^{(1)} + \sigma_{\theta\theta}^{(2)} \tag{5.32}$$

$$\sigma_{r\theta}^{total} = -S_o\cos\left[2(\theta-\theta_o)\right] + \sigma_{r\theta}^{(2)} \tag{5.33}$$

$$\sigma_{zz}^{total} = S_{zz} - 2\nu_3 M_o + \nu_3(\sigma_{rr}+\sigma_{\theta\theta}) + (\alpha_3 - 2\nu_3\alpha_1)(p-p_o) \tag{5.34}$$

$$\sigma_{\theta z}^{total} = \left(S_{yz}\cos\theta - S_{xz}\sin\theta\right)\left(1+\frac{R_w^2}{r^2}\right) \tag{5.35}$$

$$\sigma_{rz}^{total} = \left(S_{xz}\cos\theta + S_{yz}\sin\theta\right)\left(1-\frac{R_w^2}{r^2}\right) \tag{5.36}$$

where the superscripts "(1)" and "(2)" denote the solution of *Part 1* and *Part 2* respectively.

5.4 Solution Validations for Special Cases

First, the solution is validated against the special case of a transversely isotropic poroelastic formation using the numerical example presented in (*Abousleiman & Cui*, 1998). Shown in Fig.5.3 and Fig.5.4 are the effective tangential stress and effective axial stress with varying ratio of r/R_w along $\theta = 90^o$ when assuming that the formation CEC is zero and that the drilling mud activity is equal to the native formation activity. Other formation and fluid properties, in-situ stresses, and wellbore geometry are the same as in (*Abousleiman & Cui*, 1998). It can be observed that the solution does reduce to that of Abousleiman & Cui (1998) for this special case.

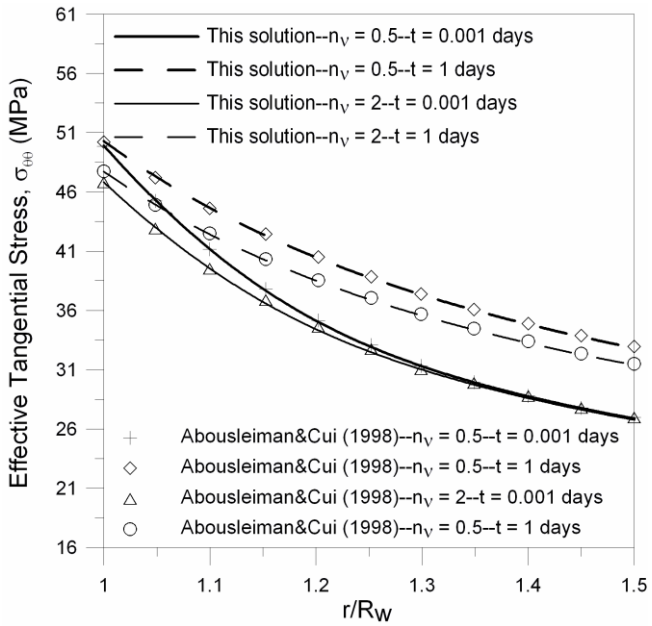


Fig.5.3-Effective tangential stress along $\theta = 90^o$, identical to the results in Abousleiman & Cui (1998)

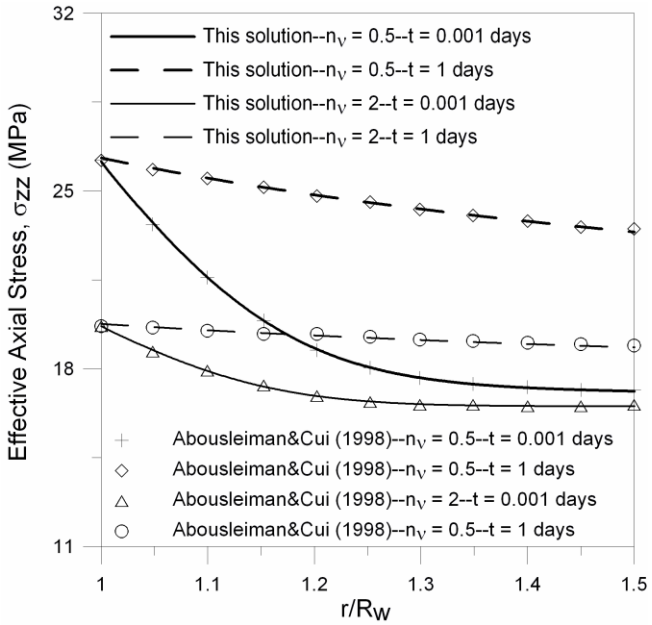


Fig.5.4-Effective axial stress along $\theta = 90^{o}$, identical to the results in Abousleiman & Cui (1998)

On the other hand, Fig.5.5 and Fig.5.6 are the effective radial and tangential stress around a vertical borehole in isotropic formation using the formation properties and in-situ conditions as in the numerical examples of (*Nguyen & Abousleiman*, 2010). The following formula $D_{eff}^{a,c} = (1-\chi)\phi^{\tau} D^{a,c}$ is used to calculate the effective ion diffusion coefficients. The rock tortuosity, τ, is assumed to be 2 which result in D_{eff}^{a} and D_{eff}^{c} of 9.6×10^{-12} (m^2/s) and 1.47×10^{-11} (m^2/s) as reported in Nguyen & Abousleiman (2010). It can be observed that these results do not reduce to those in (*Nguyen & Abousleiman*, 2010). It is possible that the previous study has applied the formula $D_{eff}^{a,c} = \tau\phi D^{a,c}$ in Shackleford & Daniel (1991) for estimating the effective ion diffusion coefficients which result in D_{eff}^{a} and D_{eff}^{c} of 2.53×10^{-10} (m^2/s) and 3.86×10^{-10} (m^2/s). In this case, the present solution does reduce to the results of Nguyen & Abousleiman (2010) for the special case of isotropic formation as shown in Fig.5.7 and Fig.5.8.

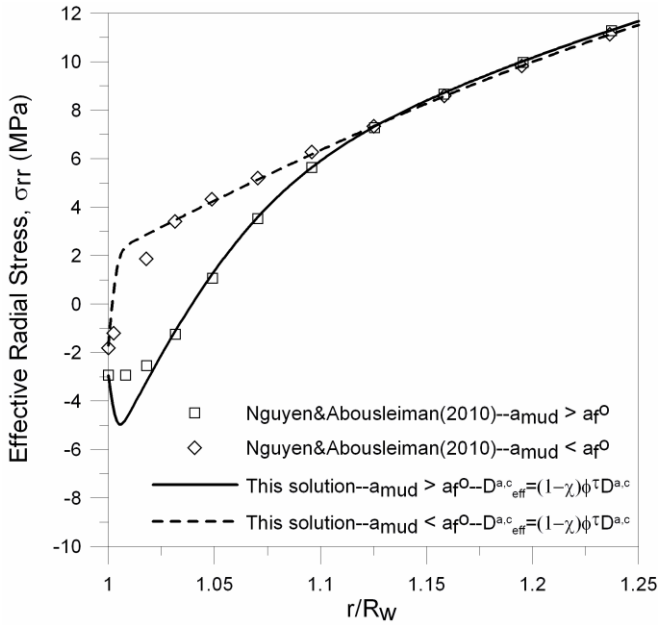


Fig.5.5-Effective radial stress when using D^{a}_{eff} = 9.6×10^{-12} (m^2/s) and D^{c}_{eff} = 1.47×10^{-11} (m^2/s), the results does not reduce to that of Nguyen & Abousleiman (2010)

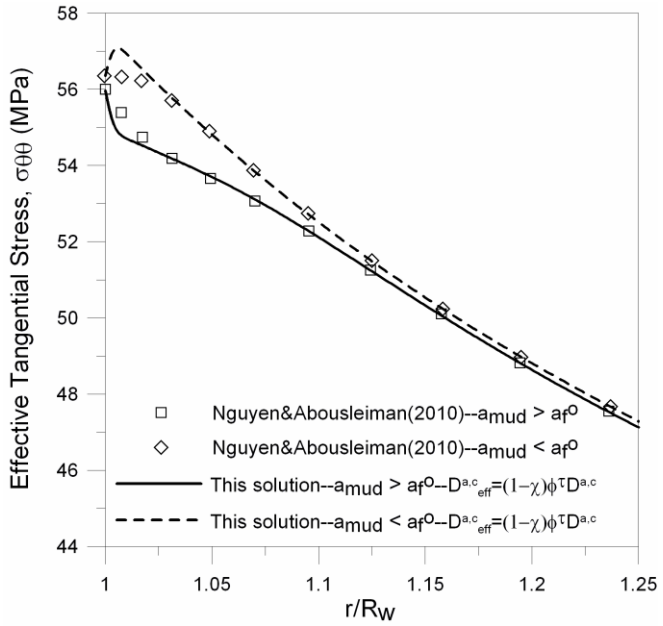


Fig.5.6-Effective tangential stress when using D^{a}_{eff} = 9.6×10^{-12} (m^2/s) and D^{c}_{eff} = 1.47×10^{-11} (m^2/s), the results does not reduce to that of Nguyen & Abousleiman (2010)

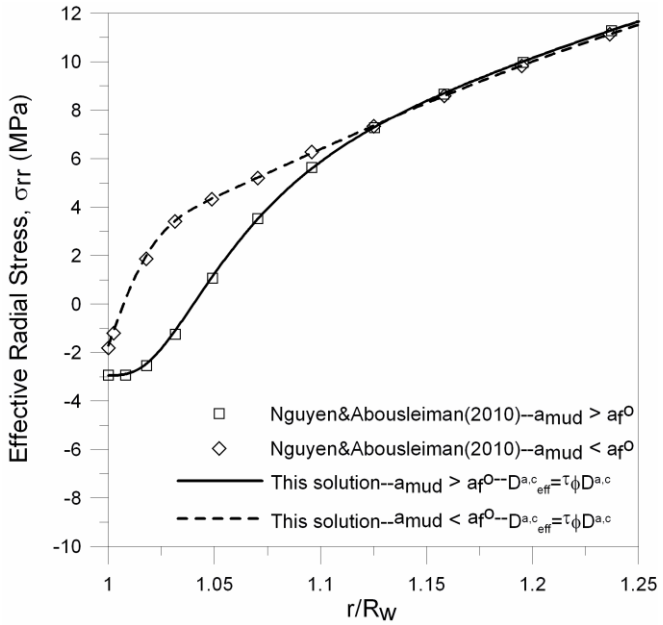


Fig.5.7-Effective radial stress, identical to the results in Nguyen & Abousleiman (2010) when using D^{a}_{eff} = 2.53×10^{-10} (m^2/s) and D^{c}_{eff} = 3.86×10^{-10} (m^2/s)

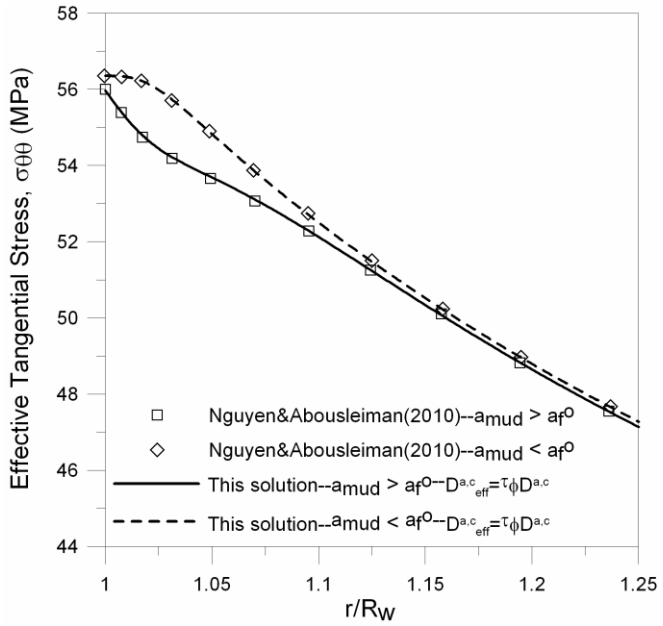


Fig.5.8-Effective tangential stress, identical to the results in Nguyen & Abousleiman (2010) when using D^{a}_{eff} = 2.53×10^{-10} (m^2/s) and D^{c}_{eff} = 3.86×10^{-10} (m^2/s)

5.5 Examples of Applications

5.5.1 Drilling in Shale

In this section, a vertical wellbore with radius of 0.1 m is assumed to be drilled in a shale formation at a depth of 2000 m and subject to the following in-situ conditions: S_V = 50 MPa, S_H = 44 MPa, S_h = 40 MPa, p_o = 19.6 MPa, $T = 90^o$ C. The drilling fluid is NaCl solution with activity of 0.9 and density of 1.07 g/cc. The shale formation rock properties are assumed to be that of the organic rich Woodford shale having native pore fluid activity a_o = 0.87 and geomechanical properties similar to those given in Table 3.2. Shown in Fig.5.9 is the pore pressure profile along the direction of the maximum horizontal stress ($\theta = 0^o$) at 15 minutes after drilling. The plot for the transversely isotropic poroelastic case (CEC = 0, $a_{\text{mud}} = a_o$) and the isotropic prochemoelectroelastic case with $E_1 = E_3$ = 4.2 GPa and $\nu_1 = \nu_3$ = 0.3 (this data set simulates an oil field scenario where sonic run in a vertical wellbore can only obtain mechanical properties along the wellbore-axis) are also included for comparison. The pore pressure jump at the wellbore wall when comparing the porochemoelectroelastic models with the anisotropic poroelastic model is the result of the Donnan equilibrium effect as discussed in previous sections. The pore pressure peak near the wellbore wall ($r/R_w \approx 1.03$) is a consequence of the chemical osmotic effects generated by the high mud salinity. On the other hand, the dip of pore pressure to a value below the virgin pore pressure (19.6 MPa) at $r/R_w \approx 1.35$ as shown in all three models is a result of the volumetric expansion of the formation on the side of the maximum horizontal stress. As time elapses, the pore pressure peak inside the formation decreases as shown in Fig.5.10. However, the pore pressure jump at the wellbore wall due to the Donnan equilibrium effect remains.

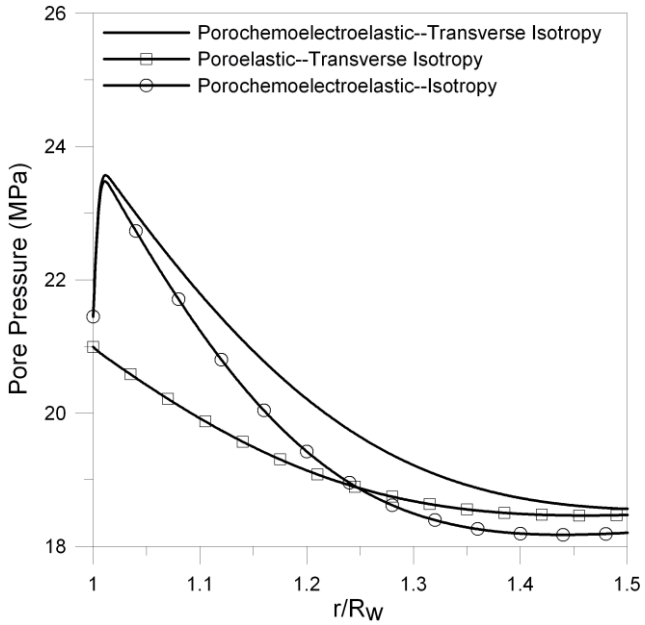


Fig.5.9-Pore pressure along the direction of S_H at t = 15 minutes

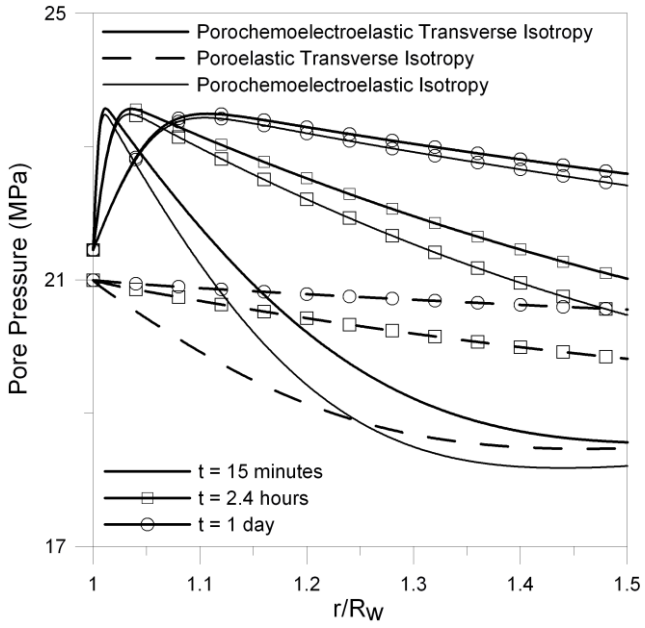


Fig.5.10-Pore pressure along the direction of S_H at various times

Shown in Fig.5.11 and Fig.5.12 are, respectively, the effective radial stress and the effective tangential stress in the direction of the maximum horizontal stress at 15 minutes after excavation. As seen in Fig.5.11, the pore pressure peak inside the formation as previously discussed results in a region of tensile effective radial stress near the wellbore wall which causes spalling failure of the formation in this region.

Similarly, a less compressive region close to the borehole wall is observed for the effective tangential stress as shown in Fig.5.12. For this particular analysis, it seems that the effects of formation anisotropy on pore pressure and effective radial stress distributions become more significant at places away from the wellbore wall.

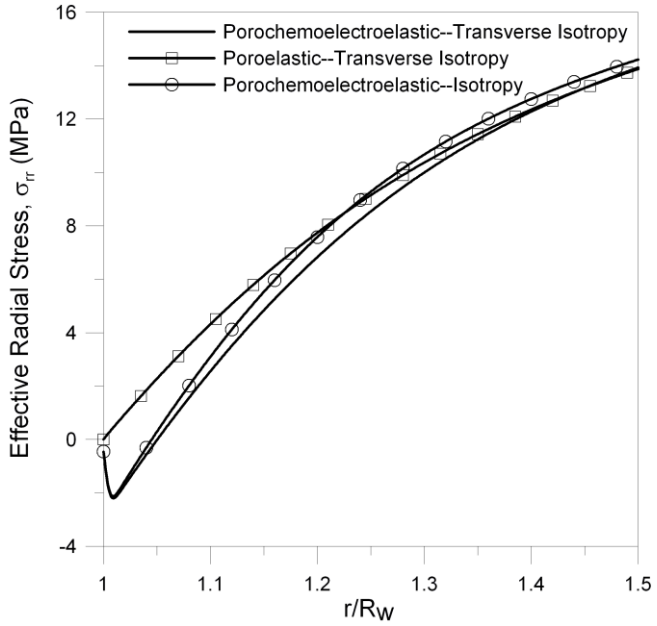


Fig.5.11-Effective radial stress along the direction of S_H at t = 15 minutes

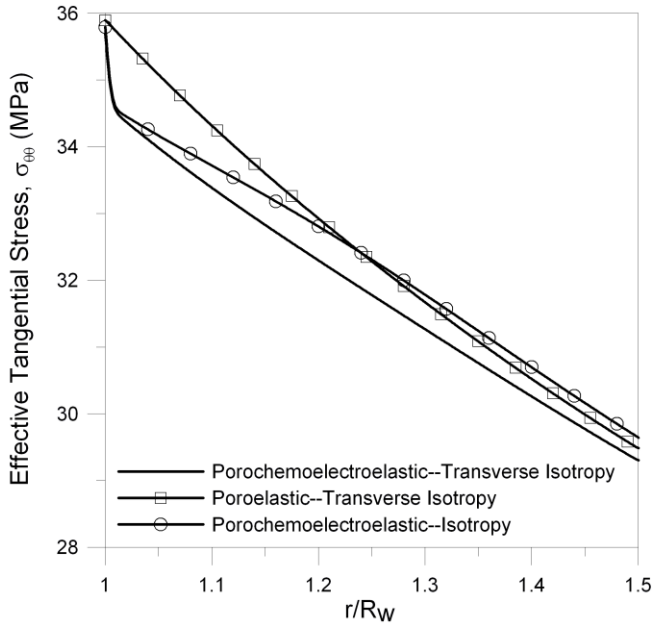


Fig.5.12-Effective tangential stress along the direction of S_H at t = 15 minutes

The effects of formation CEC on the effective radial stress distribution is shown in Fig.5.13. It can be observed that the higher the CEC values, the larger the extent of the near-wellbore tensile region. Hence, clay rich intervals are more susceptible to spalling failure than quartz rich intervals.

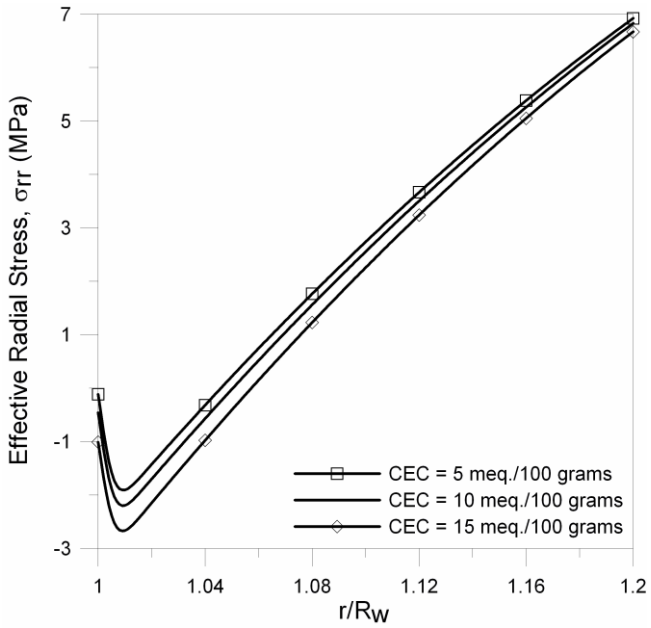


Fig.5.13-Effective radial stress along the direction of S_H at t = 15 minutes and CEC = 5, 10, 15 meq./100 grams

As shown in Fig.5.14 and Fig.5.15, the effective radial stress distribution near the wellbore wall (r/R_w < 1.05) is not sensitive to the variation of the Poisson's ratio and Young's modulus in the isotropic plane for this data set. This is in accordance with the observation in Abousleiman & Cui (1998) that the effects of anisotropy on radial stress only become more significant at places far away from the borehole wall as time progresses. On the other hand, the near wellbore distribution of the effective tangential stress is greatly affected by the formation anisotropy as shown in Fig.5.16 and Fig.5.17. Therefore, it is expected that the material anisotropy influences the wellbore fracturing mudweight significantly, while the corresponding elastic solution predicts no anisotropy effects on the fracturing at all. The results in this section clearly show that ignoring

either the porochemoelectroelastic effects or the formation transversely isotropic characteristic leads to inaccurate predictions of near wellbore effective stresses and pore pressure distribution.

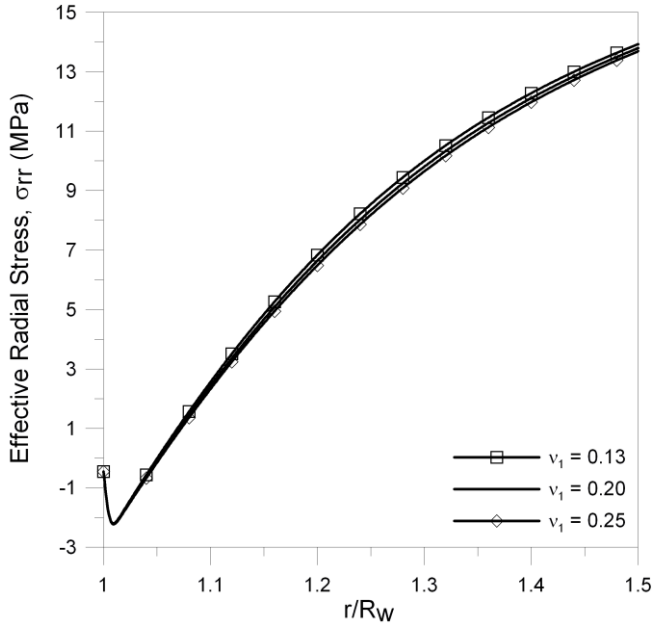


Fig.5.14-Effective radial stress along the direction of S_H at t = 15 minutes with ν_1 = 0.13, 0.2, 0.25 and ν_3 = 0.3

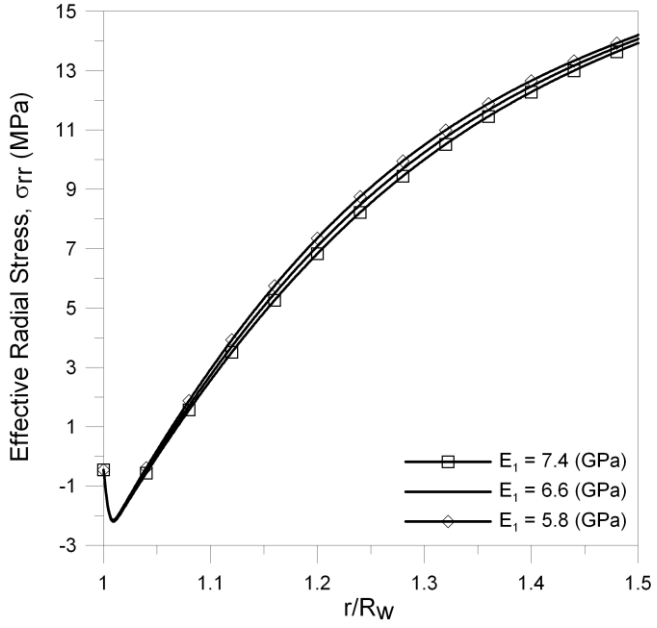


Fig.5.15-Effective radial stress along the direction of S_H at t = 15 minutes with E_1 = 7.4, 6.6, 5.8 (GPa) and E_3 = 4.2 (GPa)

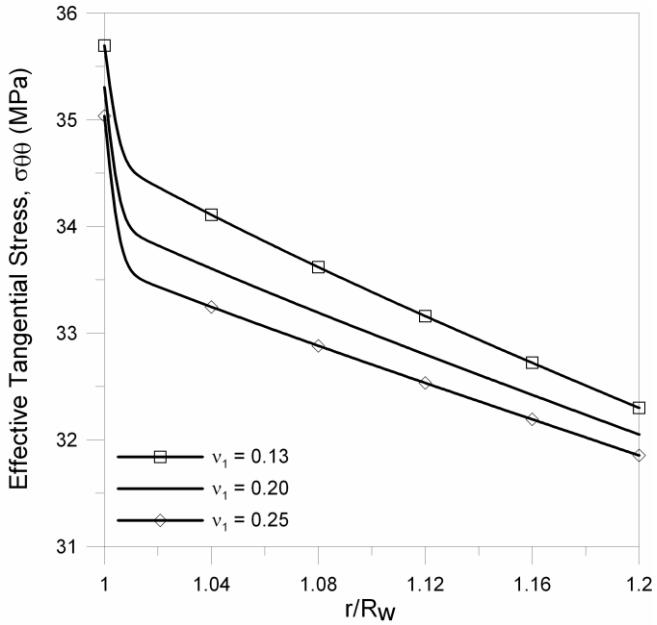


Fig.5.16-Effective tangential stress along the direction of S_H at t = 15 minutes with ν_1 = 0.13, 0.2, 0.25 and ν_3 = 0.3

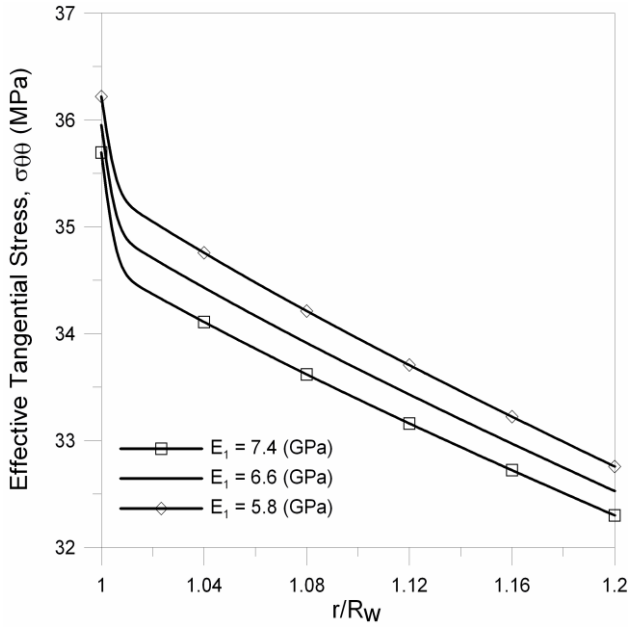


Fig.5. 17-Effective tangential stress along the direction of S_H at t = 15 minutes with E_1 = 7.4, 6.6, 5.8 (GPa) and E_3 = 4.2 (GPa)

5.5.2 Leak-off Test

In this section, the effects of borehole fluid pressure history on the pore pressure and stresses distribution around the wellbore is shown to demonstrate the versatility of the solutions. Of particular interest is the stress and pore pressure distribution during a leak-

off test. The leak-off test is usually performed to determine the strength or fracture pressure of the open formation and is usually conducted soon after drilling on the open formation section just below the new casing shoe. Shown in Fig.5.18 is a typical mud pressure and salinity history which mimics the down-hole conditions from the time of drilling to leak-off test. Practically, during leak-off tests, it is the pumping rate of the fracturing fluid instead of the down-hole pressure is controlled (known) variable. However, assuming that the fluid leak-off rate into the formation is negligible due to the intrinsically low permeability of the shale formations, a constant pumping rate will translate itself into a linear increase in down-hole pressure as shown in Fig.5.18.

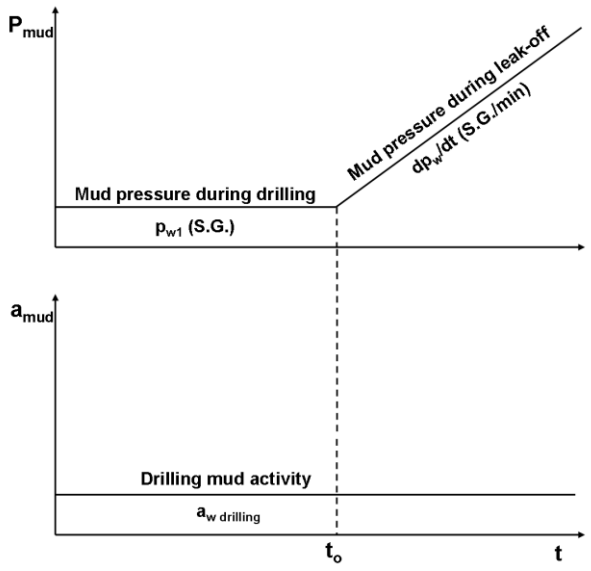


Fig.5.18-Typical mud pressure and mud salinity history during drilling and leak-off test

Because numerical Laplace inversion algorithms cannot be used to invert piecewise functions, analysis for mud pressure history as shown in Fig.5.18 require convoluting the solution of a wellbore creation problem (constant mud pressure) with the solution from a perturbed linear increase of wellbore pressure. The "perturbed" means changes

with respect to the down-hole condition during drilling. The solution for the wellbore creation problem has been addressed previously. The perturbed linear increase wellbore pressure problem has non-trivial perturbed boundary conditions at the wellbore wall ($r = R_w$) as shown in Eq.5.37, and the general solution is that of the axis-symmetric loading case (*Part* 1).

$$\sigma_{rr} = \left[\frac{dp}{dt} t - p_{w1} \right] H(t_o) \tag{5.37a}$$

$$p = \left[\frac{dp}{dt} t - p_{w1} \right] H(t_o) \tag{5.37a}$$

$$p_a = 0 \tag{5.37c}$$

$$p_c = 0 \tag{5.37d}$$

In this numerical example, the leak-off test is assumed to start at 30 minutes after drilling (t_o = 30 minutes). The down-hole pressure is assumed to increase linearly at a rate of 0.03 S.G./min. The formation properties and other down-hole conditions during drilling are assumed to be the same with the previous example. Fig.5.19-21 show the evolution of the pore pressure, the effective radial stress, and the effective tangential stress at 15, 30 minutes after drilling, and 10, 20 minutes after the start of leak-off test (or 40 and 50 minutes after drilling). As expected, the near-wellbore tensile zone of radial stress becomes smaller during leak-off test due to increasing compression from the ramping wellbore pressure as shown in Fig.5.20. On the other hand, the tangential stress at the wellbore wall becomes less and less compressive as time elapses as depicted in Fig.5.21.

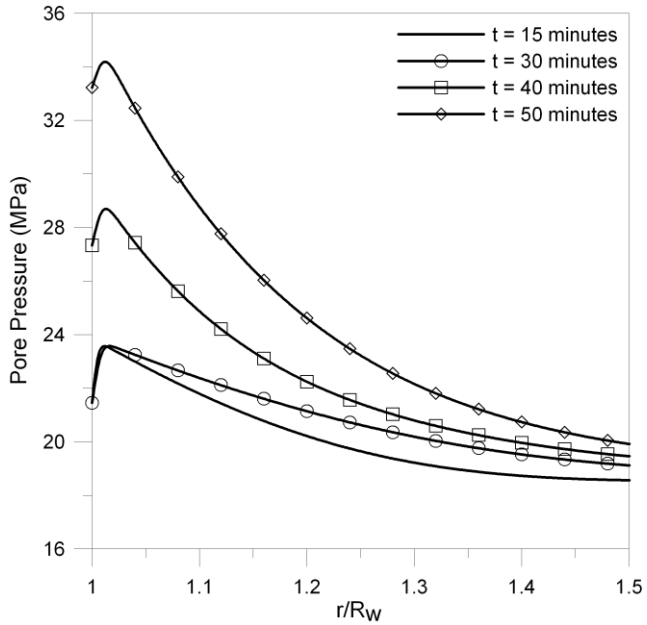


Fig.5.19-Pore pressure distribution ($\theta = 0^o$) at various times

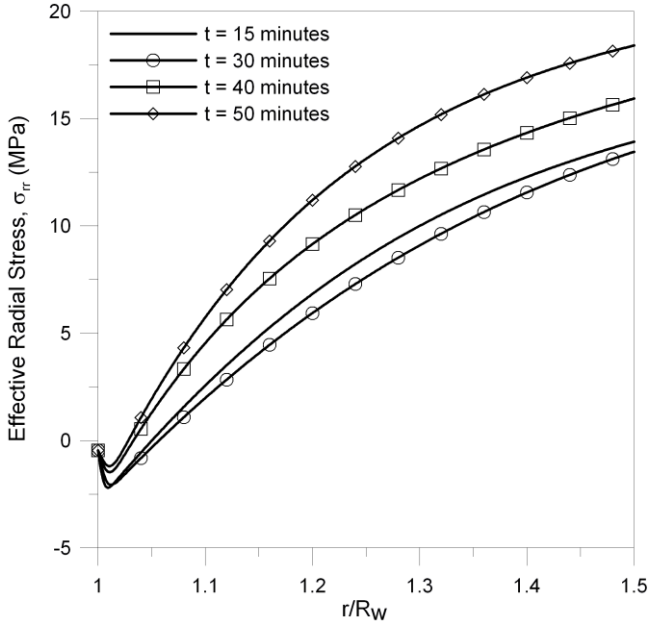


Fig.5.20-Effective radial stress distribution ($\theta = 0^o$) at various times

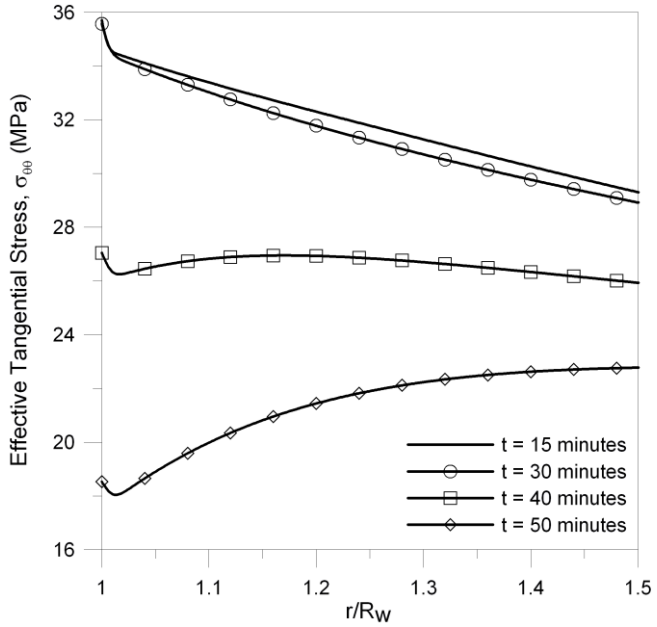


Fig.5.21-Effective tangential stress distribution ($\theta = 0^o$) at various time

5.6 Summary

In this chapter, the analytical solution for an inclined wellbore drilled in transversely isotropic chemically active and charged saturated shale formation is derived and presented. The solution finds a wide range of applications in the petroleum industry as illustrated through the examples of wellbore drilling and leak-off test in the heavily gas produced Woodford Shale formation.

From the present solutions, it is observed that the pore pressure diffusion is affected not only by the hydraulic Darcy's permeability, Fick's solute diffusion coefficient, and the membrane efficiency, but also by the electrokinetic contribution that manifests itself as a boundary effect at the borehole wall. The analyses show clearly that the effective tangential stress and the axial stress are greatly affected by the formation anisotropic mechanical parameters. The numerical examples also show that the presence of the negative fixed charges on clays surfaces creates a pore pressure jump at the wellbore wall due to the Donnan equilibrium effect. The problem exacerbates when drilling mud

with activity higher than the pore fluid native activity is used. These combined effects can result in a region of tensile effective radial stress and less compressive tangential stress near the wellbore wall which may lead to tensile failure of the formation. Since wellbore stability analyses are usually performed based on effective stresses, ignoring either the porochemoelectroelastic behavior or the anisotropic characteristic of the shale formation will mislead the predictions and assessment of potential problems in applied field engineering operations.

Chapter 6: Conclusions

In this work, the formulation for anisotropic porochemoelectroelasticity is presented. Discussions on the electrokinetic equilibrium conditions in the shale prior to and after being exposed to an external fluid are also included. Then, the analytical solutions for rectangular strip sample, cylindrical sample, and inclined wellbore under various loading and in-situ conditions while being exposed to aqueous solutions are derived. For each solution, numerical examples are given to illustrate the applications of the newly-derived solution for laboratory characterization and field analyses.

The results show that ignoring either the porochemoelectroelastic behavior or the well known anisotropic characteristic of the shale formation will mislead the predictions and assessment of potential problems in laboratory testing and field operations. In particular:

For laboratory characterization of shale, the analyses show that presence of negative fixed charges on the clay minerals create an osmotic pressure at the interface of the shale sample and the testing fluid with magnitude proportional to the CEC of the sample according to the Donnan equilibrium condition. The magnitude of the Donnan-induced pore pressure is rather small when compared to the load-generated pore pressure or activity-generated pore pressure. However, the Donnan-induced pore pressure when coupled with the pore pressure surge due to the applied load in addition to the use of a high activity (i.e. low salinity) testing fluid can result in significant tensile effective stresses in the sample which may lead to tensile damages in weak shale samples. The results, thus, explain why some shales disintegrate when brought into contact with

certain aqueous solutions while others do not. In addition, the complex pore pressure, stresses responses and distributions, and induced tensile damages can complicate the interpretation of experimental results for the effects of fluid chemistry on the rock matrix. It is, therefore, recommended to gradually adjust the testing fluid salt concentration or applied load to the desired value so that excessive induced stresses and pore pressure buildup become minimal.

Similarly, for application in shale hydraulic fracturing, the Donnan equilibrium effects and the use of a high activity (i.e. low salt concentration) water-based fracturing fluid can induce a tensile damage zone near the fracture surface. As the result, the formation becomes weaker and can deform more easily producing a wider fracture width and a shorter fracture length. In addition, the damaged and weakened formation can exacerbate the problem of proppant embedment leading to fracture closure and, thus, further reducing the fracture length and productivity. Thus, the results explain why higher clay content intervals are often observed to be more "ductile" compared to lower clay content intervals. Practically, the use of fracturing fluid having similar activity with the shale formation native pore fluid can help to prevent the tensile damages and work for the advantage of the fracturing process.

Analysis for shale electrokinetic effects on pore pressure buildup during diagenesis suggests that, in addition to the intrinsically low permeability of shale, the semi-permeable membrane behavior of the clay matrix can effectively hinder the overall pore fluid diffusion process. As a result, the pore pressure buildup inside a shale formation can be much higher than in a clean sand formation under the same consolidation rate.

Hence, taking into account shale electrokinetic effects in basin modeling may give better predictions of overpressure issues in shale.

In the context of laboratory characterization for shale diffusion parameters using the pressure transmission test, the results show that ignoring the coupled electrochemical and poroelastic effects can lead to significant underestimation of the rock permeability and membrane efficiency. The problem exacerbates in soft sedimentary rocks in which the coupled hydro-mechanical effects of poroelasticity is more pronounced.

Finally, analyses for wellbore drilling in shale clearly show that the effective tangential stresses and, hence, the axial stresses around a wellbore are greatly affected by the formation anisotropic mechanical parameters. In addition, the presence of clay fixed charges and the use of a drilling mud with activity higher than the pore fluid native activity result in a region of tensile effective radial stress and less compressive tangential stress near the borehole wall which may lead to wellbore spalling and in extreme case will result in stuck pipe and non-productive time. Since wellbore stability analyses are usually performed based on effective stresses, ignoring either the porochemoelectroelastic behavior or the anisotropic characteristic of the shale formation will mislead the predictions of potential wellbore instability problems.

The newly-derived solutions are useful not only to analyze and simulate experimental testing results but also to predict possible problems arising from the electrochemical interactions between the shale and the outer environment fluid. In addition, geomechanics modelers can utilize the solutions as benchmarks to validate their numerical algorithms for hydraulic fracturing and reservoir simulations.

References

Abousleiman, Y.N. et al., 1996. Mandel's problem revisited. *Geotechnique*, **42**(2), 187-195.

Abousleiman, Y.N. et al., 1996. Poroviscoelastic analysis of borehole and cylinder problem. *Acta Mechanica*, **199**(1-4), 199-219.

Abousleiman, Y.N. and Cui, L., 1998. Poroelastic solution in transversely isotropic media for wellbore and cylinder. *Int. J. Solids Struct.*, **35**(34-35), 4905-4929.

Abousleiman, Y.N., et al., 2007. Geomechanics field and lab characterization of Woodford shale: The next gas play. Paper SPE 110120 in proceedings of the 2007 SPE Annual Technical Conference and Exhibition, Anaheim, California, Nov. 11-14.

Abousleiman, Y.N., Hoang, S.K., and Tran, M.H., 2010. Mechanical Characterization of Small Shale Samples Subjected to Fluid Exposure Using the Inclined Direct Shear Testing Device. *Int. J. of Rock Mech. Min. Sci.*, **47**(3), 335-367.

Amstrong, C.G., Lai, W.M., and Mow, V.C., 1984. An analysis of the unconfined compression of articular cartilage. *J. Biomech. Eng.*, **106**(2), 165-173.

Biot, M.A., 1941. General theory of three dimensional consolidation. *J. Appl. Phys.*, **12**(2), 155–164.

Black, H.N., Hower, W.E., 1965. Advantageous use of potassium chloride water for fracturing water sensitive formation. Paper 851-39-F in proceedings of the 1965 Mid-Continent District Meeting, API Div. of Production, Wichita, Mar. 31-Apr. 2.

Boresi, A.P. and Chong, K., 1987. *Elasticity in Engineering Mechanics*. Elsevier, New York.

Bunger, A.P., 2010. The Mandel-Cryer effect in chemoporoelasticity. *Int. J. Num. An. Meth. Geomech.*, **34**(14), 1479-1511.

Carter, J.P. and Booker, J.R., 1982, "Elastic consolidation around a deep circular tunnel" *Int. J. Solids Structures*, **18**(12), 1059-1074.

Chen, G., Ewy, R.T., and Yu, M., 2010. Analytic solutions with ionic flow for a pressure transmission test on shale. *J. Pet. Sci. Eng.*, **72**(2010), 158-165.

Chenevert, M. and Pernot, V., 1998. Control of shale swelling pressures using inhibitive water–base muds. Paper SPE 49263 in proceedings of the 1998 SPE Annual Technical Conference and Exhibition, New Orleans, Louisiana, Sep. 27–30.

Cheng, A.H-D., 1997. Material coefficients of anisotropic poroelasticity. *Int. J. Rock Mech. Min. Sci.*, **34**(2), 183-193.

Chilingarian, G.V., 1981. Compaction diagenesis. In: *Sediment Diagenesis* (A. Parker and B. Sellwood eds.). D. Reidel, Dodretch, Boston and Lancaster.

Corapcioglu, Y.M., 1991. Formulation of electro-chemico-osmotic process in soils. *Transp. Porous Media*, **6**(4), 435-444.

Coussy, O., 2004. *Poromechanics*. J Wiley & Sons, Chichester.

Cryer, C.W., 1963. A comparison of the three-dimensional consolidation theories of Biot and Tezraghi. *Quart. J. Mech. Appl. Math.*, **16**(4), 401-412.

Cui, L., et al., 1996. Finite element analyses of anisotropic poroelasticity: A generalized Mandel's problem and an inclined borehole problem. *Int. J. Numer. Anal. Meth. Geomech.*, **20**(6), 381-401.

Cui, L., Cheng, AH.-D., and Abousleiman, Y.N., 1997. Poroelastic solution of an inclined borehole. *J. App. Mech.*, **64**(1), 32-38.

Ekbote, S.M., 2002. *Anisotropic Poromechanics of the Wellbore Coupled with Thermal and Chemical Gradients*. Ph.D. Dissertation, University of Oklahoma.

Ekbote, S.M. and Abousleiman, Y.N., 2005. Porochemothermoelastic solution for an inclined borehole in a transversely isotropic formation. *J. Eng. Mech.*, **131**(5), 522−533.

Ekbote, S.M. and Abousleiman, Y.N., 2006. Porochemoelastic solution for an inclined borehole in a transversely isotropic formation. *J. Eng. Mech.*, **132**(7), 754−763.

Ewy, R.T. and Stankovich, R.J., 2010. Shale swelling, osmosis, and acoustic changes measured under simulated downhole conditions. *SPE Drilling & Completion*, **25**(2), 177-186.

Fakcharoenphol, P., et al., 2012. Fully-implicit flow and geomechanics model: Application for enhanced geothermal reservoir simulations. In proceedings of the 37th Workshop on Geothermal Reservoir Engineering, Stanford, Jan. 30-Feb. 1.

Farlow, 1993. *Partial Differential Equations for Scientists and Engineers*. Dover Publications Inc., New York.

Geerstma, J., 1973. Land subsidence above oil and gas reservoir. *J. Petro. Technol.*, **25**(6), 734-744.

Gu, W., et al., 1999. Transport of multi-electrolytes in charged hydrated biological soft tissues. *Transport Porous Med.*, **34**(1-2), 143–157.

Hemphill, T.A. et al., 2008. Direct strength measurements of shale interaction with drilling fluids. Paper SPE 117851 in proceedings of the 2008 Abu Dhabi International Petroleum Exhibition and Conference, Abu Dhabi, UAE, Nov. 3–6.

Hemphill, T.A. et al., 2010. Changing the safe drilling window with invert emulsion drilling fluids: Advanced wellbore stability modeling using experimental results. Paper SPE 132207 in proceedings of the 2010 CPS/SPE International Oil & Gas Conference and Exhibition, Beijing, China, Jun. 8–10.

Hoang, S.K. and Abousleiman, Y.N., 2009. Poroviscoelastic two-dimensional anisotropic solution with application to articular cartilage testing. *J. Eng. Mech.*, **135**(5), 367-373.

Huyghe, J.M. and Jassen, J.D., 1999. Thermo-chemo-electro-mechanical formulation of saturated charged porous solids. *Transport Porous Med.*, **34**(1-3), 129-141.

Johnston, J. E. and Christensen, N. I. 1995. Seismic Anisotropy of Shales. *J. Geophys. Res.*, **100**(B4), 5991-6003.

Jones, T.G.J., Hughes, T.L., and Tomkins, P., 1989. The ion content and mineralogy of a North Sea Cretaceous shale formation. *Clay Minerals*, **24**(2), 393-410.

Katchalsky, A. and Curran, P.F., 1967. *Nonequilibrium Thermodynamics in Biophysics*. Harvard University Press, Massachusetts.

Lekhnitskii, S.G., 1981. *Theory of Elasticity of an Anisotropic Elastic Body*. Transl. rev. 1977 Russian Ed., Mir Publishers, Moscow.

Lu, X.L., Mow, V.C., and Guo, X.E., 2009. Proteoglycans and Mechanical Behavior of Condylar Cartilage. *Journal of Dental Research*, **88**(3), 244-248.

Mandel, J., 1953. Consolidation des sols (etude mathematique). *Géotechnique*, **3**(7), 287-299.

Malusis, M.A. and Shackelford, C.D., 2002. Theory for reactive solute transport through clay membrane barriers. *J. Cont. Hydro.*, **59**(3-4), 291-316.

Neuzil, C.E., 2000. Osmotic generation of anomalous fluid pressures in geological environments. *Nature*, **403**(6766), 182-184.

Nguyen, V.X., Abousleiman, Y.N., and Hoang, S.K., 2009. Analyses of wellbore instability in drilling through chemically active fractured rock formations. *SPEJ*, **14**(2), 283-301.

Nguyen, V.X. and Abousleiman, Y.N., 2010. Incorporating electrokinetic effects in the porochemoelastic inclined wellbore formulation and solution. *An. Acad. Bras. Cienc.*, **82**(1), 1-28.

Nguyen, V.X. and Abousleiman, Y.N., 2010. Poromechanics solutions to plane strain and axisymmetric Mandel-type problems in dual-porosity and dual-permeability medium. *J. Appl. Mech.*, **77**(1), 011002.1-17.

Nguyen, V.X, 2010. *Dual-porosity and Dual-permeability Poromechanics Solutions for Problems in Laboratory and Field Applications*. Ph.D. Dissertation, University of Oklahoma.

Olsen, H.W., 1969. Simultaneous fluxes of liquid and charge in saturated kaolinite. *Soil Sci. Soc. Am. Proceedings*, **33**(3), 338-344.

Onsager, L., 1931. Reciprocal relations in irreversible processes I. *Phys. Rev.*, **37**(4), 405-426.

Overbeek, J.T., 1956. The Donnan equilibrium. *Progress in Biophysics*, **6**, 57-84.

Rosanne, M., Pasxukuta, M., and Adler, P.M., 2005. Electrokinetic phenomena in saturated compact clays. *J. Colloid Interface Sci.*, **297**(1), 353-364.

Sachs, J.R. and Grodzinsky, A.J., 1987. An electromechanically coupled poroelastic medium driven by an applied electrical current: Surface detection of bulk material parameters. *Phys. Chem. Hydrodynamics*, **11**, 585-614.

Sarout, J., 2003. *Experimental Identification of Chemoporoelastic Parameters for Reactive Shales*. Master Thesis, University of Minnesota.

Sarout, J. and Detournay, E., 2011. Chemoporoelastic analysis and experimental validation of the pore pressure transmission test for reactive shales. *Int. J. of Rock Mech. Min. Sci.*, **48**(5), 759-772.

Schmidt, G.W., 1973. Interstitial water composition and geochemistry of deep Gulf Coast shales and sandstones. *Am. Assoc. Pet. Geol. Bull.*, **57**(2), 321-337.

Shackelford, C.D. and Daniel, D.E., 1991. Diffusion in saturated soil. I: Background. *J. Geotech. Eng.*, **117**(3), 467-484.

Sherwood, J.D., 1993. Biot poroelasticity of a chemically active shale. *Proc. Royal Soc. Lond. A*, **440**(1909), 365‑377.

Sherwood, J.D. and Bailey, L., 1994. Swelling shale around a cylindrical wellbore. *Proc. Royal Soc. Lond. A*, **444**(1920), 161-184.

Sierra, R.P. et al., 2010. Woodford shale mechanical properties and the impacts of lithofacies. Paper ARMA 10-461 in proceedings of the 44th US Rock Mechanics Symposium and 5th U.S.-Canada Rock Mechanics Symposium, Salt Lake City, UT Jun. 27–30.

Stehfest, H., 1970. Numerical inversion of Laplace transform. *Commun. A.C.M.*, **13**(1), 47-49.

Tan, C.P., Richard, B.G., and Rahman, S.S., 1996. Managing physico-chemical wellbore instability in shales with the chemical potential mechanism. Paper SPE 36971 in proceedings of the 1996 Asia Pacific Oil and Gas Conference and Exhibition, Adelaide, Australia, Oct. 28-31.

Terzaghi, K., 1943. *Theoretical Soil Mechanics*. Wiley, New York.

Thomsen, L., 1986. Weak elastic anisotropy. *Geophysics*, **51**(10), 1954-1966.

Tran, M.H. and Abousleiman, Y.N., 2013. Anisotropic porochemoelectroelastic solution for an inclined wellbore drilled in shale. *J. Appl. Mech.*, **80**(2), 020912.1-14.

Tran, M.H. and Abousleiman, Y.N., 2013. Anisotropic porochemoelectroelastic solution for applications in reservoir modeling and laboratory characterization. *Mech. Res. Comm.*, **47**(January), 89-96.

Van Meerveld, J. et al., 2003. Analytical solution of compression, free swelling and electrical loading of saturated charged porous media. *Transport Porous Med.*, **50**(1-2), 111–126.

Van Oort, E., 1994. A novel technique for the investigation of drilling fluid induced borehole instability in shales. Paper SPE/ISRM 28064 in proceedings of the 1994 SPE/ISRM Rock Mechanics in Petroleum Engineering Conference, Delft, Aug. 29-31.

Wang, H.F., 2000. *Theory of Linear Poroelasticity with Applications to Geomechanics and Hydrology*. Princeton University Press, Princeton.

Yeung, A.T. and Mitchell, J.K., 1993. Coupled fluid, electrical and chemical flows in soil. *Geotechnique*, **43**(1), 121-134.

Yew, C.H. et al., 1990. Wellbore stress distribution produced by moisture adsorption. *SPE Drilling Eng.*, **5**(4), 311-316.

Yin, S., et al., 2006. 3D Coupled displacement discontinuity and finite element analysis of reservoir behavior during production in semi-infinite domain. *Transport Porous Med.*, **65**(3), 425–441.

Appendix A: Relationships between Elastic Stiffness Coefficients and Elastic Moduli for Anisotropic Medium

Transversely Isotropic Material

The elastic stiffness coefficients, C_{ij}, can be expressed in terms of the familiar engineering moduli as (*Boresi & Chong*, 1987)

$$C_{11} = \frac{E_1(E_3 - E_1 v_3^2)}{(1+v_1)(E_3 - E_3 v_1 - 2E_1 v_3^2)} \tag{A-1}$$

$$C_{12} = \frac{E_1(E_3 v_1 + E_1 v_3^2)}{(1+v_1)(E_3 - E_3 v_1 - 2E_1 v_3^2)} \tag{A-2}$$

$$C_{13} = \frac{E_1 E_3 v_3}{E_3 - E_3 v_1 - 2E_1 v_3^2} \tag{A-3}$$

$$C_{33} = \frac{E_3^2(1-v_1)}{E_3 - E_3 v_1 - 2E_1 v_3^2} \tag{A-4}$$

$$C_{44} = G = \frac{C_{11} - C_{12}}{2} = \frac{E_1}{2(1+v_1)} \tag{A-5}$$

$$C_{55} = G_3 \tag{A-6}$$

where E_1 and E_3 are the Young's modulus in the direction parallel to and perpendicular to the isotropic plane (i.e. the apparent laminations of the rock) respectively. v_1 is the Poisson's ratio which characterizes the transverse expansion in the isotropic plane due to a load in the same plane, and v_3 is the Poisson's ratio which gives the transverse expansion in the isotropic plane due to a load normal to the plane.

Following Abousleiman et al. (1996), the transversely isotropic Biot's pore pressure coefficients α_1 and α_3 can be expressed in terms of C_{ij} and the bulk modulus of the solid grains, K_s, as

$$\alpha_1 = 1 - \frac{C_{11} + C_{12} + C_{13}}{3K_s} \tag{A-7}$$

$$\alpha_3 = 1 - \frac{2C_{13} + C_{33}}{3K_s} \tag{A-8}$$

The Biot's modulus, *M*, is given as (*Cui et al.*, 1996)

$$M = \frac{K_s^2}{K_s\left[1 + \phi(K_s / K_f - 1)\right] - M_{avg}} \tag{A-9a}$$

$$M_{avg} = \frac{C_{11} + 2C_{33} + 2C_{12} + 4C_{13}}{9} \tag{A-9b}$$

Orthotropic Material

The elastic stiffness coefficients, C_{ij}, can be expressed in terms of the familiar engineering moduli as (*Lekhnitskii,* 1981)

$$C_{11} = \frac{E_1(\nu_{23}\nu_{12} - 1)}{v_d} \tag{A-10}$$

$$C_{12} = -\frac{E_2(\nu_{13}\nu_{32} + \nu_{12})}{v_d} \tag{A-11}$$

$$C_{13} = -\frac{E_2(\nu_{13}\nu_{32} + \nu_{13})}{v_d} \tag{A-12}$$

$$C_{22} = \frac{E_2(\nu_{13}\nu_{31} - 1)}{v_d} \tag{A-13}$$

$$C_{23} = -\frac{E_1(\nu_{13}\nu_{21} + \nu_{23})}{v_d} \tag{A-14}$$

$$C_{33} = \frac{E_3(\nu_{12}\nu_{21} - 1)}{v_d} \tag{A-15}$$

$$C_{44} = G_{12} \tag{A-16}$$

$$C_{55} = G_{13} \tag{A-17}$$

$$C_{66} = G_{23} \tag{A-18}$$

where E_1, E_2, E_3 are the Young's modulus in the 1, 2, and 3 direction respectively. G_{12}, G_{13}, and G_{23} are the shear moduli for planes that are parallel to the coordinate planes 1-2, 2-3, and 1-3. Finally, ν_{ij} (i, j = 1, 2, 3) are the Poisson's ratio characterized by the expansion in the j-direction due to applied stress in the i-direction.

The anisotropic Biot's pore pressure coefficients, α_1 and α_3, and Biot's modulus, M, can be expressed in terms of C_{ij} and the bulk modulus of the solid grains, K_s, as (*Cui et al*., 1996; *Cheng*, 1997)

$$\alpha_1 = 1 - \frac{C_{11} + C_{12} + C_{13}}{3K_s} \tag{A-19}$$

$$\alpha_2 = 1 - \frac{C_{12} + C_{22} + C_{23}}{3K_s} \tag{A-20}$$

$$\alpha_{33} = 1 - \frac{C_{13} + C_{23} + C_{33}}{3K_s} \tag{A-21}$$

$$M = \frac{K_s^2}{K_s\left[1 + \phi(K_s / K_f - 1)\right] - M_{avg}} \tag{A-22}$$

with

$$M_{avg} = \frac{C_{11} + C_{22} + C_{33} + 2C_{12} + 2C_{13} + 2C_{23}}{9} \tag{A-23}$$

Appendix B: Wellbore Plane Strain Solutions

Solution for Part 1: Axis-Symmetric Loading

The Laplace transformed boundary conditions at $r = R_w$ are as follows

$$\widetilde{\sigma}_{rr} = -\frac{M_o}{s} + \widetilde{p}_{mud} \tag{B-1a}$$

$$\widetilde{p} = \Delta\widetilde{p} \tag{B-1b}$$

$$\widetilde{p}_a = \Delta\widetilde{p}_a \tag{B-1c}$$

$$\widetilde{p}_c = \Delta\widetilde{p}_c \tag{B-1d}$$

The solution in Laplace transform domain is as follows

$$\widetilde{p}^{(1)} = \sum_{i=1}^{3} m_{1i}\Delta_i\Phi(\xi_i) \tag{B-2}$$

$$\widetilde{p}_a^{(1)} = \sum_{i=1}^{3} m_{2i}\Delta_i\Phi(\xi_i) \tag{B-3}$$

$$\widetilde{p}_c^{(1)} = \sum_{i=1}^{3} m_{3i}\Delta_i\Phi(\xi_i) \tag{B-4}$$

$$\widetilde{\sigma}_{rr} = \left(-\frac{M_o}{s} + \widetilde{p}_{mud}\right)\frac{R_w^2}{r^2} - 2\frac{\alpha_1 G}{C_{11}}\sum_{i=1}^{3} m_{1i}\Delta_i\Xi(\xi_i) \tag{B-5}$$

$$\widetilde{\sigma}_{\theta\theta} = \left(\frac{M_o}{s} - \widetilde{p}_{mud}\right)\frac{R_w^2}{r^2} + 2\frac{\alpha_1 G}{C_{11}}\sum_{i=1}^{3} m_{1i}\Delta_i\left[\Xi(\xi_i) + \Phi(\xi_i)\right] \tag{B-6}$$

with

$$\Phi(\xi_i) = \frac{K_o(\xi_i r)}{K_o(\xi_i R_w)} \tag{B-7}$$

$$\Xi(\xi_i) = \frac{K_1(\xi_i r)}{\xi_i r K_o(\xi_i R_w)} - \frac{R_w K_1(\xi_i R_w)}{\xi_i r^2 K_o(\xi_i R_w)} \tag{B-8}$$

$$[\Delta]=\frac{1}{m}\begin{bmatrix} m_{22}m_{33}-m_{23}m_{32} & m_{13}m_{32}-m_{12}m_{33} & m_{12}m_{23}-m_{13}m_{22} \\ m_{23}m_{31}-m_{21}m_{33} & m_{11}m_{33}-m_{13}m_{31} & m_{13}m_{21}-m_{11}m_{23} \\ m_{21}m_{32}-m_{22}m_{31} & m_{12}m_{31}-m_{11}m_{32} & m_{11}m_{22}-m_{12}m_{21} \end{bmatrix}\begin{bmatrix} \Delta\widetilde{p} \\ \Delta\widetilde{p}_a \\ \Delta\widetilde{p}_c \end{bmatrix} \tag{B-9}$$

and

$$m = m_{11}(m_{22}m_{33}-m_{23}m_{32})-m_{12}(m_{21}m_{33}-m_{23}m_{31})+m_{13}(m_{21}m_{32}-m_{22}m_{31}) \tag{B-10}$$

Solution for Part 2: Deviatoric Loading

The Laplace transformed boundary conditions at $r = R_w$ are as follows

$$\widetilde{\sigma}_{rr} = -\frac{S_o}{s}\cos[2(\theta-\theta_o)] \tag{B-11b}$$

$$\widetilde{\sigma}_{r\theta} = \frac{S_o}{s}\cos[2(\theta-\theta_o)] \tag{B-11b}$$

$$\widetilde{p} = \widetilde{p}_a = \widetilde{p}_c = 0 \tag{B-11c}$$

The solution in Laplace transform domain is as follows

$$\widetilde{p} = \left[f_1 \frac{C_o}{r^2} + \sum_{i=1}^{3} m_{1i} C_i K_2(\xi_i r) \right] \cos[2(\theta-\theta_o)] \tag{B-12}$$

$$\widetilde{p}_a = \left[f_2 \frac{C_o}{r^2} + \sum_{i=1}^{3} m_{2i} C_i K_2(\xi_i r) \right] \cos[2(\theta-\theta_o)] \tag{B-13}$$

$$\widetilde{p}_c = \left[f_3 \frac{C_o}{r^2} + \sum_{i=1}^{3} m_{3i} C_i K_2(\xi_i r) \right] \cos[2(\theta-\theta_o)] \tag{B-14}$$

$$\widetilde{\sigma}_{rr} = 2G\left\{ \begin{array}{l} \left(\frac{C_{11}}{G} + \frac{\alpha_1 f_1}{C_{11}} - 1 \right) \frac{C_o}{r^2} - \frac{3C_4}{r^4} \\ \qquad -\frac{\alpha_1}{C_{11}} \left[6\sum_{i=1}^{3} \frac{m_{1i} C_i K_2(\xi_i r)}{\xi_i^2 r^2} + \sum_{i=1}^{3} \frac{m_{1i} C_i K_1(\xi_i r)}{\xi_i r} \right] \end{array} \right\} \cos[2(\theta-\theta_o)] \tag{B-15}$$

$$\widetilde{\sigma}_{\theta\theta} = 2G\left\{ \frac{3C_4}{r^4} + \frac{\alpha_1}{C_{11}} \left[\begin{array}{l} 6\sum_{i=1}^{3} \frac{m_{1i} C_i K_2(\xi_i r)}{\xi_i^2 r^2} \\ \qquad + \sum_{i=1}^{3} \frac{m_{1i} C_i K_1(\xi_i r)}{\xi_i r} + \sum_{i=1}^{3} m_{1i} C_i K_2(\xi_i r) \end{array} \right] \right\} \cos[2(\theta-\theta_o)] \tag{B-16}$$

$$\widetilde{\sigma}_{r\theta} = 2G\left\{\begin{array}{l}\left(\dfrac{C_{11}}{G}+\dfrac{\alpha_1 f_1}{C_{11}}-1\right)\dfrac{C_o}{2r^2}-\dfrac{3C_4}{r^4} \\ \qquad -\dfrac{2\alpha_1}{C_{11}}\left[3\displaystyle\sum_{i=1}^{3}\frac{m_{1i}C_i K_2(\xi_i r)}{\xi_i^2 r^2}+\sum_{i=1}^{3}\frac{m_{1i}C_i K_1(\xi_i r)}{\xi_i r}\right]\end{array}\right\}\cos\left[2\left(\theta-\theta_o\right)\right] \tag{B-17}$$

with

$$\begin{bmatrix}C_1\\C_2\\C_3\end{bmatrix} = \frac{2S_o}{sG\left(\dfrac{C_{11}}{G}+\dfrac{\alpha_1 f_1}{C_{11}}-1\right)}\left[K\right]^{-1}\begin{bmatrix}f_1\\f_2\\f_3\end{bmatrix} \tag{B-18}$$

$$C_o = -\frac{2R_w^2 S_o}{sG\left(\dfrac{C_{11}}{G}+\dfrac{\alpha_1 f_1}{C_{11}}-1\right)}-\frac{2R_w^2\alpha_1}{\dfrac{C_{11}^2}{G}+\alpha_1 f_1 - C_{11}}\sum_{i=1}^{3}\frac{m_{1i}C_i K_2(\xi_i R_w)}{\xi_i R_w} \tag{B-19}$$

$$C_4 = -\frac{2R_w^4 S_o}{2sG}-\frac{R_w^4\alpha_1}{C_{11}}\sum_{i=1}^{3}\left[\frac{2m_{1i}C_i K_2(\xi_i R_w)}{\xi_i^2 R_w^2}+\frac{m_{1i}C_i K_1(\xi_i R_w)}{\xi_i R_w}\right] \tag{B-20}$$

and

$$K_{ij} = m_{ij}K_2(\xi_j R_w)-\frac{2\alpha_1}{\dfrac{C_{11}^2}{G}+\alpha_1 f_1 - C_{11}}\frac{f_1 K_1(\xi_j R_w)}{\xi_j R_w} \tag{B-21}$$